IMPROVEMENT OF AFTERSHOCK MODELS BASED ON COULOMB STRESS CHANGES AND RATE-AND-STATE DEPENDENT FRICTION

BY

CAMILLA CATTANIA

Dissertation

in fulfilment of the requirements for the degree of
doctor rerum naturalium (Dr. rer. nat.)
in the subject of Geophysics

submitted to
Faculty of Mathematics and Natural Sciences
University of Potsdam

Published online at the
Institutional Repository of the University of Potsdam:
URN urn:nbn:de:kobv:517-opus4-87097
http://nbn-resolving.de/urn:nbn:de:kobv:517-opus4-87097

ABSTRACT

Earthquake clustering has proven the most useful tool to forecast changes in seismicity rates in the short and medium term (hours to months), and efforts are currently being made to extend the scope of such models to operational earthquake forecasting. The overarching goal of the research presented in this thesis is to improve physics-based earthquake forecasts, with a focus on aftershock sequences. Physical models of triggered seismicity are based on the redistribution of stresses in the crust, coupled with the rate-and-state constitutive law proposed by Dieterich to calculate changes in seismicity rate. This type of models are known as Coulomb-rate-and-state (CRS) models. In spite of the success of the Coulomb hypothesis, CRS models typically performed poorly in comparison to statistical ones, and they have been underepresented in the operational forecasting context. In this thesis, I address some of these issues, and in particular these questions: (1) How can we realistically model the uncertainties and heterogeneity of the mainshock stress field? (2) What is the effect of time dependent stresses in the postseismic phase on seismicity? I focus on two case studies from different tectonic settings: the M_w 9.0 Tohoku megathrust and the M_w 6.0 Parkfield strike slip earthquake.

I study aleatoric uncertainties using a Monte Carlo method. I find that the existence of multiple receiver faults is the most important source of intrinsic stress heterogeneity, and CRS models perform better when this variability is taken into account. Epistemic uncertainties inherited from the slip models also have a significant impact on the forecast, and I find that an ensemble model based on several slip distributions outperforms most individual models.

I address the role of postseismic stresses due to aseismic slip on the mainshock fault (afterslip) and to the redistribution of stresses by previous aftershocks (secondary triggering). I find that modeling secondary triggering improves model performance. The effect of afterslip is less clear, and difficult to assess for near-fault aftershocks due to the large uncertainties of the afterslip models. Off-fault events, on the other hand, are less sensitive to the details of the slip distribution: I find that following the Tohoku earthquake, afterslip promotes seismicity in the Fukushima region.

To evaluate the performance of the improved CRS models in a pseudo-operational context, I submitted them for independent testing to a collaborative experiment carried out by CSEP for the 2010-2012 Canterbury sequence. Preliminary results indicate that physical models generally perform well compared to statistical ones, suggesting that CRS models may have a role to play in the future of operational forecasting. To facilitate efforts in this direction, and to enable future studies of earthquake triggering by time dependent processes, I have made the code open source. In the final part of this thesis I summarize the capabilities of the program and outline technical aspects regarding performance and parallelization strategies.

ZUSAMMENFASSUNG

Die örtliche und zeitlich Häufung von Erdbeben ist geeignet, um Änderungen in Seismizitätsraten auf kurzen bis mittleren Zeitskalen (Stunden bis Monate) zu prognostizieren. Kürzlich wurden vermehrt Anstrengungen unternommen, den Umfang solcher Modelle auf Operationelle Erdbebenvorhersage auszudehnen, welche die Veröffentlichung von Erdbebenwahrscheinlichkeiten beinhaltet mit dem Ziel, die Bevölkerung besser auf mögliche Erdbeben vorzubereiten. Das vorrangige Ziel dieser Dissertation ist die Verbesserung von kurz- und mittelfristiger Erdbebenprognose basierend auf physikalischen Modellen. Ich konzentriere mich hier auf Nachbebensequenzen. Physikalische Modelle, die getriggerte Seimizität erklären, basieren auf der Umverteilung von Spannungen in der Erdkruste. Berechnung der Coulomb Spannung können kombiniert werden mit dem konstituivem Gesetz von Dieterich, welches die Berechnung von Änderungen in der Seismizitätsrate ermöglicht. Diese Modelle sind als Coulomb-Rate-and-State (CRS) Modelle bekannt. Trotz der erfolgreichen Überprüfung der Coulomb-Hypothese, schneiden CRS-Modelle im Vergleich mit statistischen Modellen schlecht ab, und wurden deshalb bisher kaum im Kontext operationeller Erdbenbenvorhersage genutzt. In dieser Arbeit, gehe ich auf einige der auftretenden Probleme ein. Im Besonderen wende ich mich den folgenden Fragen zu: (1) Wie können wir die Unsicherheiten und die Heterogenität des Spannungsfeldes infolge des Hauptbebens realistisch modellieren? (2) Welche Auswirkungen haben zeitlich variable Spannungsänderungen in der postseismischen Phase? Ich konzentriere mich hierbei auf zwei Beispiele in unterschiedlichen tektonischen Regionen: die Aufschiebung des M_w9.0 Tohoku Erdbeben und die Blattverschiebung des M_w6.0 Parkfield Erdbeben.
Ich untersuche aleotorische Unsicherheiten der Coulomb-Spannung durch Variabilität in der Orientierung der betroffenen Bruchflächen und durch Spannungsgradienten innerhalb von Modellzellen. Ich zeige, dass die Existenz der unterschiedlichen Bruchflächen die bedeutenste Quelle für intrinsiche Spannungheterogenität ist und das CRS-Modelle deutlich besser abschneiden, wenn diese Variabilität berücksichtigt wird. Die epistemischen Unsicherheiten aufgrund von unterschiedlichen Ergebnissen von Inversionen von Daten für die Verschiebung entlang der Bruchfläche haben ebenso erhebliche Auswirkungen auf die Vorhersage.
Ich gehe dann auf die Rolle von postseismischen Spannung ein, insbesondere auf zwei Prozesse: aseismische Verschiebung entlang der Störungsfläche des Hauptbebens (Afterslip) und die Veränderung von Spannungen durch vorhergehende Nachbeben (sekundäres Triggern). Ich demonstriere, dass das Modellieren von sekundärem Triggern die Modellvorhersage in beiden Fallbeispielen verbessert. Die Einbeziehung von Afterslip verbessert die Qualität der Vorhersage nur für die

Nachbebensequenz des Parkfield Erdbebens. Dagegen kann ich nachweisen, dass Afterslip infolge des Tohoku Bebens eine höhere Seismizität auf Abschiebungsflächen im Hangenden begünstigt.
Die dargestellten Verbesserungen des CRS-Modells sind sehr vielversprechend im Kontext operationeller Erdbebenvorhersage, verlangen aber nach weiterer Überprüfung. Ich stelle die vorläufigen Ergebnisse eines gemeinschaftlichen Tests für die Erdbebenfolge von Canterbury 2010-2012 vor, welcher von CSEP durchgeführt wurde. Die physikalischen Modelle schneiden hier im Vergleich mit statistischen Modellen gut ab. Daher scheint eine Anwendung von CSR-Modellen, die Unsicherheiten und sekundäres Triggering berücksichtigen, in zukünftigen operationellen Erdbebenvorhersagen empfehlenswert.
Um die Bemühungen in dieser Richtung zu unterstützen und weitere Studien zum Triggern von Erdbeben durch zeitabhängige Prozesse zu ermöglichen, habe ich meinen Open Source Code öffentlich zugänglich gemacht. Im letzten Teil dieser Arbeit fasse ich die Leistungsfähigkeit des Programms zusammen und skizziere die technischen Aspekte bezüglich der Effiziens und der Parallelisierung des Programmes.

PUBLICATIONS

I have published the following articles during the course of this PhD:

- Hainzl, S., Y. Ben-Zion, **C. Cattania**, and J. Wassermann, Testing atmospheric and tidal earthquake triggering at Mt. Hochstaufen, Germany, *Journal Geophys. Res.*, *118*(\), 5442–5452, doi: 10.1002/jgrb.50387, 2013

  My contribution: I developed part of the methods (use of multiple receiver faults for Coulomb stress calculations, described in Chapter 3); I provided feedback on the manuscript, and in particular on the reliability of the rate-and-state parameters. S.H. wrote the manuscript and prepared the figures.

- **Cattania, C.**, S. Hainzl, L. Wang, F. Roth, and B. Enescu, Propagation of Coulomb stress uncertainties in physics-based aftershock models, *J. Geophys Res.*, *119*, 7846–7864, doi: 10.1002/2014JB011183, 2014

  My contribution: I developed the methods, run the models, wrote the article and made the figures; the contribution of the other authors consisted of supervising the project (S.H. and F.R.), providing seismicity data and slip models (B.E. and L.W.) and providing feedback on the manuscript (all co-authors).

- **Cattania, C.**, S. Hainzl, L. Wang, B. Enescu, and F. Roth, Aftershock triggering by postseismic stresses: a study based on Coulomb-Rate-and-State models, *J. Geophys Res.*, *in press*, doi: 10.1002/2014JB011500, 2015

  My contribution: same as for the previous article.

The following article is in preparation:

- **Cattania, C.**, and F. Khalid, A parallel code to calculate seismicity evolution induced by time dependent, heterogeneous Coulomb stress changes, *in preparation for submission to Computers and Geosciences*

  My contribution: I wrote the serial code and implemented the OpenMP parallelization, and I wrote ~80% of the article; F.K. implemented the MPI parallelization and wrote ~20% of the article; both authors produced the figures.

CONTENTS

LIST OF FIGURES

LIST OF TABLES

ACRONYMS AND SYMBOLS

General acronyms

CRS	Coulomb Rate-State
RS	Rate-State
ETAS	Epidemic Type Aftershock Sequence
CSEP	Collaboratory for the Study of Earthquake Predictability
ANSS	Advanced National Seismic System
JMA	Japan Meteorological Agency
IPOC	Integrated Plate Boundary Observatory Chile

Parameters in CRS models

ΔCFS	Coulomb stress change (Section 2.1, Eq. 2.2)
τ	shear stress (Section 2.1, Eq. 2.2)
σ_{tot}	effective normal stress (Section 2.1, Eq. 2.2)
μ, μ'	coefficient of friction, effective coefficient of friction (Section 2.1, Eq. 2.2)
B	Skempton coefficient (Section 2.1)
R	seismicity rate (Section 2.2, Eq. 2.4; Section 6.2.2)
r_0	background seismicity rate (Section 2.2, Eq. 2.4; Section 2.3.1)
$\dot{\tau}_r$	tectonic shear stressing rate (Section 2.2, Eq. 2.4)
γ	rate-state evolution parameter (Section 2.2, Eq. 2.4; Section 6.2.2)
$A\sigma$	fault constitutive parameter (Section 2.2, Eq. 2.3, 2.4)
t_a	aftershock duration time (Section 2.2, Eq. 2.6)
OOP	Optimally Oriented Plane (Section 3.2.1)

Statistical quantities

LL log-likelihood (Section 2.3, Eq. 2.7)

I information gain (Section 2.4, Eq. 2.8)

I_{ev} information gain per event (Section 2.4, Eq. 2.9)

Other parameters

p Omori p-value (Section 1.1, Eq. 1.1)

c Omori c-value (Section 1.1, Eq. 1.1)

M_0 seismic moment

M_w moment magnitude

M_c completeness magnitude

1

INTRODUCTION

The degree to which earthquakes are predictable has been a subject of debate for decades (for a discussion on the topic, see *Main* [1999]), and the prediction of destructive shocks has been defined "the holy grail of seismology" [*Hough*, 2009]. If earthquake prediction is understood as a deterministic statement on the location and time of the next earthquake, it may never be achieved: the occurrence of precursory phenomena to large earthquakes is at best sporadic, and a reliable method of prediction in the short term (days to hours) and small spatial scales has not been identified [*Jordan et al.*, 2011]. On contrary, our current understanding of plate tectonics and the earthquake cycle allows to define with a certain degree of confidence where destructive earthquakes will occur within a time scale of centuries or millennia; and more importantly, the well recognized clustering behaviour of earthquakes in the medium term (days to years) allows to produce time-dependent hazard estimates, and to issue probabilistic statements about earthquake occurrence.
The need for rigorous testing of such theories and the importance of effective communication to the public has been made extremely clear by the controversial accusation towards seven Italian seismologists for "approximate risk assessment" and "ineffective communication" during the L'Aquila seismic sequence in 2009. Following these events, increased attention has been placed by the seismological community towards the implementation of Operational Earthquake Forecasting, defined as

> *The continual updating of authoritative information about the future occurrence of potentially damaging earthquakes, and the officially sanctioned dissemination of this information to enhance earthquake preparedness in threatened communities.* [*Jordan et al.*, 2011]

The work presented in this thesis, supported by the EU-project REAKT, falls within these efforts. While the focus is on aftershock sequences, the physical concepts behind the models discussed here can

in principle be extended to other examples of earthquake sequences, including foreshocks as well as natural or human-induced swarms. The abundance of aftershocks, and the fact that their first order features in space and time are relatively well understood, makes them a particularly suitable target for studying the physical mechanisms driving seismicity, and for the development of forecasting models. Moreover, the goal of forecasting aftershocks is in itself a worthwhile effort in terms of its societal benefits: as clearly demonstrated by recent seismic sequences in Canterbury, New Zealand (2010-2012) and in Emilia Romagna, Italy (2012) aftershocks can in some cases create as much damage as the mainshock.

1.1 Main features of aftershock sequences

A well recognized feature of earthquakes is their tendency to cluster in space and time: examples are foreshock sequences, aftershock sequences, and swarms. Aftershocks are the most ubiquitous example of seismic sequences, following virtually every large earthquake in all tectonic settings.
The temporal decay of aftershocks follows a power law, first discovered by Omori following the 1981 Nobi earthquake and later modified by Utsu [*Utsu et al.*, 1995]:

$$N(t) = \frac{K}{(t+c)^p} \tag{1.1}$$

where N is the number of earthquakes per unit time, t is the time from the mainshock, and K, c and p are constants. The total number of aftershocks scales exponentially with mainshock magnitude [*Utsu and Seki*, 1955; *Utsu*, 1971] and linearly with the mainshock rupture area [*Yamanaka*, 1990]; most aftershocks occur on the mainshock fault and within few rupture lengths, but aftershocks have also been observed at distances of several fault lengths up to thousands of kilometres [*Felzer and Brodsky*, 2006; *Freed*, 2005].

1.2 Physical mechanism for earthquake triggering

Aftershocks and other triggered earthquakes are commonly understood as a process relaxing the stress concentration produced by the mainshock. While the observation of remote triggering is associated with the dynamic stress changes due to the passage of seismic waves, the stresses induced by static deformation is considered to be the dominant

mechanism at a distance of few fault lengths, although controversy exists [*Felzer and Brodsky*, 2006; *Richards-Dinger et al.*, 2010; *Hainzl et al.*, 2014].
Das and Scholz [1981] were the first to identify a spatial correlation between increases in shear stress off the mainshock fault and aftershock locations; but it is not until the early 90s that *Stein et al.* [1992] and *King et al.* [1994] introduced the concept of Coulomb stress changes (a linear combination of shear and normal stress changes) and demonstrated that positive Coulomb stress changes are responsible for earthquake triggering during a sequence of large events in the Eastern California Shear Zone. The most compelling example of Coulomb stress triggering presented in these studies is the M_w6.3 Big Bear earthquake, which occurred few hours after the 1992 M_w7.3 Landers earthquake (see Fig. 1.1). Since then, calculations of Coulomb stress changes has proved a useful tool to explain several feature of aftershock sequences [*Hainzl et al.*, 2010a, 2014], and they have been applied in several locations worldwide, including New Zealand [*Doser and Robinson*, 2002], Turkey [*Nalbant et al.*, 2002; *Stein et al.*, 1997], Italy [*Nostro et al.*, 2005]; as well as subduction zones, such as Japan [*Toda et al.*, 1998], Sumatra [*Mccloskey et al.*, 2005], the Aleutian and Chile [*Lin and Stein*, 2004].

The concept of static stress transfer can explain the spatial distribution of aftershocks, and the scaling between number of triggered events and mainshock size. However, a time dependent process must be involved in order to explain the temporal evolution of aftershocks. An instantaneous stress change can be reconciled with the observed time dependent (Omori-type) seismicity by considering a time dependent frictional response. Based on experimental results about the frictional properties of rocks [*Dieterich*, 1979], *Dieterich* [1994] introduced a constitutive law for the evolution of seismicity due to stress changes. Due to the finite nucleation time of a population of faults subject to a sudden stress change, aftershock triggering may be delayed; in fact, seismicity rates evolve following an inverse power law, in agreement with the observed Omori-Utsu decay.
An alternative interpretation is that the time dependence of seismicity is driven by time-dependent, aseismic stresses. Processes which may be responsible for inducing stress changes are fluid flow [*Cocco and Rice*, 2002], viscoelastic relaxation [*Freed and Lin*, 2001] and aseismic slip on the mainshock fault plane. Aseismic slip has been associated with seismicity in a variety of settings, including swarms [*McGuire et al.*, 2005], and foreshock sequences [*Kato et al.*, 2012]. In the postseismic phase, afterslip on the mainshock rupture plane is frequently observed, and has been suggested to be the main mechanism driving aftershock sequences [*Perfettini and Avouac*, 2007].

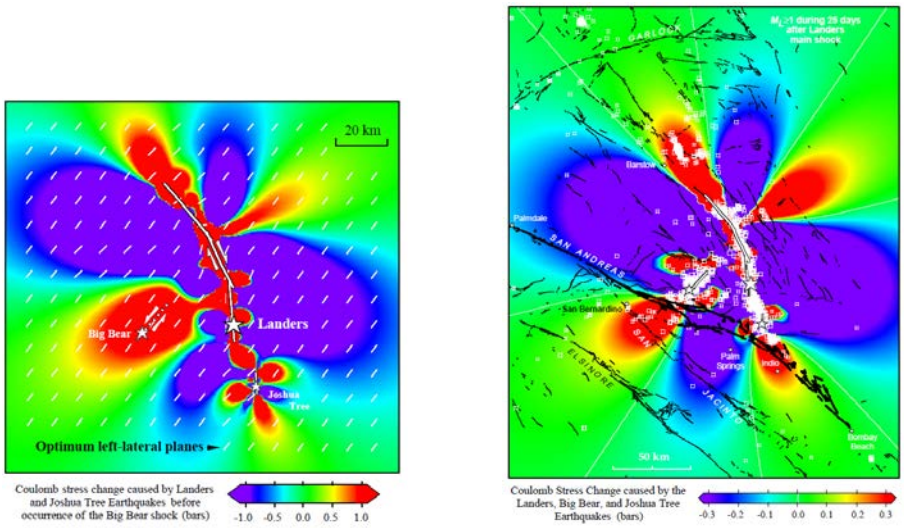

Figure 1.1: *Coulomb stress maps for the earthquake sequence including the Joshua Tree, Landers, and the Big Bear earthquakes, from King et al. [1994]. Left: stresses from the Joshua Tree and the Landers earthquakes. The Big Bear earthquake, which occurred approximately 3.5h after the Landers earthquake, is located on a lobe of positive Coulomb stress. Right: Stress changes from all 3 earthquakes, with 25 days of aftershocks from the Landers earthquake superimposed (white squares): a good spatial correlation between aftershocks and positive Coulomb stress changes is visible.*

Understanding the relative role of stress changes from static displacement, dynamic waves, and aseismic processes including slow slip and fluid migration is a central goal in current earthquake research: advances in this areas would not only increase our theoretical understanding of fault behaviour, but also guide the development of models aimed at earthquake forecasting and prediction.

1.3 Challenges to the Coulomb stress hypothesis

While a correlation between Coulomb stress changes and aftershock location has repeatedly been reported, several studies have questioned the validity of the Coulomb stress hypothesis and its predictive power; for example, *Hardebeck et al.* [1998] found that only 60% of the aftershocks of the Northridge earthquake fall in areas of positive Coulomb stress change. The Coulomb hypothesis predicts a reduction of seismicity in areas of negative Coulomb stress (stress shadows); and while this

behaviour has been reported in few cases [*Toda and Stein*, 2003; *Toda et al.*, 2012], high seismicity rates in regions of negative Coulomb stress change have more frequently been observed [*Mallman and Parsons*, 2008; *Marsan*, 2003].
An interplay between static coseismic stress changes and the other processes described above may explain the occurrence of aftershocks in stress shadows. Another explanation is the presence of heterogeneity in the stress field [*Helmstetter and Shaw*, 2006; *Marsan*, 2006]: unresolved, small scale slip on the mainshock fault plane generates a rough stress distribution in the near field, so that unresolved areas of high stress concentration may be present on the mainshock fault plane. Furthermore, the roughness of the faults which experience stress changes also causes an heterogeneous stress field, which is typically not considered in Coulomb stress studies assuming a relatively uniform orientation of faults.

1.4 Physical modelling and earthquake forecasting

The large majority of applications of Coulomb-based models are retrospective, with Coulomb stress changes sometimes calculated directly at the location of subsequent events. While these studies offer insight on whether observed events were favoured by Coulomb stress, they may suffer from "sharpshooter fallacy"[1]: the analysis is limited to the aftershocks which occurred, but do not take into consideration locations which experienced positive Coulomb stress changes without an increase in seismicity. The need for rigorous statistical verification of the Coulomb hypothesis has been raised by several authors [*Strader and Jackson*, 2014; *Toda and Enescu*, 2011]: the implementation of Coulomb-based models in the context of operational earthquake forecasting offers the possibility to perform statistical testing, and to compare the predictive value of the Coulomb to alternative models.
Models aimed at forecasting seismicity can be broadly divided into three categories:

- **Statistical models** based on the empirical relations discussed above (Omori-Utsu law and the scaling of productivity with mainshock magnitude) or on the location of previous earthquakes;
- **Physical models** which attempt to forecast seismicity based on our

1 "The Texas sharpshooter fallacy is an informal fallacy which is committed when differences in data are ignored, but similarities are stressed. The name comes from a joke about a Texan who fires some gunshots at the side of a barn, then paints a target centred on the biggest cluster of hits and claims to be a sharpshooter." [*Wikipedia*]

physical understanding of earthquake triggering (Coulomb stress, rate-and-state friction);

- **Hybrid models** which combine elements of statistical and physical models.

Time-dependent seismicity models are implemented for several regions in the world, and routinely tested in a fully prospective setting by the Collaboratory for the Study of Earthquake Predictability (CSEP). Physics-based models are currently severely under-represented in these studies. Retrospective studies have shown that the ability of physical models in predicting aftershocks is poor in comparison to statistical models [*Woessner et al.*, 2011]; this result may have discouraged the submission of Coulomb based models to CSEP testing centres for prospective testing. The poor performance of these models can be explained by the physical reasons outlined above: the presence of time-dependent stresses induced by secondary processes, and the small scale heterogeneity of the stress field. And while several studies have addressed these issues on a rather theoretical level, the implementation of physical models which take these aspects into account lags behind.

1.5 Goals of the thesis and roadmap

The goal of this work is to bring the current knowledge of Coulomb triggering and rate-and-state frictional response into the realm of Operational Earthquake Forecasting. While an improvement in model performance is a desirable outcome of this work, my approach has been guided first of all by an attempt to construct physically consistent and realistic models of the processes involved. In particular, I have addressed these questions:

- How can we realistically model the heterogeneity of the stress field produced by large earthquakes, and how does this heterogeneity affect the distribution of aftershocks in space and time?
- How should aleatoric and epistemic uncertainties be treated in the models?
- What is the role of time dependent stresses in the postseismic phase in triggering aftershocks?

The main features of the models and a description of the case studies are presented in Chapter 2. In Chapter 3, I address the first two questions by performing a sensitivity study of the input data used in Coulomb

stress calculations. I focus on the following aspects: the existence of multiple receiver faults; the stress heterogeneity within grid cells, due to their finite size; and errors inherited from the coseismic slip model. I introduce a methodology to include uncertainties in the final forecast, taking into account the distinction between aleatoric and epistemic uncertainties.
Another aspect which has so far been overlooked in CRS models is the effect of postseismic stress changes, which I address in Chapter 4. I focus in particular on two processes: creep on the mainshock fault plane (afterslip), and secondary triggering by previous aftershocks. In Chapter 5 I present preliminary results from a retrospective experiment which is currently being carried out by CSEP. Computational aspects of the work are presented in Chapter 6, while conclusions and future directions are discussed in Chapter 7.

2

IMPLEMENTATION OF COULOMB RATE-AND-STATE MODELS

In this chapter, I introduce the theory behind two main elements of Coulomb-rate-and-state models: calculation of Coulomb stress changes and rate-and-state seismicity evolution. I describe various aspects of the model implementation, such as the inversion of rate-and-state parameters and the estimation of background seismicity rate. Furthermore, I describe the datasets used in Chapter 3 and Chapter 4.

The material presented in this chapter appears in the following articles:

- **Cattania, C.**, S. Hainzl, L. Wang, F. Roth, and B. Enescu, Propagation of Coulomb stress uncertainties in physics-based aftershock models, *J. Geophys Res.*, *119*, 7846–7864, doi: 10.1002/2014JB011183, 2014.
- **Cattania, C.**, S. Hainzl, L. Wang, B. Enescu, and F. Roth, Aftershock triggering by postseismic stresses: a study based on Coulomb-Rate-and-State models, *J. Geophys Res.*, *in press*, doi: 10.1002/2014JB011500, 2015.
- **Cattania, C.**, and F. Khalid, A parallel code to calculate seismicity evolution induced by time dependent, heterogeneous Coulomb stress changes, *in preparation for submission to Computers and Geosciences*.

2.1 Coulomb stress changes

According to the Mohr-Coulomb criterion, failure on a plane is promoted by an increase in shear stress (τ); on contrary, an increase in normal stress (σ_{tot}) enhances the frictional force, thus inhibiting

failure. Therefore, a useful quantity to predict how a change in the local stressing state affects seismicity is the change of Coulomb Failure Stress, defined as

$$\Delta CFS = \Delta\tau - \mu\Delta\sigma_{tot} \tag{2.1}$$

with μ the coefficient of friction. The total normal pressure on the fault, σ_{tot}, is given by $\sigma_{tot} = \sigma - p$, where σ is the externally applied normal pressure and p is the pore pressure. Different models exist to describe how pore pressure changes in response to applied stresses; I use the apparent friction poroelastic model (*Cocco and Rice* 2002 and references therein), which gives $\Delta p = B\Delta\sigma$, with B the Skempton coefficient. This yields

$$\Delta CFS = \Delta\tau - \mu'\Delta\sigma \tag{2.2}$$

with an effective friction coefficient $\mu' = \mu(1 - B)$. The value of μ' is a fixed input parameter.
Unless otherwise specified, I calculate stress fields using the solutions for rectangular dislocations in an elastic half space presented by *Okada* [1992]. In order to avoid the singularities of the Okada solutions, I follow the common approach of imposing a cut-off value for ΔCFS: I set a value of 10 MPa for Tohoku and 1 MPa for Parkfield, so that only a small number of grid points is affected.

2.2 Rate and state evolution of seismicity

While the first-order behaviour of rocks is well described by the Mohr-Coulomb failure criterion, experimental studies indicate that the coefficient of friction μ presents small variations depending on slip, slip rate, contact time and stressing history. The empirical results describing these dependencies are included in the framework of rate-and-state dependent friction. A widely used form, introduced by *Dieterich* [1981] and *Ruina* [1983], is the following:

$$\mu = \mu_0 + A \log \frac{v}{v_0} + B \log \frac{\theta}{\theta_0} \tag{2.3}$$

where v is the sliding velocity; μ_0, A and B are experimentally determined coefficients; and θ is a state variable which depends on time, slip and normal stress. Rate-and-state dependent friction has been used

to reproduce a range of sliding regimes, including creep processes and earthquake nucleation.
In order to calculate changes in seismicity rates caused by applied stresses, *Dieterich* [1994] considered the collective behaviour of an infinite population of faults governed by Eq. 2.3. The seismicity rate R is found to evolve according to

$$R(t,x) = \frac{r_0(x)}{\gamma(t)\dot{\tau}_r} \tag{2.4}$$

with r_0 the background rate, $\dot{\tau}_r$ the constant shear stressing rate and γ a constitutive parameter which evolves according to

$$d\gamma = \frac{1}{A\sigma}\left[dt - \gamma dS\right] \tag{2.5}$$

with t time, $S = \tau - (\mu - \alpha)\sigma_{tot} = \tau - \mu''\sigma$, where α is a positive non-dimensional constitutive parameter [*Linker and Dieterich*, 1992] and $\mu'' = (\mu - \alpha)(1 - B)$. For simplicity, Coulomb-rate-and-state models (henceforth referred to as CRS models) usually assume $\mu'' = \mu'$, so that S is the Coulomb stress as defined above. I set $\mu' = 0.3$ unless otherwise specified. A related parameter is the aftershock duration time, given by

$$t_a = \frac{A\sigma}{\dot{\tau}_r} \tag{2.6}$$

which controls the time taken for seismicity to return to background level following an instantaneous stress step [*Dieterich*, 1994].
Different sources of stresses play a role during and after a mainshock: (1) coseismic (static) stresses induced by the mainshock deformation; (2) dynamic stresses due to the passage of seismic waves; (3) stresses caused by postseismic processes such as afterslip. *Belardinelli* [2003] showed that faults governed by rate-and-state friction exhibit nearly instantaneous triggering following dynamic stress changes, making static and post-seismic stresses the most important source of stress to consider in the days to months following a mainshock.

2.3 Model implementation

Fig. 2.1 describes the work flow of the model. Two tasks are performed: first, the optimal rate-and-state parameters $(A\sigma, t_a, r_0)$ are found; then, these parameters are used to produce a forecast. The forecast time

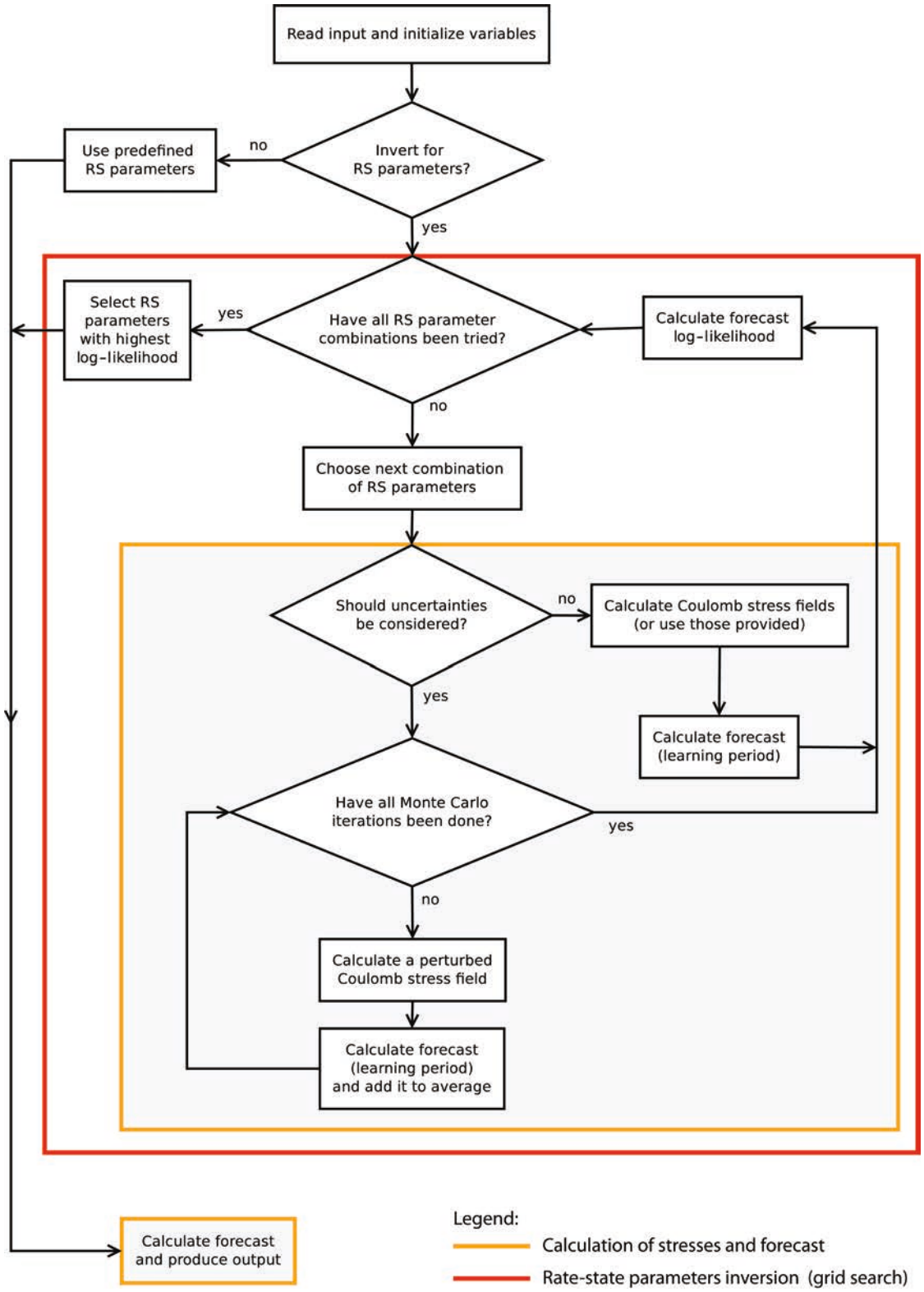
Read input and initialize variables
Invert for RS parameters?
no
Use predefined RS parameters
yes
Have all RS parameter combinations been tried?
yes
Select RS parameters with highest log-likelihood
Calculate forecast log-likelihood
no
Choose next combination of RS parameters
Should uncertainties be considered?
no
Calculate Coulomb stress fields (or use those provided)
yes
Calculate forecast (learning period)
Have all Monte Carlo iterations been done?
yes
no
Calculate a perturbed Coulomb stress field
Calculate forecast (learning period) and add it to average
Calculate forecast and produce output
Legend:
Calculation of stresses and forecast
Rate-state parameters inversion (grid search)

Figure 2.1

period may be in the future with respect to the optimization period (prospective or pseudo-prospective study), or overlap (retrospective study); while in this case the output is not strictly a forecast, I use the term for simplicity.
Optimal rate-and-state parameters are fitted to the earthquake catalogue by maximizing the log-likelihood, which is defined as the logarithm of the probability of the observed outcome (the earthquake catalogue) given a specified model. Given equal a priori probability, Bayes theorem implies that models with higher log-likelihood are more likely to be correct [*Ogata*, 1983]. For a stationary Poisson process, the log-likelihood is defined as:

$$LL = \sum_{j}^{N} \log\left[R(\mathbf{x}_j, t_j)\right] - \int_{t_0}^{t_1}\int_{volume} R\,(\mathbf{x}, t)\; d\mathbf{x}dt \tag{2.7}$$

where R is the model rate and $(\mathbf{x}_j, t_j)$ are the location and time of the observed earthquakes; t_0 and t_1 are the start and end time of the forecast. The values of $R(\mathbf{x}_j, t_j)$ depend on the exact location of the observed events. In order to account for the uncertainty in earthquake location, I smooth the position over a set of grid points, assuming a Gaussian distribution with standard deviation in the horizontal and vertical position as given in the catalogue.
The spatially averaged value of background rate r_0 which maximizes the log-likelihood can be found analytically: this approach is the most suitable when the background rate is not well constrained (as done in Chapter 5). In Chapter 3 and Chapter 4, I instead fix this parameter to a value estimated from the seismicity catalogue, in order to reduce the number of free parameters. I use a simple grid search algorithm to find the optimal values for $A\sigma$ and t_a, as described in *Hainzl et al.* [2009] (Appendix A1).

2.3.1 Background seismicity rate

The steady state seismicity rate $r_0(x)$ in Eq. 2.4 represents the seismicity rate at constant background stressing rate, and it is in general space dependent; the background rate has been shown to play a first order control on the spatial distribution of aftershocks [*Bhloscaidh et al.*, 2014], and to significantly affect the behaviour of CRS models (as discussed in Chapter 4 and Chapter 5).

Spatially uniform background rate

While unrealistic, this modelling choice may be the most suitable for regions with low seismicity, where a stable estimation of the space dependence of r_0 is not possible. *Cocco et al.* [2010] showed that CRS models with a non-homogeneous background rate are more sensitive to the details of the stress field; thus the uncertainties in the background model may be amplified. Moreover, using an homogeneous background rate facilitates the interpretation of the effect of other aspects, which are the main focus of the following studies. This is the approach I take throughout most of this thesis (Chapter 3 and Chapter 4). I estimated the spatially homogeneous background rate from the seismicity catalogue up to the time of the mainshock, as described in section 2.5.

Spatially non-uniform background rate

The capability of using a non-uniform background rate from a smoothed seismicity catalogue is also implemented, and this aspect is tested in Chapter 4 and Chapter 5. By definition, a declustered catalogue should be used when calculating the background rate. I use the Knopoff-Gardner [*Gardner and Knopoff*, 1974] method: after each earthquake exceeding a threshold magnitude, all earthquakes within a magnitude dependent spatial and temporal window are removed. The drawback of this method, compared to stochastic declustering algorithms, is that background events occurring during aftershock sequences are also removed. To obviate this problem, one should consider that at a location which falls within declustering window of overall duration T_d, the earthquakes left after declustering occur in a time period $T_{tot} - T_d$, where T_{tot} is the catalogue duration. Therefore, each earthquake left after declustering is given a weight $w = T_{tot}/(T_{tot} - T_{ds})$, where T_{ds} is the total time covered by aftershock time windows. Figure 2.2 shows an demonstration of how this method improves the estimation of r_0. After declustering, the catalogue is used to estimate the background rate using the 2D smoothing algorithm introduced by *Helmstetter et al.* [2007], which consists of smoothing each earthquake across grid points with a Gaussian distribution with standard deviation proportional to the distance to the second nearest earthquake. The distribution of seismicity with depth is estimated by counting the number of events within each depth layer; while in principle the spatial distribution could be calculated by applying the smoothing algorithm on the 3D grid, I find that a more robust estimation is obtained by separating the horizontal and vertical dimensions.

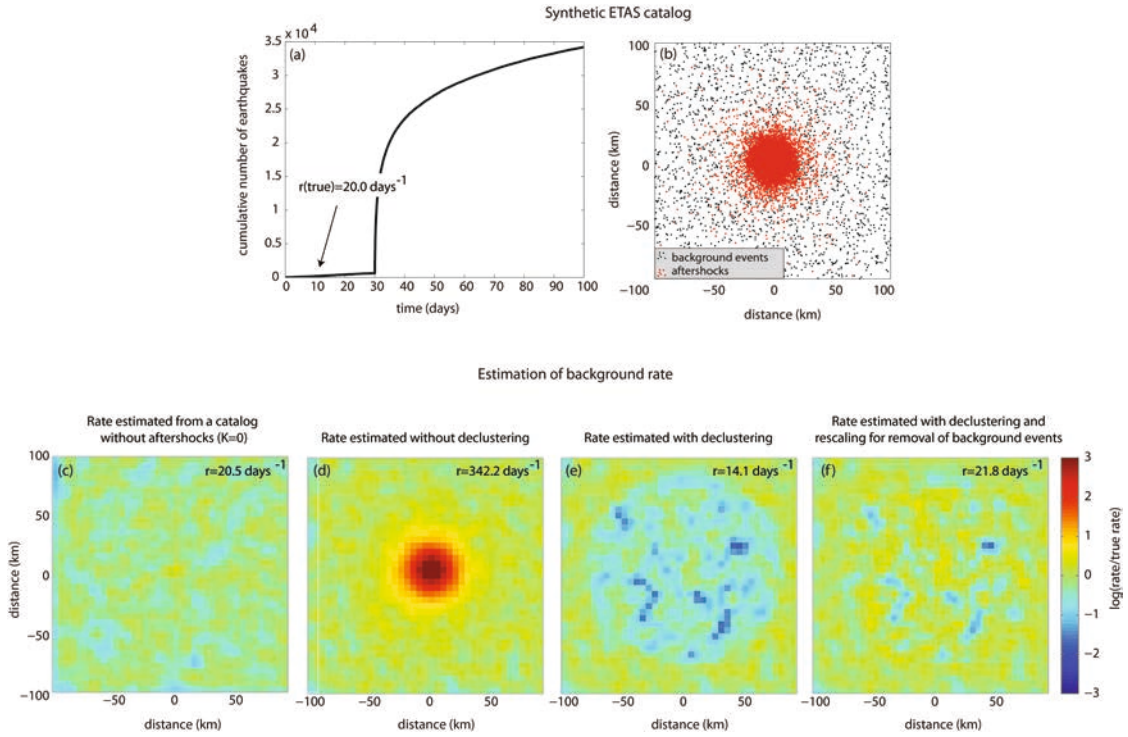

Figure 2.2: *Calculation of the non uniform background rate from a synthetic ETAS catalogue, with a mainshock of M_w7.0 at $t = 30$ days. (a) Temporal distribution of seismicity; (b) Spatial distribution; (c-f) Background rate estimated as follows: (c) from background events only; (d) from entire, non-declustered catalogue; (e) from declustered catalogue, without accounting for removal of background events; (f) from declustered catalogue, with remaining events rescaled to account for removal of background seismicity. The differences between (c) and (f) are due to the fact that only 30 days of data are used for the central region in (f), making the background rate estimation less robust.*

2.4 Evaluation of model performance

The log-likelihood (Eq. 2.7) is used to assess the ability of a model to describe a seismic sequence. To compare models against each others, I use the average difference in log-likelihood (information gain):

$$I = \frac{LL_1 - LL_0}{N} \tag{2.8}$$

where LL_1, LL_0 are log-likelihoods of the models, and N the total number of aftershocks. To quantify how models differ in their ability to forecast specific events, I consider the information gain of single aftershocks:

$$\begin{aligned} I_{ev} &= LL_{1,i} - LL_{0,i} = \\ &= \log(R_1(x_i, t_i)) - \log(R_0(x_i, t_i)) + \\ &\quad - \int_{t_{i-1}}^{t_i} \int_{volume} [R_1(\mathbf{x}, t) - R_0(\mathbf{x}, t)] \, d\mathbf{x}dt \end{aligned} \tag{2.9}$$

A related quantity is the ratio of probabilities between models (or probability gain), given by $G = \exp(I_{ev})$. This quantity has a more intuitive physical interpretation, since it is proportional to the ratio of the probabilities of individual events between models.

2.5 Case studies

In Chapter 3 and Chapter 4 I focus on two case studies from different tectonic settings: the Parkfield, M_w6.0 strike slip earthquake and the Tohoku, M_w9.0 megathrust event, both of which have well recorded aftershock sequences and for which several input slip models are available.

2.5.1 Parkfield

The M_w6.0 Parkfield earthquake occurred on 28/09/2004, rupturing a portion of the San Andreas fault located between a creeping and a locked section (to the north-west and the south-east respectively). The region was extremely well instrumented, providing high quality data sets of seismicity and crustal deformation in the coseismic and postseismic phase. The Parkfield was followed by significant afterslip, larger than other events of a similar rupture style and size: the cumulative afterslip moment was of the same order as the coseismic moment. Most of the aftershocks were located on the mainshock fault, but events also occurred in a cluster at ≈ 50 km south-west of mainshock, as well as on north-east side of the fault.

Data

For these study, I considered the area shown in Fig. 2.3. I used the independent coseismic and afterslip model of *Wang et al.* [2012b], based on Bayesian inversion of GPS data; the earthquake catalogue is a combination of the ANSS catalogue and the more complete catalogue of *Peng and*

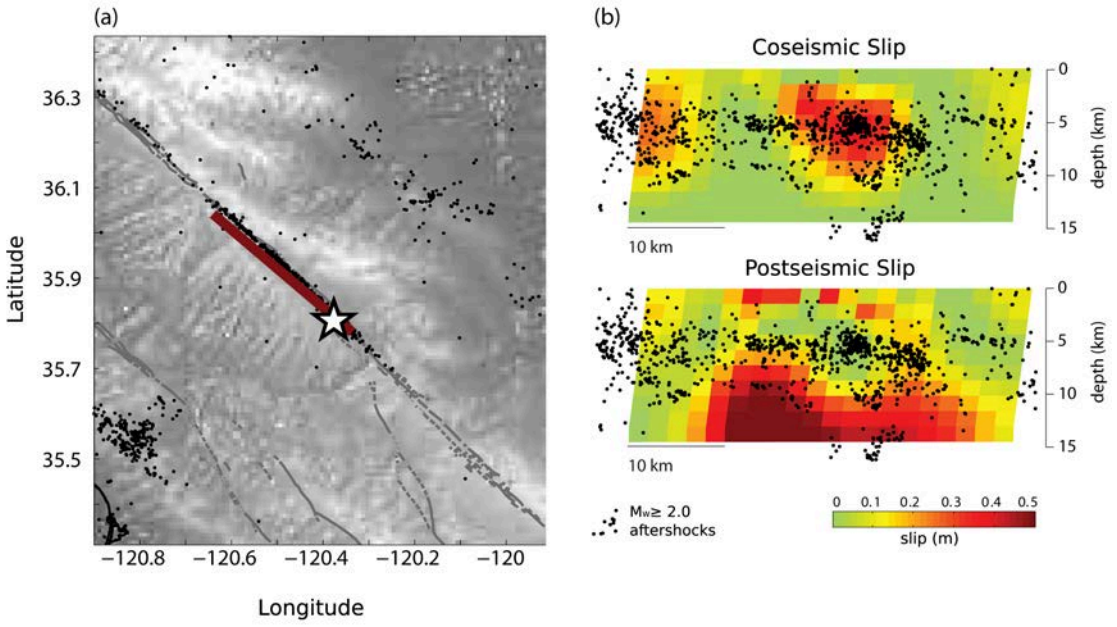

Figure 2.3: *Map of the aftershock region of the September 2004 Parkfield earthquake. (a) Map view of $M_w \geqslant 2.0$ aftershocks in the first 250 days, with surface rupture marked by the red line; (b) Coseismic and postseismic slip models from Fig. 4 of Wang et al. [2012b], with aftershocks superimposed.*

Zhao [2009] for the first 2 days. The combined catalogue has a completeness of $M_c = 2.0$ starting from 100 s after the mainshock [*Peng and Zhao*, 2009]. I only fit data starting from the time of completeness, up to 250 days from the mainshock. I estimate the background rate based on the ANSS catalogue from 1970, up to the mainshock: rates are calculated for time windows of 30 days and 1 yr, and the background rate of $0.22\ d^{-1}$ is found visually ignoring increased values after large ($M_w \geqslant 6.0$) events. Due to the ongoing aftershock sequence of the San Simeon earthquake, the rate at the time of the Parkfield mainshock is higher than the background rate. I test the effect of this by starting the model with a non steady-state rate of $r(0) = 1.144\ d^{-1}$, and find no significant difference in model behaviour: the results presented here are based on a background rate of $r_0 = 0.22\ d^{-1}$ for the area in Fig. 2.3 and depth range between [0.5, 13.5] km.

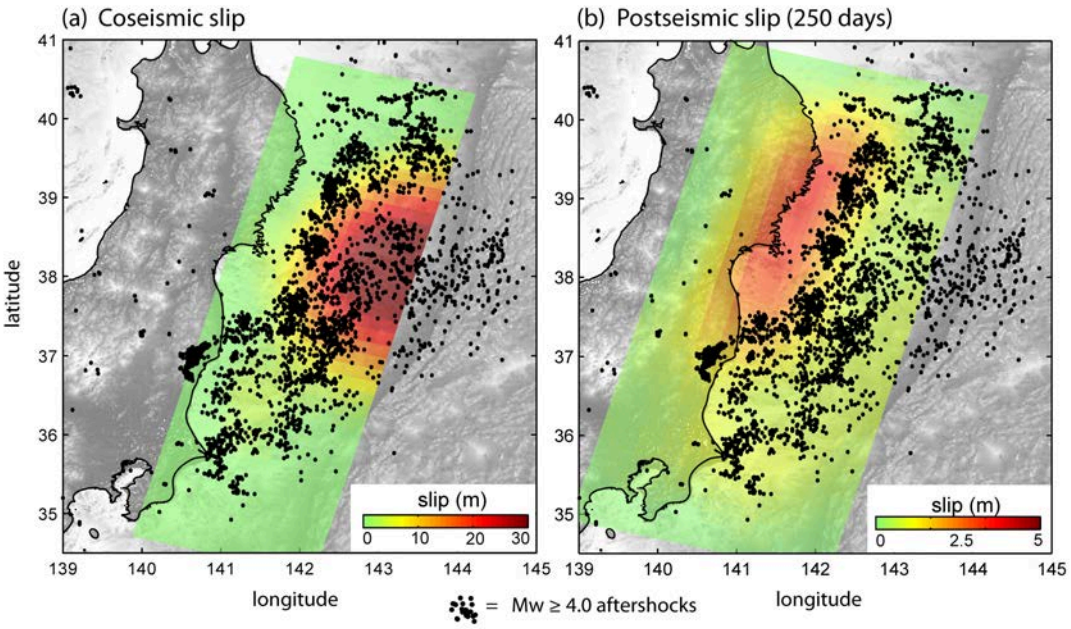

Figure 2.4: *Map of the aftershock region of the March 2011 Tohoku earthquake. (a) Coseismic slip; (b) Cumulative afterslip after 250 days. Both slip models are from Wang et al. [2013]. Black dots are* $M_w \geqslant 4.0$ *aftershocks between 5 and 250 days.*

2.5.2 Tohoku

The $M_w 9.0$ Tohoku event was a thrust earthquake which ruptured the subduction interface between the Pacific and the North America plates. It was followed by intense aftershocks activity with an along strike extent of 500 km; aftershocks were mostly located within 20 km of the fault interface, but numerous normal faulting events occurred in the outer rise and on the overriding plate. The afterslip following the Tohoku had a moment corresponding to $M_w 8.3$, and was located downdip of the coseismic rupture. The seismic moment ratio between coseismic and postseismic slip, as well as the location of afterslip, are typical of afterslip following megathrust earthquakes.

Data

The model domain corresponds to the area shown in Fig. 2.4, and a depth range between [3.0, 42.0] km. I used the catalogue provided by the Japan Meteorological Agency. I estimate a completeness magnitude of $M_c = 4.0$ starting from 5 days after the mainshock: also in this

case, I limit the study to the time period in which the catalogue is complete, up to 250 days from the mainshock. I used the GPS based slip models of *Wang et al.* [2013], which uses the same geometry as *Pollitz et al.* [2011]; as well as a set of alternative coseismic slip models presented in Chapter 3. In Chapter 4, I present the sensitivity of the results to the choice of afterslip model by repeating the calculations for Tohoku using the coseismic and postseismic slip models of *Perfettini and Avouac* [2014].

3

PROPAGATION OF COULOMB STRESS UNCERTAINTIES

Despite the successes of Coulomb hypothesis and of the rate-and-state formulation, CRS models perform worse than statistical models in an operational forecasting context: one reason is that Coulomb stress is subject to large uncertainties and intrinsic spatial heterogeneity. In this chapter, I characterize the uncertainties in Coulomb stress inherited from different physical quantities, and assess their effect on CRS models. I use a Monte Carlo method, and consider the following aspects: the existence of multiple receiver faults; the stress heterogeneity within grid cells, due to their finite size; and errors inherited from the coseismic slip model. The existence of multiple receiver faults is found to be the most important source of intrinsic stress heterogeneity, and CRS models perform significantly better when this variability is taken into account. The choice of slip model also generates large uncertainties. An ensemble model is constructed based on published slip models, and is found to outperform individual models. These findings highlight the importance of identifying sources of errors and quantifying confidence boundaries in the forecasts; moreover, I demonstrate that consideration of stress heterogeneity and epistemic uncertainty has the potential to improve the performance of operational forecasting models.

Most of the material presented in this chapter has been published in the following article:

- **Cattania, C.**, S. Hainzl, L. Wang, F. Roth, and B. Enescu, Propagation of Coulomb stress uncertainties in physics-based aftershock models, *J. Geophys Res.*, *119*, 7846–7864, doi: 10.1002/2014JB011183, 2014.

3.1 Introduction

Coulomb stress calculations require several simplifications, and various sources of errors are present in the input data. These include: uncer-

tainties and finite resolution of the slip model; small scale variability of elastic parameters in the crust; lack of knowledge of the orientation of the faults that can accommodate future seismicity; discretization of the crust into cells of finite volume.

While a simple treatment may be sufficient to demonstrate a qualitative agreement between the distribution of seismicity and ΔCFS, careful consideration of uncertainties is required in order to construct models which are useful in the context of operational earthquake forecasting. Due the to strong non-linearity, of the rate-and-state equations, CRS models are very sensitive to variability in input stress values, and several authors have shown that including stress variability leads to a significantly different spatio-temporal distribution of seismicity.

Marsan [2006] and *Helmstetter and Shaw* [2006] demonstrated that small scale variability can lead to the suppression of stress shadows in the short term, a result that can be understood from the fact that, according to the rate-and-state constitutive law, seismicity rate increases exponentially with stress change immediately after a stress step, and hence the largest values of a distribution dominate at short times. Therefore, small scale variability can explain the observation of early aftershocks in areas which experience an average negative stress, including the vicinity of the rupture area on the mainshock fault. Stress variability also affects the temporal evolution of seismicity. In the rate-and-state formulation, seismicity following a positive stress step is predicted to decay following an Omori law with $p = 1$ and c dependent on the value of stress change: due to the variability in c value, an effective value of $p < 1$ is observed when stresses of different magnitude are included [*Helmstetter and Shaw*, 2006]. These results indicate that a careful treatment of the variability in Coulomb stress may be a critical aspect for CRS models aimed at forecasting aftershock sequences. In fact, *Hainzl et al.* [2009] showed that when Coulomb stress uncertainties are included in CRS models of the Landers, 1992 M_w7.3 aftershock sequence, the correlation with observed seismicity improves and the inversion of rate-and-state parameters is more stable. They estimated uncertainties of ΔCFS by comparing the stress field obtained from existing published slip models, and they found the standard deviation of ΔCFS to be spatially similar to the absolute stress change: therefore, they modeled uncertainties by assuming a spatially constant Coefficient of Variation (CV, the ratio between standard deviation and absolute value). While this approach has the advantage of being simple to implement, it has few drawbacks: it introduces a new parameter (CV); and it may not provide an accurate spatial description of the variability of the stress field, as pointed out by *Woessner et al.* [2012].

My goal is to present methods by which uncertainties can be included

into CRS models in a physically meaningful way, and to perform an assessment of the variability of ΔCFS and its effect on the forecasts of aftershock sequences. I estimate uncertainties in input quantities by using prior information about fault orientation and slip characteristics, and I explicitly propagate them through the model using Monte Carlo simulations, thus without making any prior assumption on the distribution of ΔCFS. I focus on three sources of uncertainty: (1) the choice of receiver faults on which the stress tensor is resolved; (2) the existence of a range of stress values within each cell, due to its finite volume; (3) uncertainties in the slip models, due both to its finite resolution and to modelling assumptions such as choice of geometry or inversion method. In section 3.2, I present methods to model the variability of ΔCFS: to model the presence of multiple receiver fault orientations, I sample the distribution of past focal planes; I then consider the effect of finite resolution of the calculation grid, and suggest two techniques to reproduce this aspect of stress heterogeneity; finally, I outline methods to reproduce the effect of slip model uncertainties by adding a synthetic, small scale slip and by comparing the output from different published slip models. In section 3.3, I study the effect of each source of uncertainty on the forecast of sequences following the Parkfield and the Tohoku earthquakes. After describing the sensitivity of the models to various sources of uncertainty, I discuss practical ways to combine this information into a single model, in particular drawing a distinction between aleatoric and epistemic uncertainties. In section 3.6, I test how these techniques affect model performance; a physical interpretation of these results, and their significance in the context of medium term earthquake forecasting, are discussed in the final part of the chapter.

3.2 Methods

I implement Coulomb-rate-and-state models as described in Chapter 2. In order to study the effect of stress variability on a sub-grid scale and the use of different slip models, I use a Monte Carlo technique: I create 100 perturbed versions of the stress field and calculate the spatio-temporal distribution of seismicity for each iteration from the rate-and-state equations. The perturbed stress fields are obtained based on physical consideration of different sources of uncertainties, as described below.

3.2.1 Receiver Fault Orientation

In principle, the total seismicity in a region of the crust should be obtained by adding the contribution from each of the fault planes in that volume, assuming that earthquakes occur on pre-existing fault planes. However, it is in practice not possible to have a complete knowledge of all the faults. The two most commonly adopted assumptions are the following: (1) all events have the same focal plane orientation as the mainshock; (2) earthquakes rupture along optimally oriented Coulomb failure planes (OOP), on which the total (background + coseismic) Coulomb stress is maximum. The first approach oversimplifies the geometry of most fault systems, in which faults exist with different orientation from the mainshock. The second approach leads in general to more successful forecasts [*Cocco et al.*, 2010]; however, it relies on the assumption that faults exist everywhere with the optimal orientation, and that only these faults will produce earthquakes. Considering only the contribution of the optimally oriented fault at each grid point is not consistent with rate-and-state modelling: while in this framework seismicity is predicted to be dominated by the largest ΔCFS values at short times ($t \ll t_a$), the contribution of faults with lower ΔCFS would have an impact at later times [*Helmstetter and Shaw*, 2006].
In order to account for the presence of multiple fault orientations, I use the catalogue of past focal mechanisms in the area of interest, assuming that past focal planes provide a reliable sample of the existing fault structures. I use both possible plane solutions of the catalogue as possible rupture planes. Since the direction of slip on a pre-existing plane depends on the external field, I only use the strike and dip values from the catalogue, and choose the rake for which shear stress τ is highest. For Tohoku, I use a differential stress of 20 MPa [*Hasegawa et al.*, 2011], with orientation such that the mainshock mechanism (strike=195°; dip=10°; rake=88°) is optimally oriented; for Parkfield, the differential stress is 10 MPa [*King et al.*, 1994], and the mainshock plane (strike=330°; dip=89°; rake=180°) is optimally oriented.

Focal mechanism catalogues

For Parkfield, I use the catalogue of focal mechanisms from Yang, Haukkson and Shearer [*Yang et al.*, 2012]. I select events occurring between the start of the catalogue (1/1/1981) and the time of the mainshock; I also perform spatial selection, using the spatial window corresponding to Fig. 3.1, and use only events with $M_w \geqslant 2.0$, giving a total of 81 focal mechanisms. I investigate whether spatial trends in the orientation of these focal planes exists, and I find a rather homogeneous spatial

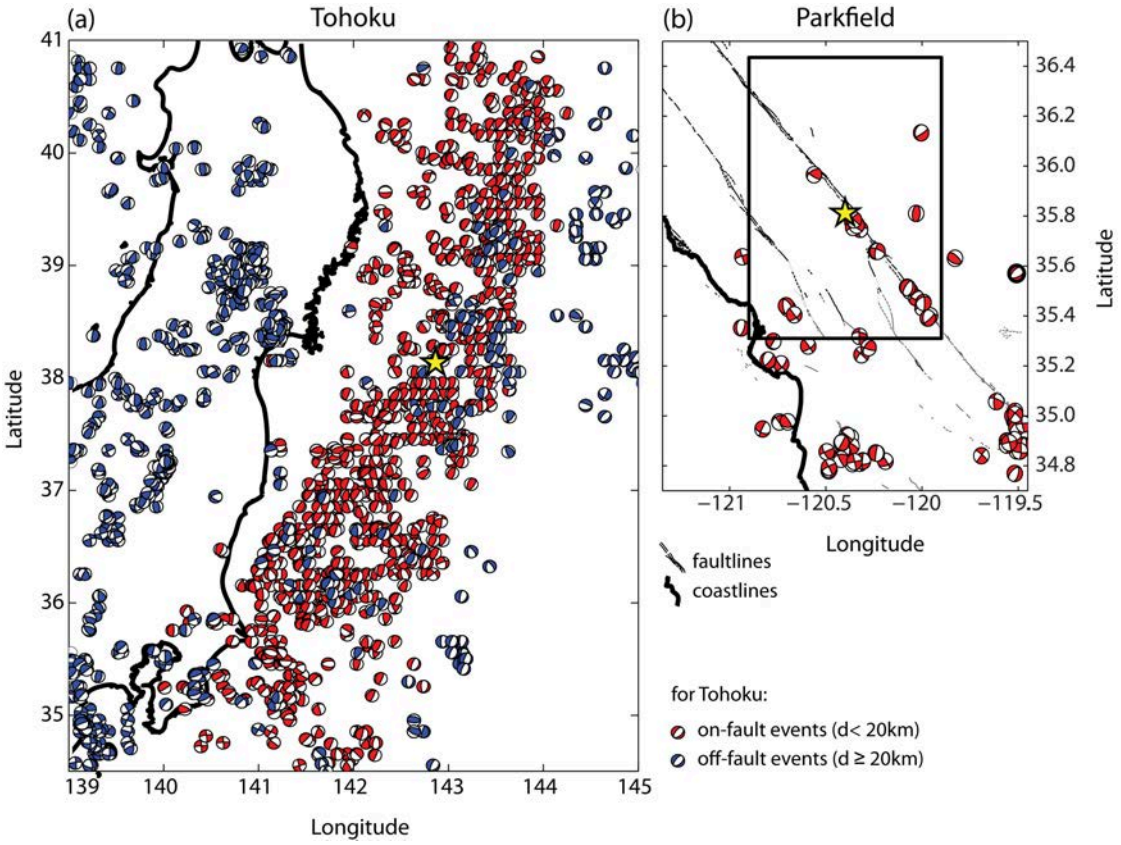

Figure 3.1: *Maps of focal mechanisms in the area of the two mainshocks, used as a set of receiver faults on which Coulomb stresses are resolved. (a) Focal mechanisms of* $M_w \geqslant 3.1$ *events in the area of the Tohoku earthquake, between February 1997 and the mainshock. Events are colour coded by distance from the fault: red events are considered on-fault* ($d < 20$ *km), those in blue are the intra-plate events. This selection has been done from the observed clustering of focal mechanisms parameters (strike, dip) in Fig. 3.2a. (b) Focal mechanisms of* $M_w \geqslant 2.0$ *events in the Parkfield area, between 1/1/1981 and the time of the mainshock. The box in the Parkfield map indicates the model domain, and the depth range is [0.5, 13.5] km; for Tohoku, the entire area is the model domain, and the depth range is [3.0, 42.0] km. The choice of these areas was dictated by the distance at which corresponding Coulomb stresses are significant.*

distribution of focal mechanisms (as confirmed by Fig. 3.1b and 3.2b): therefore, I sample the entire set of focal planes at each grid point.
For Tohoku, I use the F-net moment-tensor focal mechanism solutions [*Okada et al.*, 2004], determined and provided by the National Research Institute for Earth Science and Disaster Prevention, Japan, and containing events of $M_w \geqslant 3.1$ from February 1997. The total number of focal mechanisms preceding the Tohoku earthquake is 2626. Compared to the Parkfield case, I find here a non uniform spatial distribution of focal mechanisms, due to the larger area considered and to the presence of a wider range of fault structures, such as the subduction interface, splay faults, and intra-plate faults in the hanging and foot wall [*Asano et al.*, 2011]; in particular, I distinguish different distributions of strike and dip for subduction related events, and intra-plate events on each side of the subduction interface (Fig. 3.2a). In order to capture the local variability of receiver faults, I divide the catalogue into three groups based on Fig. 3.2a: events in the foot wall, at a distance $d > 20$ km below the fault (208 events); events in the hanging wall, at $d > 20$ km from the fault (588 events); subduction related events, at $d < 20$ km (1830 events). The latest group includes a larger variety of focal planes, reflecting the coexistence of different fault structures within few tens of kilometres from the mainshock plane. At each grid point, receiver faults are sampled from one of these groups, depending on the grid point location.

3.2.2 Distribution of receiver faults

The use of focal planes as a proxy for existing fault structures is inevitably biased, due to the fact that past focal mechanisms reflect the external stress field: namely, fault planes which were favourably oriented will be sampled more often than structures which experienced lower stresses. In particular, past aftershock sequences may significantly bias the sample towards mechanisms which were favourably oriented following past stress changes. To verify if significant biases exist, I compare the distribution of focal planes prior to each mainshock (used as receiver faults) to the distribution of observed aftershock focal planes. Additionally, I test the hypothesis that aftershocks occur on optimally oriented planes by comparing observed planes to the OOPs calculated at corresponding locations.
Fig. 3.3 shows the distribution of focal planes for the area surrounding the Tohoku mainshock, for each of the three subsets described above. Visual inspection shows that aftershocks focal planes have a similar distribution to the previous seismicity in each of area. Both aftershocks

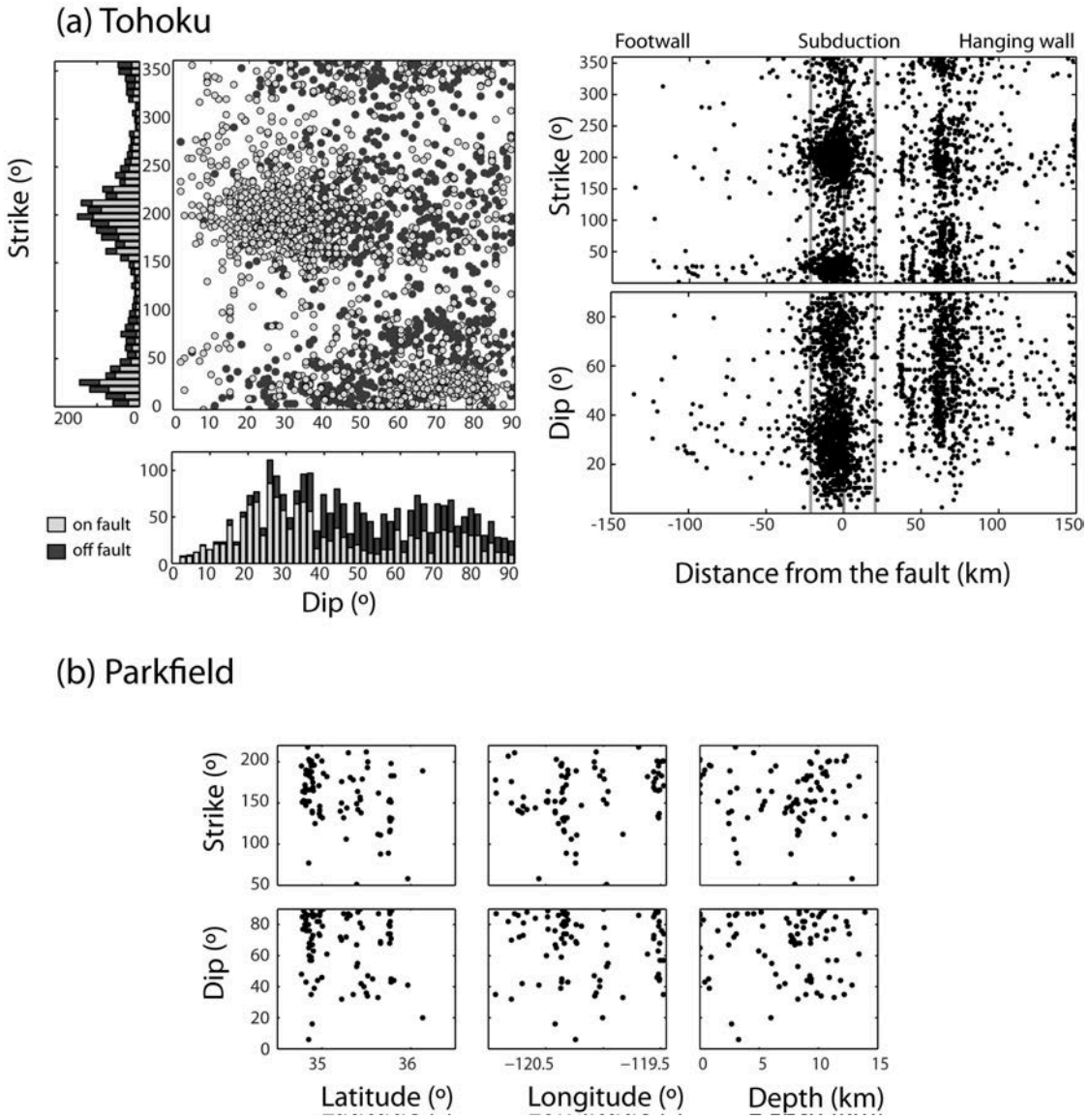

Figure 3.2: *Statistical distribution of focal planes parameters for the planes used as receiver faults shown in Fig. 3.1. (a) For Tohoku, I distinguish between three groups of events: within 20 km from the fault, more than 20 km above and more than 20 km below, based on changes in focal plane distributions displayed in the right panel. The left panel shows the distribution of strike and dip for on-fault and off-fault events (defined by the 20 km threshold); in particular, the distribution of dips shows a larger fraction of steep faults (dip= 40 — 90°) being activated further from the slab. (b) for Parkfield, strike and dip do not show clear spatial variations, and I do not distinguish between different zones.*

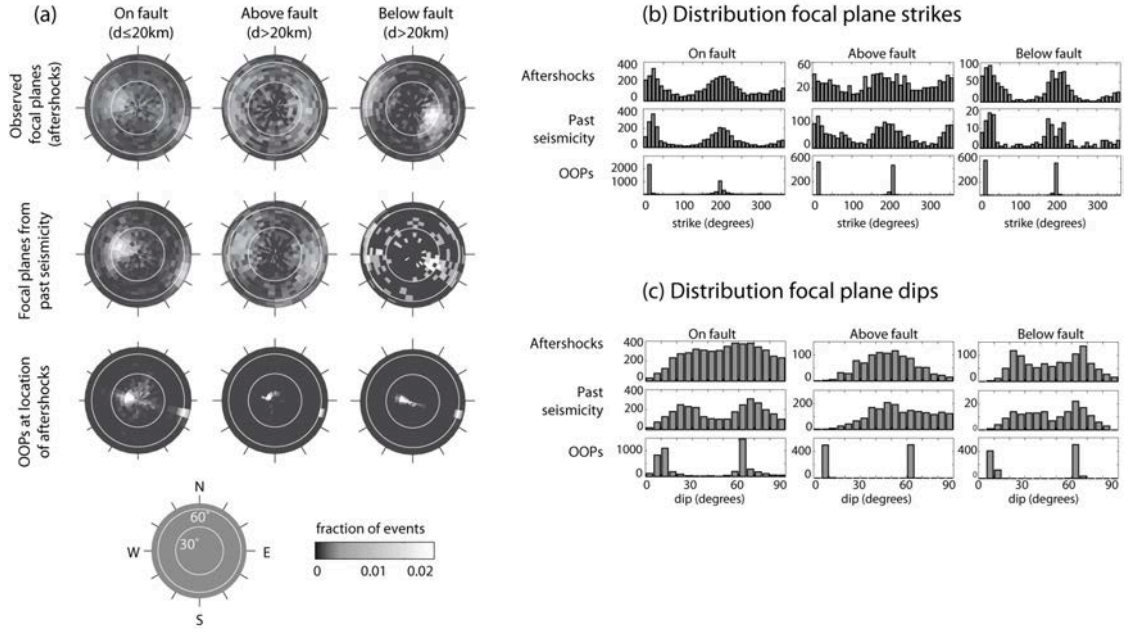

Figure 3.3: *Distribution of focal planes parameters for the Tohoku study area. Events are divided by their location relative to the fault; for each of the three sets, a comparison is made between events occurring before the mainshock, which I used as receiver faults; aftershocks occurring in the 250 days following the mainshock; Optimally Oriented Planes sampled at the locations of the aftershocks. (a) Spheres showing the normalized density of unit vectors perpendicular to focal planes, in map view. Right: histograms showing the distributions of strikes (b) and dips (c).*

and past events close to the subduction interface tend to cluster at strike 200° and dip $15-30°$, slightly steeper than the mainshock mechanism. On the other hand, Optimally Oriented planes are predicted to have a shallower dip, influenced by the background stress field. Away from the subduction interface, OOPs are, as expected, even more peaked around the optimal orientations of the background stress field, while aftershocks and past events exhibit a wider distribution of focal planes. Differences in the distribution of aftershock and previous focal planes can be seen, such as the activation of faults with a wider range in strike in the wedge during the aftershock sequence; however, despite these differences the use of orientations of past focal planes provides a more realistic description of the structures that will accommodate aftershocks than OOPs.

3.2.3 Finite cell volume

Uncertainties in CRS models also originate from discretization of the domain: the model expresses seismicity rates in a cell of finite volume, assuming that the value calculated at the enter is uniform throughout the cell. This is not the case, especially in the vicinity of the faults where gradients in ΔCFS are highest. The most direct method to address this problem is to sample each cell at multiple locations, by dividing the cell into smaller sub-cells; while simple to implement, this method leads to a fast growth of problem size and computational requirements. I therefore suggest an alternative method to obtain a first order estimate of the stress gradients within each cell, and hence the range of possible stress values. For each cell, I estimate the range of values as follows:

$$\begin{aligned} \delta_j &= (\Delta CFS_j - \Delta CFS_0)/2 \\ \Delta CFS_{min} &= \Delta CFS_0 + \min(\delta_j) \\ \Delta CFS_{max} &= \Delta CFS_0 + \max(\delta_j) \end{aligned} \tag{3.1}$$

where ΔCFS_0 is the value at the enter of the cell, and $j = 0, 1, ...6$ refers to the cell itself and the 6 neighbour cells. For each Monte Carlo iteration, I draw a value from the uniform distribution in the interval $[\Delta CFS_{min}, \Delta CFS_{max}]$. A synthetic test (Fig. 3.4) shows that the two methods yield similar distributions of stress values: in the remaining part of the chapter, results from the approximated method (Eq. 3.1) will be presented. The grid resolutions have been chosen based on the slip model patch size and the total domain size, so as to maintain computational costs reasonable. I used the following values: $0.1°$ (horizontal), 3 km (vertical) for Tohoku; $0.025°$ (horizontal), 1 km (vertical) for Parkfield.
In spite of the additional computational requirements of using a refined grid, I point out that grid refinement has the advantage that it does not require Monte Carlo iterations, and may therefore be the most suitable choice if no other source of uncertainty is included; moreover, it can also be used if a single depth layer is provided in the output forecast, as in CSEP experiments (see for example Chapter 5).

3.2.4 Slip Model uncertainties

The reliability of slip models is an important aspect to consider when modelling Coulomb stresses [*Hainzl et al.*, 2009; *Woessner et al.*, 2012]. Multiple sources of errors impact slip models, including: (1)

(a) Tohoku

Index	SrcMod identifier	Reference
1	-	Wang et al (2013)
2	s2011HONSHU01SHAO	Shao et al. (2011)
3	s2011HONSHU02SHAO	Shao et al. (2011)
4	s2011HONSHU03SHAO	Shao et al. (2011)
5	s2011HONSHU04SHAO	Shao et al. (2011)
6	s2011TOHOKU01FUJI	Fujii et al. (2011)
7	s2011TOHOKU01GUSM	Gusman et al. (2012)
8	s2011TOHOKU01HAYE	Hayes (2011)
9	s2011TOHOKU01IDEx	Ide et al. (2011)
10	s2011TOHOKU01LAYx	Lay et al. (2011)
11	s2011TOHOKU01SATA	Satake et al. (2013)
12	s2011TOHOKU01WEIx	Wei and Sladen (Caltech, Tohoku 2011)
13	s2011TOHOKU01YAMA	Yamazaki et al. (2011)
14	s2011TOHOKU01YUEx	Yue and Lay (2013)
15	s2011TOHOKU02FUJI	Fujii et al. (2011)
16	s2011TOHOKU02GUSM	Gusman et al. (2012)
17	s2011TOHOKU02SATA	Satake et al. (2013)
18	s2011TOHOKU02WEIx	Wei et al. (Caltech: Tohoku 2011)
19	s2011TOHOKU03SATA	Satake et al. (2013)
20	s2011TOHOKU03WEIx	Wei et al. (2012)

(b) Parkfield

Index	SrcMod identifier	Reference
1	-	Wang et al. (2012)
2	s2004PARKFI01DREG	Dreger et al. (2005)
3	s2004PARKFI01CUST	Custodio et al. (2005)
4	s2004PARKFI01JIxx	Ji (Caltech, Parkfield 2004)

Table 3.1: *List of input slip models. Figures of all slip models are shown in Fig. 3.5 and 3.6.*

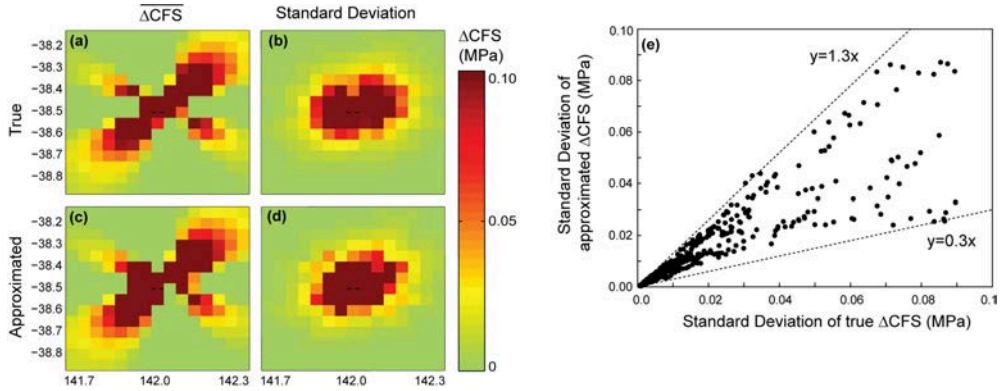

Figure 3.4: *Synthetic test comparing the distribution of stress values due to finite cell size. (a, b): mean and standard deviation of the distributions obtained from subdividing each cell into* 125 *sub-cells, by reducing the size by a factor of* 5 *in each dimension; (c, d): approximated values, obtained by first order estimation of stress gradients described in equation 3.1. (e): approximated standard deviations (obtained from estimating gradients) as a function of the real ones (obtained from the subdividing the cells), with each point corresponding to a cell: for* 95% *of the points, the approximated values differ from the true values by less than a factor of* 2*. The distributions are generated using a synthetic slip model of a strike-slip event of* M_w6.0 *on a fault with strike=*90°*, dip=*90°*, and the depth interval for stress calculations if* 4 *km.*

the non-uniqueness of the inversion; (2) incomplete and erroneous data; (3) inversion algorithm; (4) choice of fixed parameters, including fault geometry, fault discretization and smoothing; (5) choice of other physical quantities such as rupture speed and velocity structure. The sensitivity of slip models to these aspects is the subject of several studies [*Yagi and Fukahata*, 2011; *Hartzell et al.*, 2007; *Beresnev*, 2003], and it is becoming more common to provide slip models with estimates of uncertainties [*Sudhaus and Jónsson*, 2009]; techniques such as Bayesian inversion are increasingly being used to incorporate data errors and obtain a family of possible models [*Minson et al.*, 2013], which should be included in a forecasting model to estimate confidence limits. I will distinguish between two types of errors: the finite resolution of an individual slip model, and the differences between published slip models.

Sub-patch scale slip.

The resolution of a slip model is limited by the patch size and smoothing; and even when a slip model presents slip on isolated

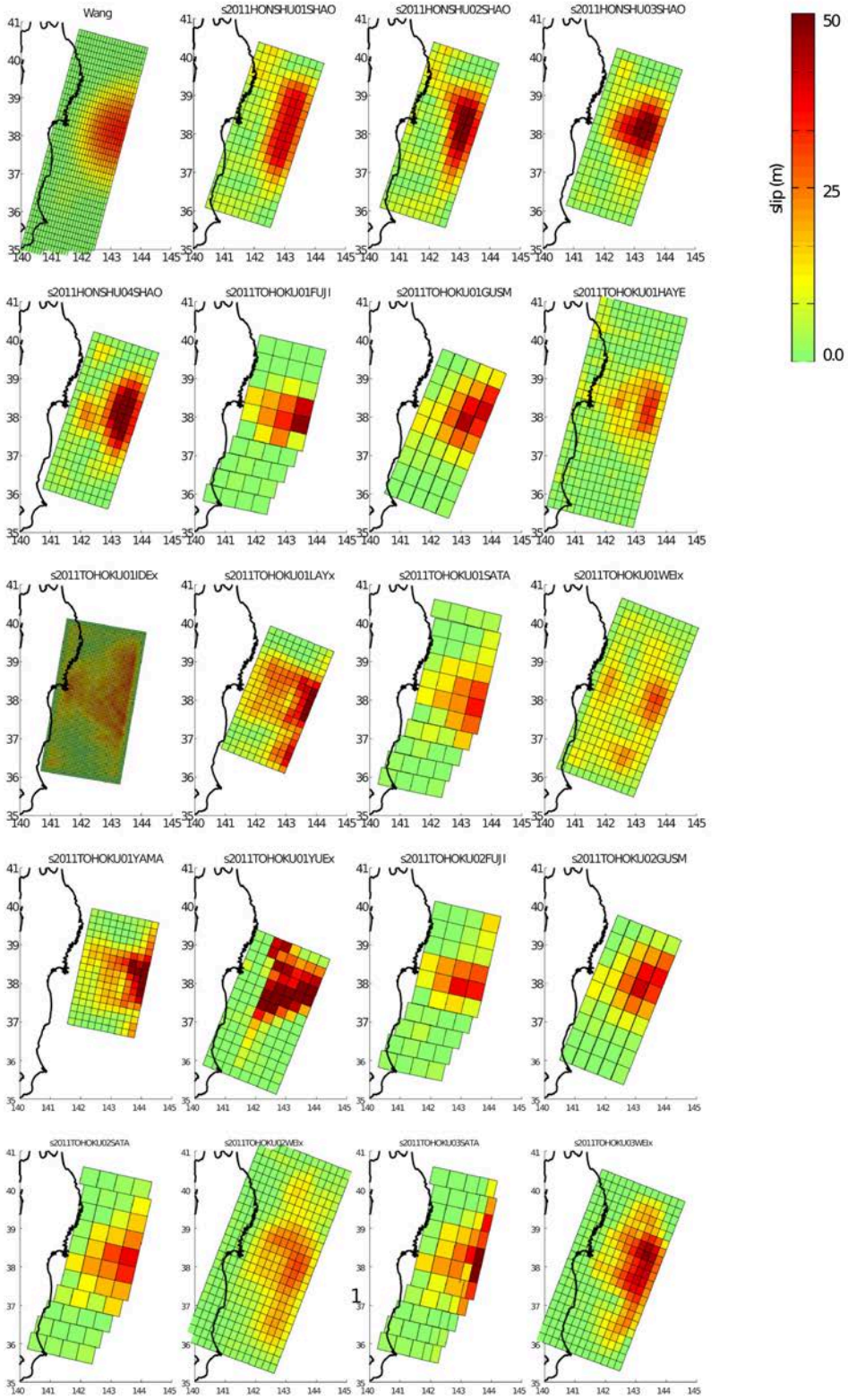

Figure 3.5: *Slip models used for Tohoku, available from the SrcMod database (http://equake-rc.info/srcmod/).*

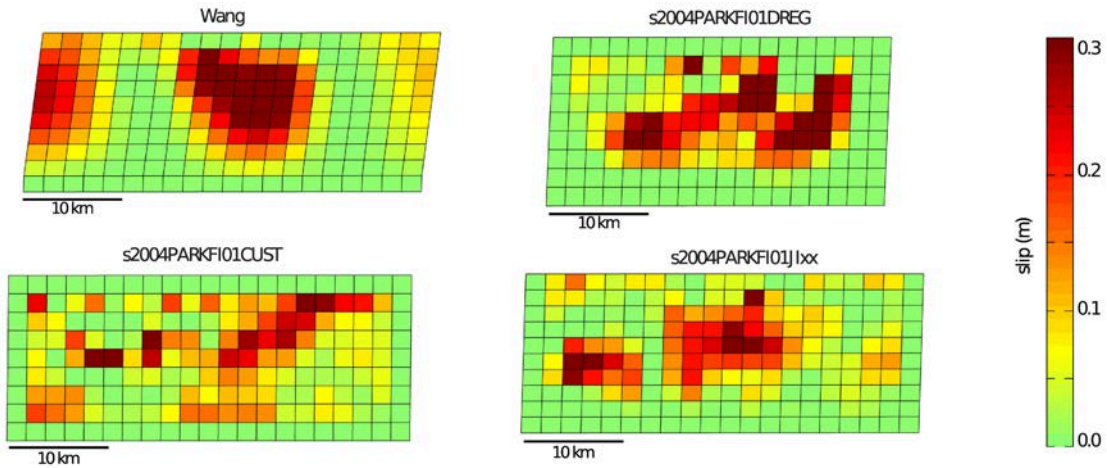

Figure 3.6: *Slip models used for Parkfield, available from the SrcMod database (http://equake-rc.info/srcmod/).*

patches, it can be a modelling artefact and has large uncertainties [*Hartzell et al.*, 2007; *Beresnev*, 2003]. In order to consider small scale slip, I create a set of possible slips by adding a random high frequency slip, while leaving the low frequencies unchanged. Several authors have suggested that slip is fractal, with power spectrum characterized by a power law decay: $P(k) \propto k^{-2(4-D)}$, with D the fractal dimension and k the wavenumber. I used the procedure described in *Kieling et al.* [2014] to create a set of slip models with synthetic slip at small wavelengths, while keeping the original slip distribution at wavelengths $k > k_c$, where k_c is the corner wavenumber given by $k_c = 10^{1.82-0.5M_w}$ [*Causse et al.*, 2010]; I chose a value of D=2.

Choice of slip model.

When adding synthetic, small wavelength slip, it is assumed that the original slip model is realistic in terms of geometry and large scale slip distribution. On the other hand, a number of different slip models exist for each mainshock, which can differ quite significantly. In order to study the sensitivity of CRS models to the input slip, I use a set of slip models from the finite-source model database: in total, I compare a set of 4 models for Parkfield and 20 models for Tohoku (Table 3.1, Fig. 3.5, 3.6).

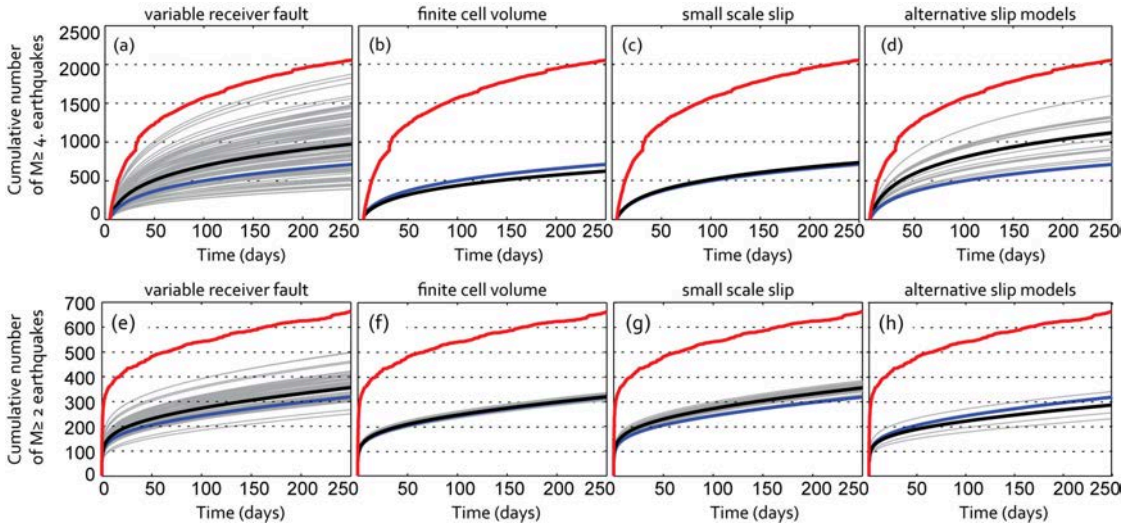

Figure 3.7: *Sensitivity test showing the cumulative number of events vs. time, with fixed rate-and-state parameters ($A\sigma = 28$ kPa, $t_a = 8000$ d for Tohoku, $A\sigma = 6$ kPa, $t_a = 10000$ d for Parkfield). Each thin line indicates a Monte Carlo iteration; the black line is their average; the red line is the observed seismicity; the blue line is the forecast obtained without any source of uncertainty (hidden by the black line in panels c and f). (a) Forecast for Tohoku, including variability in receiver faults; (b) including stress field gradients within each cell; (c) including sub-patch scale slip in the slip model; (d) using different published slip models. Figures (e) to (h): same as above, for Parkfield. For this test, rate-and-state parameters are not optimized, leading to the tendency to underestimate the total number of events.*

3.3 Model sensitivity to uncertainties

In order to assess the impact of different sources of uncertainty on the forecasted seismicity, I run models with each source of uncertainty included separately. I compare 5 models, with consideration of: (1) uncertainties from receiver fault orientation, (2) uncertainties from finite cell volume, (3) uncertainties from unresolved, small scale slip, (4) uncertainties from different published slip models, and finally a model without consideration of uncertainty. The goal of this exercise is to perform a sensitivity analysis, and not to fit the best possible model to the data: therefore, I set the rate-and-state parameters to some reasonable, but not optimized values ($A\sigma = 6$ kPa, $t_a = 10000$ d for Parkfield; and $A\sigma = 28$ kPa, $t_a = 8000$ d for Tohoku). I run 100 iterations of the model, altering each of the sources of variability in turn. In models which do not consider receiver fault uncertainty, I use the average mainshock focal mechanism; in models which do not consider slip model uncertainty, I use the original slip model without addition of

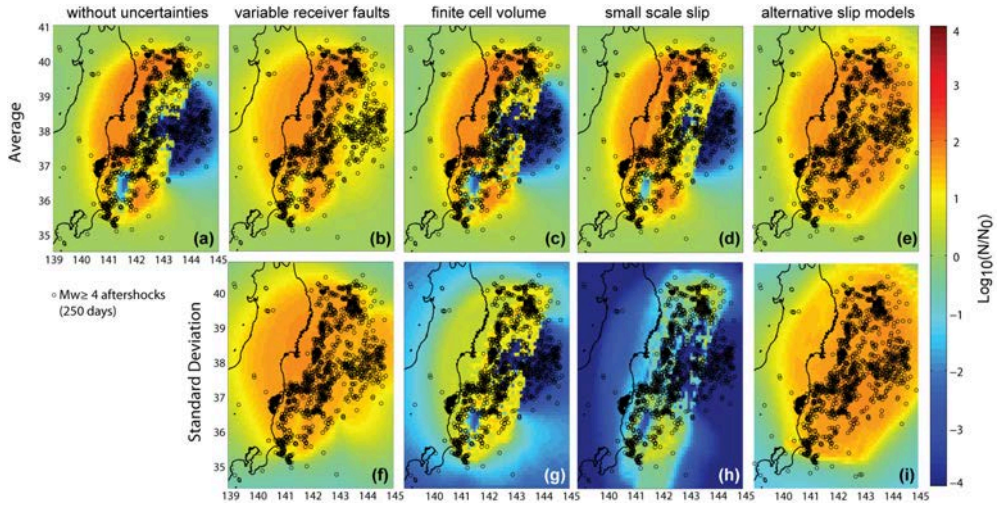

Figure 3.8: *Maps of forecasted seismicity for Tohoku. The colour scale indicates the number of events forecasted between 5 and 250 days (N), divided by the background number of events (N_0), on a logarithmic scale. (a): uncertainties not included; (b)-(e): mean forecast obtained including uncertainties from: receiver fault orientation (b); finite cell volume (c); small scale slip in the slip model (d); different published slip models (e). (f)-(i): Standard deviation corresponding to the figures above, calculated at each grid point from the set of Monte Carlo iterations.*

short wavelength slip.

Fig. 3.7 shows the effect of uncertainties on the forecasted temporal evolution of seismicity. In Fig. 3.7a and 3.7e, each line corresponds to the choice of a different receiver focal plane; it is clear, for both case studies, that this choice has a more profound effect on the forecast than the other sources of uncertainty. I find that considering the finite volume of cells has very limited impact on the temporal evolution of seismicity for Tohoku, and a moderate effect for Parkfield (Fig. 3.7b, 3.7f); the effect of small scale slip is also very small (Fig. 3.7c, 3.7g), and negligible compared to the impact of using different published slip models (Fig. 3.7d, 3.7h).

I find that the spatial distribution is also affected most significantly by the choice of receiver fault (Fig. 3.8, 3.9 and 3.10). In particular, in the average map, the seismicity lows in the area of coseismic slip disappear for both mainshocks (Fig. 3.8b and 3.10b).

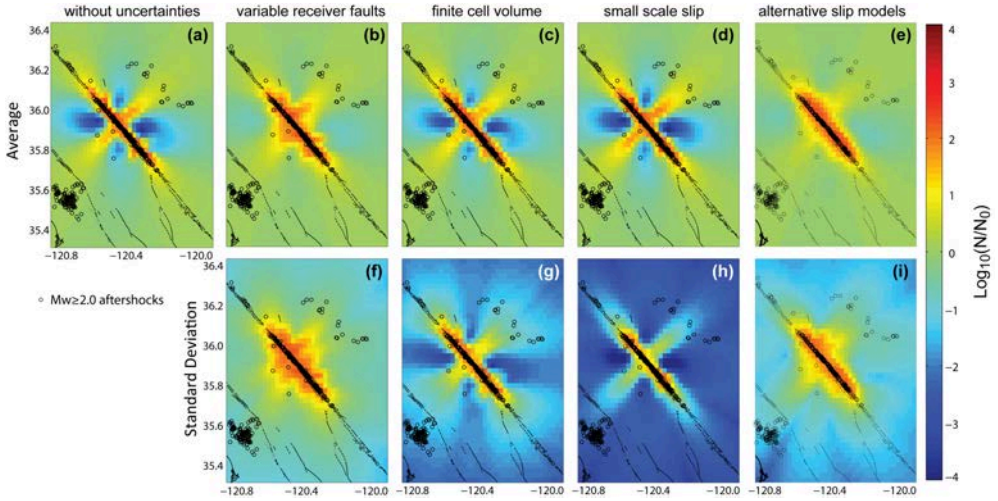

Figure 3.9: *Maps of forecasted seismicity for Parkfield. Individual maps correspond to those in Fig. 3.8.*

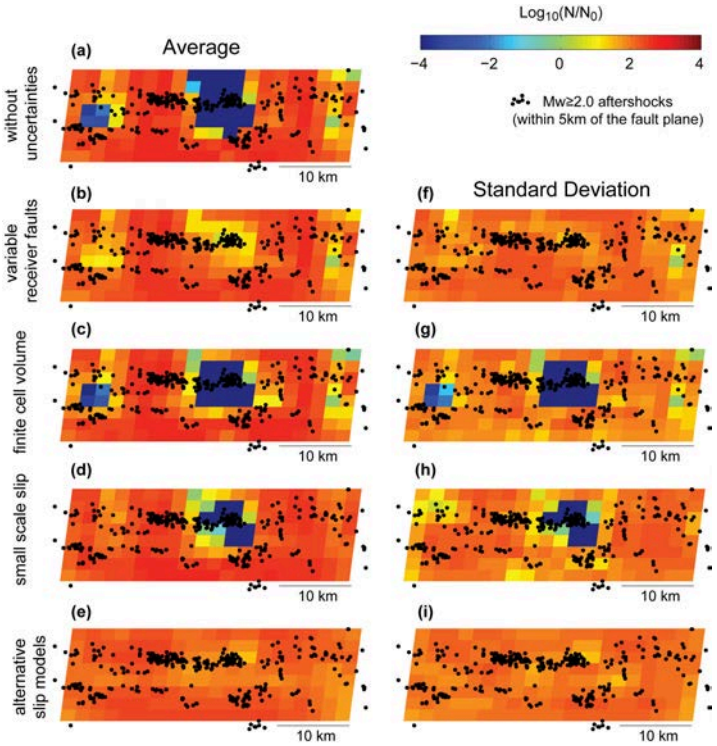

Figure 3.10: *Forecasted seismicity for Parkfield, projected on the mainshock fault plane; patches correspond to those in the slip model. Individual plots correspond to those in Fig. 3.8.*

The variation of the forecast across iterations is not only large in the vicinity of the fault, but also in the far field. For Tohoku, in the offshore region at lat ~ 38°, lon ~ 144° presents a large standard deviation (Fig. 3.8f), in an area which is quiescent when uncertainties are not included (Fig. 3.8a). This indicates that faults exist with orientations on which seismicity is promoted, as confirmed by the observed aftershocks in these areas.
When considering the finite cell size, a smoother forecast is obtained (Fig. 3.8c and 3.10c); moreover, the on-fault area of reduced seismicity has a smaller size compared to the case in which uncertainties are negligible. This results indicate that sharp boundaries between areas of increased and decreased seismicity is an artefact due to coarse grid size with respect to the near field gradients, and that the area of stress shadows can be overestimated due to discrete sampling of the stress field.
Comparison of spatial forecasts obtained with and without slip model uncertainty (Fig. 3.8d, 3.8a; 3.9d, 3.9a) indicates that the impact of small scale slip is very small. For both mainshocks, a low levels of seismicity (stress shadow) are still observed on the mainshock fault; the standard deviation is also small in this area, indicating that this feature is consistent across most of the Monte Carlo iterations obtained from different perturbed slip models. This result indicates that slip heterogeneity, as simulated in the model, is not sufficient to induce seismicity close to the largest patch of coseismic slip on fixed receiver faults. On the other hand, the differences between published slip models are significant: I find that the standard deviation in the expected number of events across models obtained from different published slip distributions is similar to the absolute value of their average (Fig. 3.8e, 3.8i; 3.10e, 3.10i).
The two mainshocks significantly differ in terms of size and complexity; however, I find that the same sources of uncertainties among those analysed in this work are most significant in both cases. I see a particularly large variability due to receiver fault orientation for the Tohoku sequence, with the total number of events varying by a factor of ~ 4.5; this result reflects the higher structural complexity of a subduction zone, in which a wider range of receiver fault orientations is present. The differences due to the choice of slip model are also larger for Tohoku, but this result may simply be due to the larger number of slip models compared. The effect of finite cell volume depends on the grid resolution compared to the scale of the stress field: this aspect is slightly more important for Parkfield (Fig. 3.7b, 3.7f), due to the fact that the grid used for Tohoku produced a smoother forecast than the one used for Parkfield (Fig. 3.8, 3.9).

3.4 Model sensitivity to parameters $A\sigma$, t_a and μ.

I fitted rate-and-state parameters $A\sigma$, t_a to the data by maximizing the log-likelihood, and therefore did not consider them as a source of error; however, in a forecasting setting the values of these parameters are not constrained a priori. A detailed discussion of the sensitivity of CRS models to the background rate, and the rate-and-state parameters $A\sigma$ and t_a can be found in *Cocco et al.* [2010]. In order to estimate the role of model parameters compared to the uncertainties discussed above, I estimate the spread of the forecast for the Tohoku sequence, due to three parameters: $A\sigma$, t_a and the friction coefficient μ.
Typical values of the frictional resistance parameter $A\sigma$ are between $10-100$ kPa [*Hainzl et al.*, 2010b]. The parameter t_a, the aftershock duration time, is typically of the order of tens of years; here I used values between $5000-20000$ days ($13.7-54.8$ years). Fig. 3.11a-b shows that variations of $A\sigma$ and t_a within these ranges lead to significant differences in forecasted number of events, comparable to the variation due to the different published slip models or to the variability from receiver fault uncertainty (Fig. 3.7). These values give a measure of the variability of the forecasts when $A\sigma$ and t_a are completely unknown; on the other hand, these values can be better constrained during the aftershock sequence. Considering a narrower range of $A\sigma$ between $80-100$ kPa and t_a between $8000-13000$ days, the sensitivity of the model to the parameters has a smaller impact than the receiver fault and the differences between published slip models. In the spatial domain, I find that the variability due to these parameters is modest compared to the effect of the variable receiver fault and to the choice of slip model (comparison between Fig. 3.11c-d and Fig. 3.8); this can be expected since these parameters only affect the seismic productivity at each grid point, but they do not modify the spatial features of the stress field.
I also tested the effect of the coefficient of friction μ. Fig. 3.12 shows that, for μ between 0.1 and 0.7, the impact of this parameter on the model is comparable to the variation due to small scale slip or to finite grid resolution, but modest compared to the most significant sources of uncertainty (Fig. 3.7, 3.8).

3.5 Combining Models

Having analysed the distribution of forecasts arising from different factors in the input data, the following question arises: how to combine the forecasts from each Monte Carlo iteration into a single forecast? To handle variability in the input data correctly, it is important to

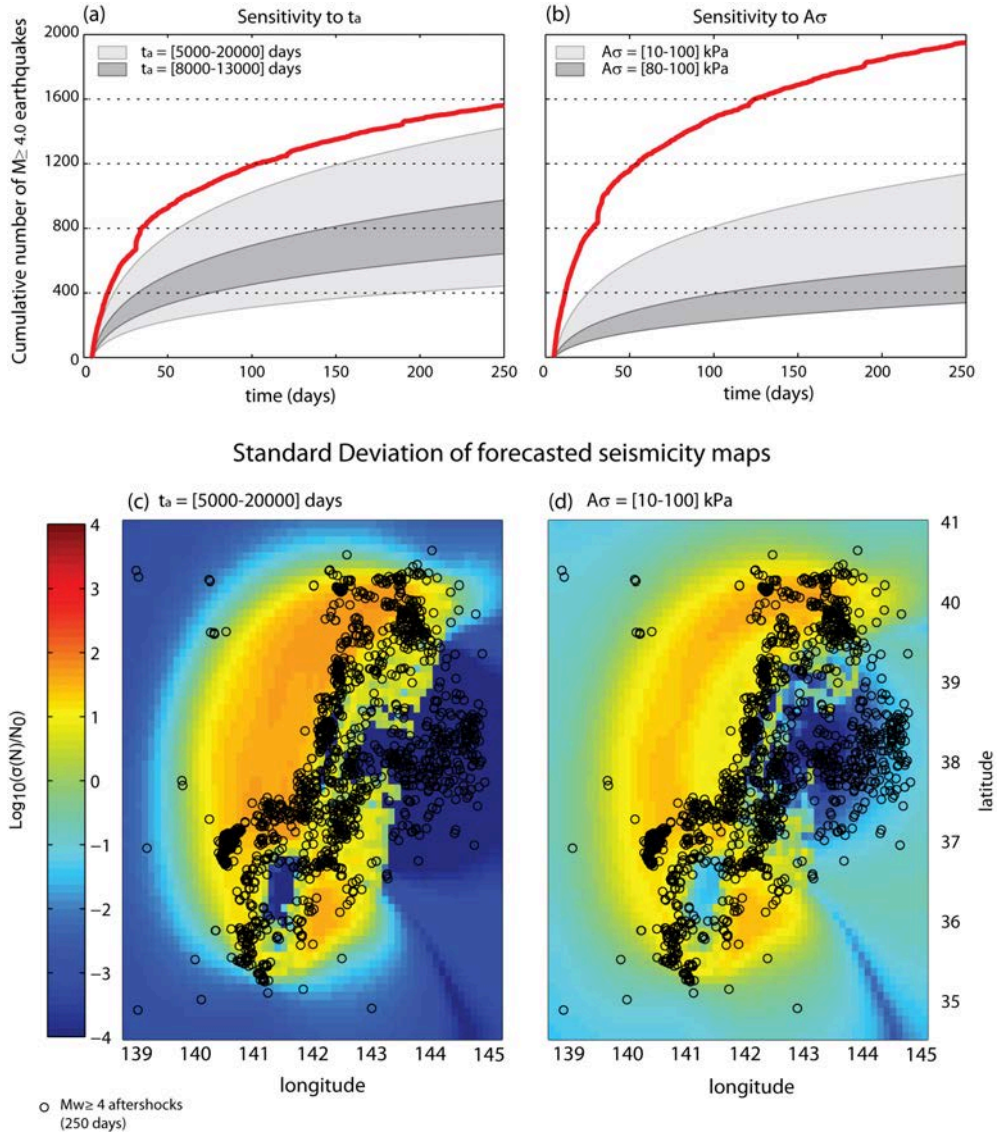

Figure 3.11: *Sensitivity of the forecast to rate-and-state parameters $A\sigma$ and t_a, for the Tohoku sequence. (a) Temporal evolution of seismicity for typical values of t_a, with fixed $A\sigma = 28$ kPa. (b) Temporal evolution with variable $A\sigma$, and fixed $t_a = 8000$ d. the red line is the observed cumulative number of events. (c-d) Standard deviation of forecasted number of events ($\sigma(N)$), divided by the background seismicity, on a log scale. t_a and $A\sigma$ are in the same range as in panels (a), (b); t_a was varied in intervals of 500 d, $A\sigma$ in intervals of 10 kPa. In all cases, stresses were resolved on a fixed plane given by the average mainshock focal plane; other sources of uncertainty were not included.*

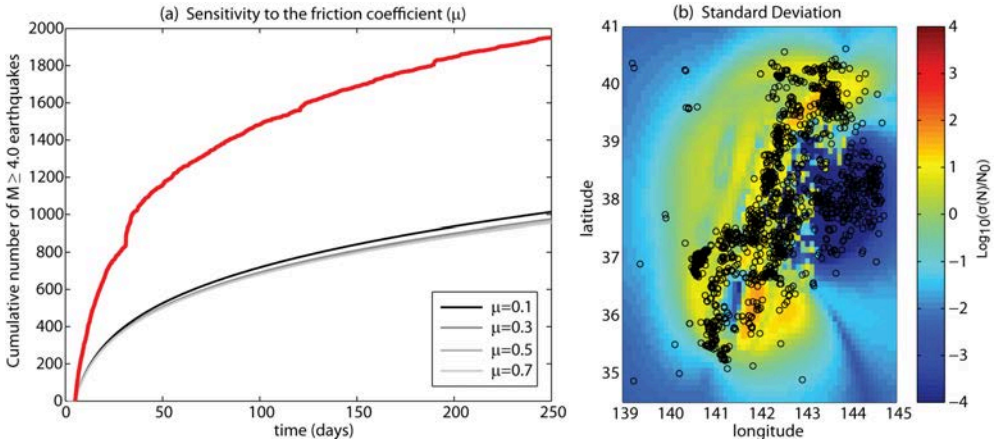

Figure 3.12: *Sensitivity of the forecast to the coefficient of friction* μ*, for the Tohoku sequence. (a) Temporal evolution of seismicity with* μ *between* 0.1 *and* 0.7*. The red lines is the observed seismicity. (b) Standard deviation of forecasted number of events* ($\sigma(N)$)*, divided by the background seismicity, on a log scale.*

draw a distinction between the physical interpretation of different types of uncertainties. With sub-grid variability, I refer to the spatial heterogeneity of physical properties in a crustal volume: for example, the presence of faults with different orientations or inhomogeneous elastic properties. These spatial variations, which can be interpreted as aleatoric uncertainties, cause a real variability in Coulomb stress values, which gives rise to physically observable characteristics of seismic sequences: an example of such phenomena is the observation of increased seismicity rates in areas with negative average ΔCFS. In this context, each Monte Carlo iteration can be viewed as representative of a small cell sub-volume, the exact location of which can not be resolved. With these assumptions, the resulting forecast should not be considered as the average of the several possible and alternative forecasts, but instead as a simulation of the behaviour emerging from real heterogeneity within each grid cell. I consider the sampling of a set of existing receiver faults, as well as the consideration of heterogeneity due to finite cell volume, as ways to reproduce this physical heterogeneity.

The use of a set of possible slip models is an example of epistemic uncertainties, and it requires a different interpretation: the forecasts obtained in this case are alternative to each others, and their average does not have a clear physical meaning. The distribution of such forecasts, on the other hand, can be used to estimate the sensitivity of the model to the input slip model, and therefore to provide

an estimation of the final uncertainty of the forecast. Additionally, ensemble models can be constructed by combining models based on alternative assumptions or input data; and while such procedure may not have an obvious physical interpretation, recent studies [*Marzocchi et al.*, 2012] have proven it to be a valuable tool from the point of view of operational earthquake forecasting. In their study, the authors use Bayesian averaging to combine models from the five-year Regional Earthquake Likelihood Models (RELM) for California: these are statistical models submitted by different authors, and based on different modelling strategies. Here I test whether the same approach can also be effective to combine forecasts from alternative input data within a single model class.

I follow the approach of *Marzocchi et al.* [2012] in creating an ensemble model based on a weighted average of forecasts from all available slip models. I weight models using the Score Model Averaging method [*Marzocchi et al.*, 2012]:

$$R_{ens} = \sum_{j}^{J} w_j R_j \tag{3.2}$$

with weights given by

$$w_j = \frac{\delta_j^{corr} S_j}{\sum_k^j \left[\delta_k^{corr} S_k\right]} \tag{3.3}$$

where δ_j^{corr} is a factor accounting for the correlation between models, and S_j is given by[1]: $S_j = |LL - LL^*|$, where LL is the model log-likelihood, and LL^* is the log-likelihood of a reference model, in this case a uniform Poisson model with seismicity rate given by the background rate. For more detail about the method, see *Marzocchi et al.* [2012]. Due to the logarithmic scaling with Likelihood, this weighting scheme tends not to favour the best performing model as strongly as other schemes. In light of the fact that small scale slip variability plays a secondary role compared to the differences between published slip models, I do not include this aspect, for computational efficiency: the individual models in the ensemble are all obtained from the original slip model, without addition of small scale slip.

1 This formula differs from the one given in *Cattania et al.* [2014] ($S_j = 1/|LL - LL^*|$). The version given here is the correct one. An erratum has been submitted to rectify the article.

Tohoku

Model	$A\sigma$ (kPa)	t_a (d)	I	N ($N_{obs} = 2266$)
Without uncertainties	100	19500	0	547
With uncertainties	18	18000	5.65	2547

Parkfield

Model	$A\sigma$ (kPa)	t_a (d)	I	N ($N_{obs} = 674$)
Without uncertainties	8	10000	0	254
With uncertainties	4	10000	14.43	526

Table 3.2: *Comparison of rate and state parameters and model performance, based on the slip models with index* 1 *in Table 3.1. The last column is the total number of forecasted aftershocks, and* N_{obs} *is the observed number.*

3.6 Model Performance

I quantify the performance of various models: first, I assess the effect of including aleatoric uncertainties (due to finite cell size and variable receiver fault orientations); secondly, I present a comparison of the performance of models obtained from the slip models listed in Table 3.1; finally, I study an ensemble model obtained combining the forecasts from alternative slip models.
In all cases, model performance is quantified by the average information gain (Eq. 2.8).

3.6.1 Performance of models including stress heterogeneity

I compare the log-likelihood of a model which includes stress variability to a simple model which assumes optimally oriented planes, and does not account for finite volume of the cells; both models use the same slip distribution ([*Wang et al.*, 2012b, 2013]), without the addition of synthetic slip. I invert for rate-and-state parameters using the entire period of the forecast (250 days for Parkfield, $5 - 250$ days for Tohoku). As previously observed by *Hainzl et al.* [2009], I find that overall model performance improved significantly when I account for the heterogeneity of the stress field (Table 3.2): the change in log-likelihood per event is 5.65 for Tohoku and 14.43 for Parkfield. I find that models which consider

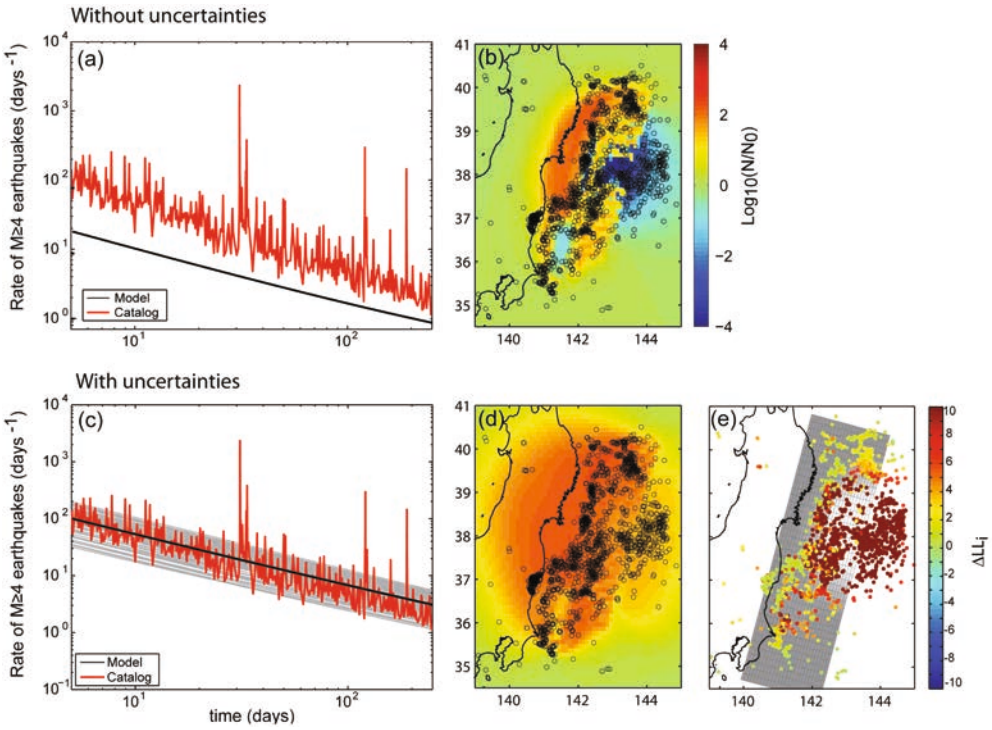

Figure 3.13: *Comparison of the modeled seismicity with (c,d) and without (a,b) aleatoric uncertainty, for Tohoku. (a) and (c): temporal decay of seismicity; red line: observed decay; black line: modeled seismicity; grey lines: individual Monte Carlo iterations. (b) and (d): spatial distribution of modeled number of events divided by background number of events in 250 days, on a logarithmic scale. (e): map of individual aftershocks, colour coded by* $\Delta LL_i = \log(R_1(x_i, t_i)) - \log(R_0(x_i, t_i))$ *when aleatoric uncertainties are included: the large majority of events is better modeled by including uncertainties. In the background, in black and white: the slip model (saturated at slip=20 m).*

aleatoric uncertainty provide a better description of both the spatial and temporal distribution of seismicity (Fig. 3.13, 3.14). Moreover, these models better estimate the total number of events for both sequences (Table 3.2; Fig. 3.13, 3.14).

3.6.2 Performance of published slip models

I evaluate the ability of published slip models to reproduce the observed seismicity. I perform two types of tests: (1) Non-prospective mode: I allow the model to find the best set of parameters to fit the data in the entire modeled period: the inversion of model parameters is done by maximizing the log-likelihood for the test period (250 days for Parkfield,

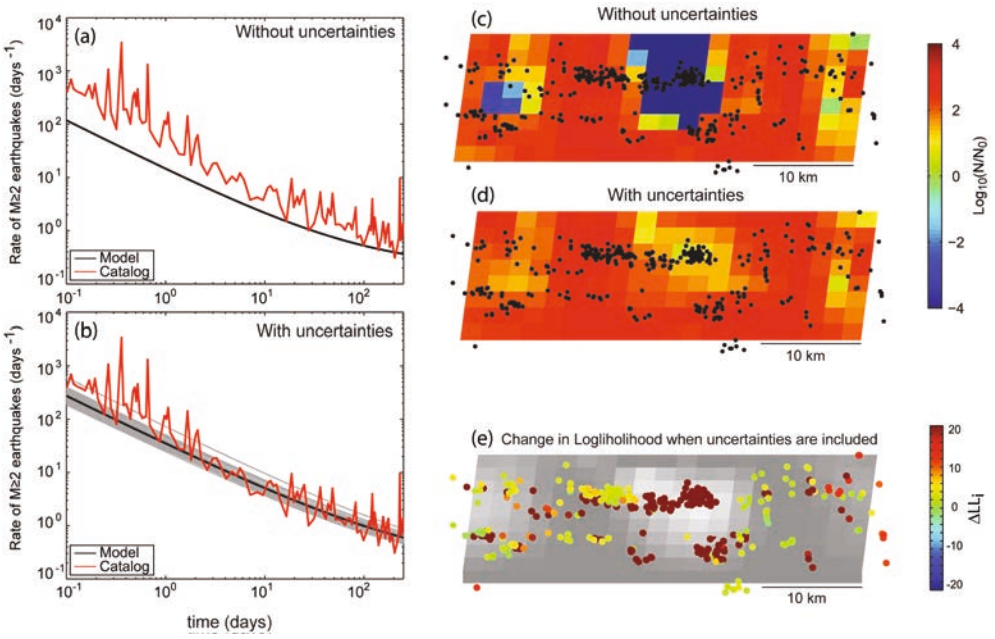

Figure 3.14: *Comparison of the modeled seismicity with (b,d) and without (a,c) aleatoric uncertainty, for Parkfield. Lines and colours scales correspond to those in Fig. 3.13. Also in this case, most of the events are better modeled when aleatoric uncertainties are included (plot e); comparison with the underlying slip model (saturated at slip=0.3 m) shows that, in particular, the events occurring on the rupture area are better explained by including stress heterogeneity.*

5 – 250 days for Tohoku). (2) Pseudo-prospective mode: I use the first 5 days of complete catalogue to fit rate-and-state parameters, and model the seismicity for the remaining time. The goal of the first tests is to compare the performance across slip models in the ideal case in which the best parameters are known; the second test, on the other hand, reproduces the condition of a forecast scenario. For each model, I include aleatoric uncertainties from receiver fault and grid size, and use the average value.

Model performance results are summarized in Fig. 3.15. I do not find a clear correlation between slip model complexity (as indicated by number of fault segments or number of patches) and model performance (Fig. 3.16). I find that for Tohoku, both in the non-prospective and the pseudo-prospective case, the ensemble model has a higher log-likelihood than any of the models in the sample. For Parkfield, I find that the ensemble model outperforms all the individual models in the pseudo prospective test; only one model outperforms the ensemble model in the non-prospective test.

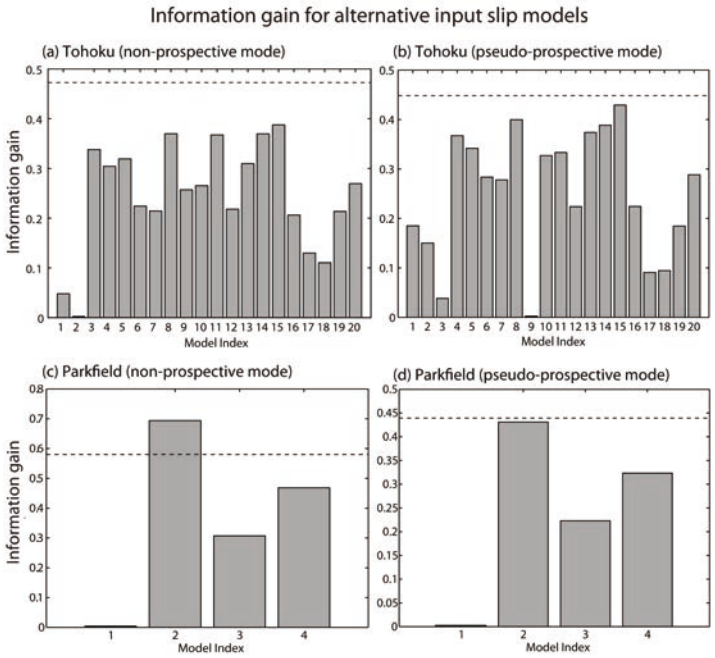

Figure 3.15: *(a-b) Comparison of Information Gain (*I*) for Tohoku, in non-prospective mode (a) and pseudo-prospective mode (b). (c-d) Comparison of* I *for Parkfield: (c) non-prospective mode and (d) pseudo-prospective mode. Each histogram corresponds to a slip model, in the order in which they are listed in table 3.1. Probability gains are calculated with respect to the worst model. The dotted line indicates the performance of the ensemble model.*

3.7 Discussion

The sensitivity analysis shows that various uncertainties in Coulomb stress have a profound impact on CRS models; in particular, the orientation of receiver faults and the choice of input slip model have a predominant effect.

The heterogeneity of stress field due to the presence of multiple receiver fault orientation plays a first order role in both spatial distribution and temporal evolution of the forecast. This is not surprising considering that resolving the stress tensor on different planes can give rise to very different stress fields, both in the near and in the far field (see Fig. 3.17); on the other hand, the perturbations in the stress fields due to finite cell size and by small scale slip act on a smaller scale, and are overall less significant.

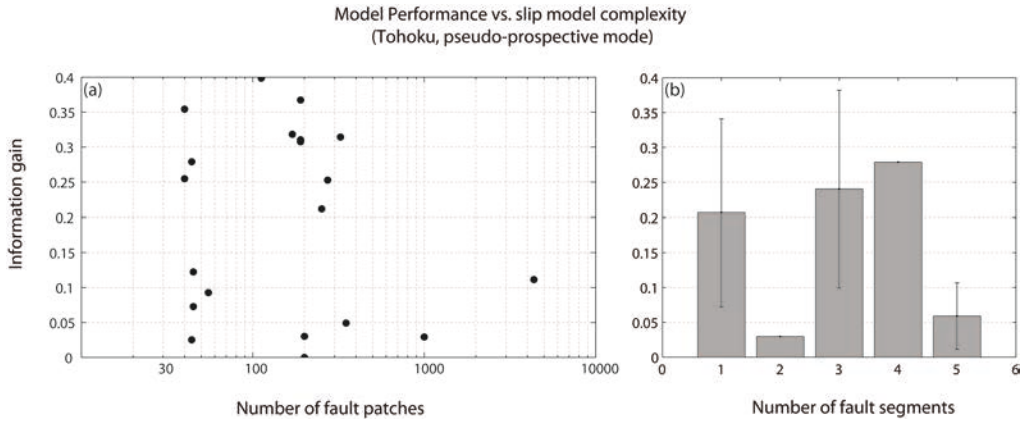

Figure 3.16: *Relationship between slip model complexity and forecast performance. (a) Probability gain per event as function of the total number of slip model patches. (b) Probability gain per event for models with different number of fault segments. Each histogram represents the average between models with a given number of fault segments, and the black bar indicate one standard deviation within each group. No clear trend is visible between the complexity of slip models and their performance.*

3.7.1 Suppression of stress shadows

I find that some important features of the forecast, such as the existence of stress shadows, are altered if I consider seismicity as emerging from the contribution of faults at different orientations which respond independently to the stress field. As previously suggested by various authors [*Marsan*, 2006; *Helmstetter and Shaw*, 2006], variability of the stress field in the context of rate-and-state models can provide an explanation for the observation of seismicity in regions of average negative stress change. This behaviour emerges from the rate-and-state response being highly non linear with respect to ΔCFS at short time scales. *Dieterich* [1994] (Eq. 12) gives the rate of seismicity following stress step $\Delta\tau$:

$$R(t) = \frac{r_0\dot{\tau}}{\dot{\tau}_r}\left\{\left[(\dot{\tau}/\dot{\tau}_r)\exp\left(\frac{-\Delta\tau}{A\sigma}\right)-1\right]\exp(\frac{-t}{t_a})+1\right\}^{-1} \tag{3.4}$$

Integration with respect to time yields the cumulative number of earthquakes at time t:

$$N(t) \approx \frac{r_0\dot{\tau}}{\dot{\tau}_r}\left\{t + t_a\left[\ln\left(\alpha\exp(-t/t_a)+1\right)-\ln(\alpha+1)\right]\right\} \tag{3.5}$$

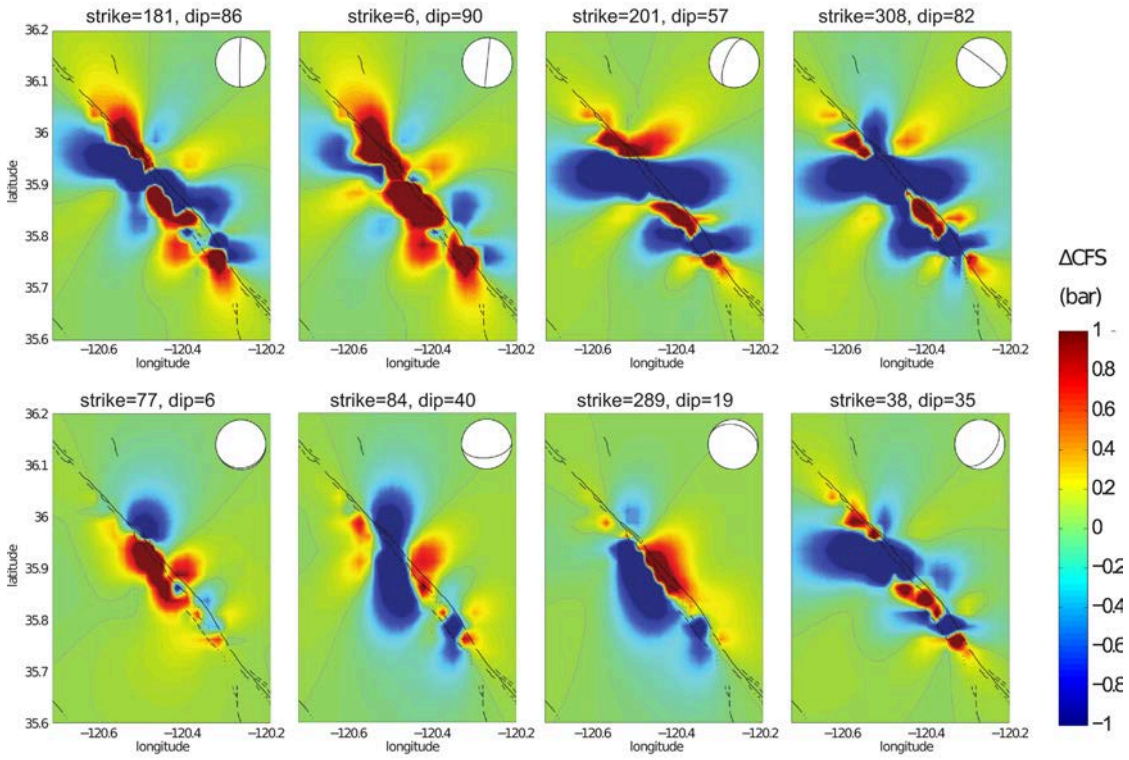

Figure 3.17: *Examples of ΔCFS fields after the Parkfield earthquake, resolved on a selection of receiver fault orientations from the catalogue of past focal mechanisms. The large variability in stress fields explains why this source of uncertainty dominates the spread of forecasted seismicity.*

with $\alpha = \dot{\tau}/\dot{\tau_r} \exp(-\Delta\tau/A\sigma) - 1$.

For $t \ll t_a$, expanding to first order in t, we have

$$\begin{aligned} N(t) = & \frac{r_0\dot{\tau}}{\dot{\tau_r}}\left[t + t_a \ln\left(\frac{\alpha + 1 - \alpha t/t_a}{\alpha+1}\right)\right] = \\ & \frac{r_0\dot{\tau}}{\dot{\tau_r}}\left[t + t_a \ln\left(1 - \frac{\alpha t}{(\alpha+1)t_a}\right)\right] \approx \\ & \frac{r_0\dot{\tau}}{\dot{\tau_r}}\left[t - t_a \frac{\alpha t}{(\alpha+1)t_a}\right] = \frac{r_0\dot{\tau}}{\dot{\tau_r}}\left[t\frac{1}{\alpha+1}\right] = \\ & \frac{r_0\dot{\tau}}{\dot{\tau_r}}\left[t\frac{\dot{\tau_r}}{\dot{\tau}}\exp(\Delta\tau/A\sigma)\right] = r_0 t \exp(\Delta\tau/A\sigma) \end{aligned} \tag{3.6}$$

Therefore, the number of events at short times compared to t_a depends exponentially on the stress change $\Delta\tau$. If the stress field is spatially heterogeneous, or if an ensemble model is constructed from a set of models with perturbed stress fields, the largest value of the distribution

will dominate in the short time.
On the other hand, after a time much longer than the aftershock duration time ($t \gg t_a$), we have

$$\begin{aligned} N(t) = &\frac{r_0\dot{\tau}}{\dot{\tau_r}}\left\{t + t_a\left[\ln(1) - \ln(\alpha+1)\right]\right\} = \\ &\frac{r_0\dot{\tau}}{\dot{\tau_r}}\left\{t + t_a\left[-\ln\left(\frac{\dot{\tau}}{\dot{\tau_r}}\exp(-\Delta\tau/A\sigma\right)\right]\right\} \end{aligned} \tag{3.7}$$

which, if the tectonic loading rate doesn't change after the mainshock ($\dot{\tau} = \dot{\tau_r}$) becomes

$$N(t) = r_0\left[t + t_a\Delta\tau/A\sigma\right] = r_0 t\left[1 + \frac{\Delta\tau}{\dot{\tau_r}t}\right] \tag{3.8}$$

And the number of excess events is $rt(\Delta\tau/\dot{\tau_r}t)$. Therefore, the ratio of excess and background events is the ratio between the stress change $\Delta\tau$ and $\dot{\tau_r}t$, the total tectonic stress accumulated in time t. Due to the linearity between N and $\Delta\tau$, the total number of events at each grid point after $t \gg t_a$ depends only on the mean value of the distribution from which perturbed values are drawn. Since in the time scale considered in this study $t \ll t_a$, stress shadows are reduced by introducing uncertainties, since the system is in the regime in which the largest ΔCFS of the distribution dominates (Eq. 3.6).

The results presented here indicate that the complexity of fault systems, with faults of different orientations co-existing in a crustal volume, can generate enough stress heterogeneity to explain the observation of seismicity in stress shadows, and they are in agreement with the results from *Toda et al.* [2011] and *Enescu et al.* [2012], who noticed that receiver fault variability plays an important role for the Tohoku aftershock sequence. The suppression of stress shadows also accounts for the better performance of the models in which aleatoric uncertainty is taken into account: in such models, seismicity does not shut down completely in the area of the coseismic rupture, or other areas of negative average stress change, and earthquakes observed at these locations is better explained. Due to definition of log-likelihood (which becomes singular if an event is observed in an area where the seismicity rate is predicted to be exactly 0), this reduction of stress shadows has a dramatic effect on the results of log-likelihood based tests.

3.7.2 Other aspects of model behaviour due to aleatoric uncertainties

Models which do not include aleatoric uncertainty are found to underestimate the total number of events by a factor of $3-4$, while better estimations are obtained when stress variability is taken into account. This difference can be understood from the values of $A\sigma$, the frictional resistance parameter which determines how strongly seismicity is enhanced by positive ΔCFS, or inhibited by negative ΔCFS. The parameter search yields higher values of $A\sigma$ for models which do not include uncertainties (Table 3.2). This result is due to the presence of stress shadows: since the log-likelihood heavily penalizes models with areas of almost complete seismicity shutdown, high values of $A\sigma$ will be favoured, so that stress shadows are less effective at inhibiting seismicity. At the same time, higher values of $A\sigma$ cause positive stress changes to produce fewer earthquakes, leading to the underestimation of total the number of aftershocks.

These findings have important implications for physics-based operational forecasting models. The most common choices of receiver fault orientation (the use of a fixed receiver or of Optimally Oriented Planes) vastly underestimate the variability of Coulomb stress, and the sensitivity study shows that these assumptions have a dramatic effect in forecasted distribution of seismicity. Another approach consists of including information about the local geology by use of a gridded fault model [*Steacy et al.*, 2005; *Segou et al.*, 2013; *Toda et al.*, 2011]; however, this method also assumes a single fault orientation at each grid point, and therefore neglects the aleatoric uncertainty associated with receiver faults. The performance comparison indicates that considering this aspect leads to significantly higher log-likelihood scores.

Woessner et al. [2011] compared the performance of statistical and physical models for the 1992 Landers sequence, and they also found that physics-based models perform significantly better when they include a stochastic component; however, they observed that CRS models including uncertainties exhibited an excessive increase in seismicity in areas of large, negative stress changes. This behaviour is due to the assumption that the standard deviation of ΔCFS at each grid point is directly proportional to its absolute value [*Hainzl et al.*, 2009]: since the distribution of ΔCFS values is wide in areas of large and negative stress, large and positive values are likely to be sampled in the Monte Carlo iterations, and they dominate early seismicity (Eq. 3.6). On the other hand, stress variability is most likely underestimated in regions where the average stress field is close to 0. The models presented here do not make a priori assumptions on the distribution of ΔCFS: this approach is physically more consistent and it does not lead to increased seismicity in stress

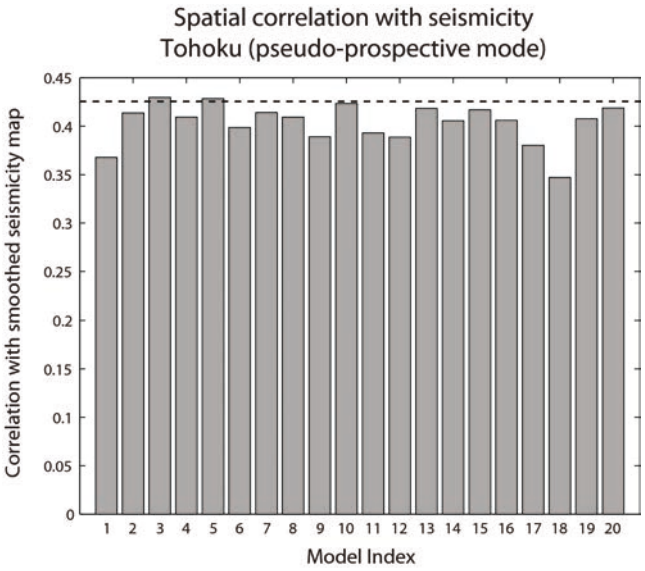

Figure 3.18: *Comparison of the correlation between forecasts and maps of observed seismicity, for different slip models, for Tohoku (pseudo-prospective mode).*

shadows (Fig. 3.9).

3.7.3 Epistemic uncertainties and ensemble models

In CRS models, a distinction between the treatment of aleatoric and epistemic uncertainties has not previously been made. While the methods used in the two cases are similar (averaging in the first case, weighted averaging in the second), the difference should be kept in mind. When dealing with aleatoric uncertainties the focus should be on realistically reproducing the physical stress variability; on the other hand, the combination of models with epistemic uncertainties is guided by an attempt to obtain the best model performance, as done in the ensemble models.

I find that the model ensemble generally outperforms all individual models. In particular, the results of the pseudo-prospective experiment (Fig. 3.15) indicate that ensemble models are promising in the context of operational earthquake forecasting: without knowing a priori which model will perform best, the ensemble model allows to obtain a better performance than each model, including the best. The log-likelihood of a forecast can be very sensitive to the occurrence of events in areas with very low forecasted seismicity: this implies that the better performance of ensemble models may be due to fact that, by overlaying a set of

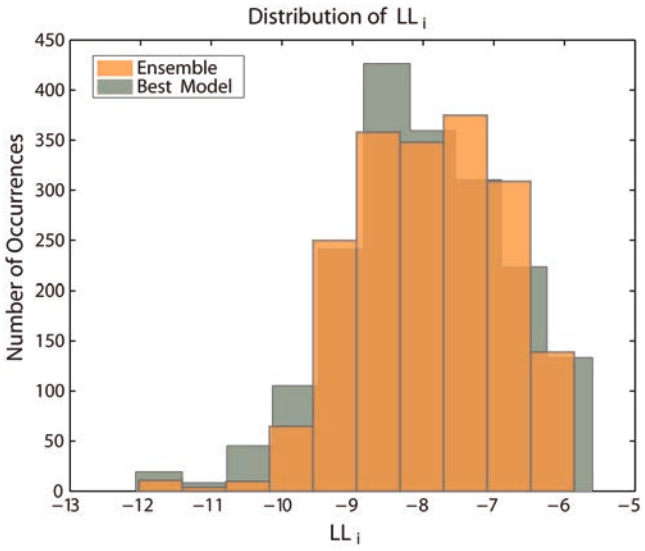

Figure 3.19: *Comparison of the contribution to the log-likelihood values of individual earthquakes* ($LL_j = \log R(\mathbf{x}_j, t_j)$) *for Tohoku, in non prospective mode: the similarity between the low tail of the two distributions indicates that improvement in log-likelihood is not due to few events with extremely low log-likelihood values.*

alternative forecast maps, areas of both high and low seismicity are reduced. In order to verify whether the improvement in log-likelihood is driven by a small number of events in areas of low forecasted rates, we calculate the correlation between the forecasted seismicity map and observed seismicity map, obtained by smoothing the catalogue over the forecast grid. Unlike the log-likelihood, this alternative measure of forecast success does not have a singularity for the case of events occurring in areas of zero seismicity rate. Fig. 3.18 shows that, for the non-prospective case, the ensemble model still outperforms most models; moreover, Fig. 3.19 indicates that the distribution of log-likelihoods for individual events is similar for the ensemble model and for the best model, confirming that the better performance of the ensemble model is not dominated by few events occurring in stress shadows.

3.7.4 Model limitations

In this chapter I attempted to address some of the limitations of CRS models, and to better describe the spatial complexity of the stress field; however, a number of simplifications still exist in the model. My approach to estimating fault orientation is arguably rather crude.

I performed some spatial selection for the Tohoku area, in order to account for different faulting style being predominant in each of the tectonic areas (wedge; fault interface; outer rise). However, I did not make an attempt to describe smaller scale spatial variations of fault structures, which could for example be achieved by weighting the focal planes from the catalogue by distance to each grid point, or by complementing the information from focal mechanisms with that from mapped faults [*Steacy et al.*, 2005; *Segou et al.*, 2013]. Focal planes in a volume of few kilometres (i.e. within a grid cell) are more homogeneous than on the entire scale of the domain [*Hardebeck*, 2006], and therefore the variability of ΔCFS may have been overestimated in this study.
I find that considering small scale variation of mainshock slip does not affect the distribution of the forecast significantly; in particular, the effect is much smaller than the variability due to the differences between published slip models. The effect of small scale slip variability may have been underestimated for two reasons:

- The grid size I used limits the definition of near field, and it may be too large to be affected by slip below a similar length. The model discretization was limited by computational resources; in Chapter 6 I present software improvements implemented in the meanwhile, which may in the future help overcoming this issue.

- The heterogeneity in fault geometry, or fault roughness, has not been included: the fault was always treated as a uniform plane. However, this aspect should also be taken into account: my treatment of slip heterogeneity could be extended to include fault roughness by creating synthetic slip models. The results indicate that the orientation of receiver planes plays a first order role, also in the vicinity of the fault: by symmetry, this suggests that including variability in the orientation of the rupturing faults may also enhance stress heterogeneity.

Another simplification of the model is the assumption that faults are uniformly distributed, while in reality they tend to cluster around major fault structures: the model could be improved by including the major existing faults on which seismicity concentrates. This could be achieved, within the rate-and-state framework, by estimating a spatially variable background rate, based on smoothed seismicity (see Chapter 2 and Chapter 5). However, such background rate calculation may suffer from large uncertainties due to limited sample size and the results of seismicity forecasts are very sensitive to those uncertainties [*Cocco et al.*, 2010].
Another simplification in the model is the choice of spatially uniform

rate-and-state parameters: while a simple 1D depth dependence could be introduced, the consideration of the full 3D spatially varying parameters would require a large number of parameters and lead to potentially unstable results. Finally, I point out that the model has intrinsic limitations due to the underlying physical assumptions. Various physical processes are neglected, including secondary triggering, afterslip, viscoelastic relaxation and redistribution of stresses by fluids: all these processes can modify the stress field postseismically, while I assume a stationary field after each earthquake. I verified that the improvement in model performance obtained by including aleatoric uncertainties is a robust feature, that persists when afterslip is also taken into account; a more detailed treatment of the role of time-dependent processes, which are particularly large following the Parkfield earthquake, is addressed in Chapter 4. The existence of afterslip should especially be kept in mind when evaluating the performance of different published slip models: since some of the earthquakes may be triggered by postseismic stresses, the ranking of the slip models in their ability to explain observed seismicity may not reflect how accurately they describe coseismic slip.

3.8 Conclusions concerning the treatment of uncertainties

In this chapter, I study the impact of different physical sources of uncertainties on CRS models of aftershock sequences, and I introduce a consistent framework to propagate epistemic and aleatoric uncertainties through such models.

I find that variability in ΔCFS gives rise to a large spread in the forecast, both in terms of spatial location and total number of events; in particular, receiver fault orientation plays a first order role. By incorporating the stress heterogeneity due to variable receiver faults, I obtain a significant performance improvement. These results indicate that a careful consideration of receiver fault orientation, combined with a stochastic treatment of its variability, are important aspects of CRS models and should be implemented in future applications.

I find that the choice of slip model is also an important source of uncertainty, and I explore the possibility of using ensemble averaging to combine models based on alternative slip distributions. This technique has previously been used to combine aftershock models based on entirely different principles [*Marzocchi et al.*, 2012]; here I suggest that the same methods can be used to address epistemic uncertainties within a

single model class. In agreement with [*Marzocchi et al.*, 2012], I find that also in this case ensemble models systematically outperform the individual models, and they are a promising tool in the context of operational earthquake forecasting.

4

AFTERSHOCK TRIGGERING BY POSTSEISMIC STRESSES

Controversy exists about the physical mechanism driving aftershock sequences, and in particular the relative role of coseismic static stress transfer and reloading by postseismic processes. In this chapter, I address the role of two postseismic processes: creep on the mainshock fault plane (afterslip), and secondary aftershock triggering by previous aftershocks. I find that modelling secondary triggering improves the maximum log-likelihood fit of the sequences. The effect of afterslip is more subtle, and difficult to assess for near-fault events, where model errors are largest. More robust conclusions can be drawn for off-fault aftershocks: following the Tohoku earthquake, afterslip promotes shallow crustal seismicity in the Fukushima region. Simple geometrical considerations indicate that afterslip-induced stress changes may have been significant on trench parallel crustal fault systems following several of the largest recorded subduction earthquakes. Moreover, the time dependence of afterslip strongly enhances its triggering potential: seismicity triggered by an instantaneous stress change decays more quickly than seismicity triggered by gradual loading, and as a result afterslip is particularly important between few weeks and few months after the mainshock.

The material presented in this chapter has been published in the following article:

- **Cattania, C.**, S. Hainzl, L. Wang, B. Enescu, and F. Roth, Aftershock triggering by postseismic stresses: a study based on Coulomb-Rate-and-State models, *J. Geophys Res.*, *in press*, doi: 10.1002/2014JB011500, 2015.

4.1 Introduction

The crust responds to a large earthquake with a variety of seismic and aseismic phenomena, including: aftershock sequences; aseismic slip

concentrated along the plate interface (afterslip); viscoelastic relaxation distributed in the asthenosphere [*Wang et al.*, 2012a]; and displacement of fluids giving rise to poroelastic rebound [*Nur and Booker*, 1972; *Cocco and Rice*, 2002]. These processes are induced by local changes in the stress field, and they in turn cause stress redistribution: physics-based models aimed at describing aftershock sequences should consider the interplay of these phenomena.

4.1.1 Afterslip

Afterslip is a widespread post-seismic process [*Marone et al.*, 1991], and it is considered the most significant source of surface displacement in the first few hundred days following the mainshock, while viscoelastic relaxation becomes increasingly significant at later times [*Wang et al.*, 2012a; *Diao et al.*, 2014]. Several authors have suggested that afterslip plays a central role in triggering aftershocks [*Benioff*, 1951; *Schaff et al.*, 1998; *Perfettini and Avouac*, 2004; *Savage et al.*, 2007; *Helmstetter and Shaw*, 2009; *Gualandi et al.*, 2014]: the total moment release of afterslip can be comparable to the coseismic moment [*Pritchard and Simons*, 2006], and it generates similar static stress changes as the mainshock. *Perfettini and Avouac* [2004] suggests that aseismic creep in the brittle-creep fault zone (downdip of the coseismic rupture) is responsible for triggering aftershocks; this model, which assumes a linear dependence between slip rate and aftershock rate, is in agreement with the mechanism suggested by [*Schaff et al.*, 1998] to explain the inter-event time of repeating earthquakes. On the other hand, the assumption of linearity between slip rate and seismicity rate has been questioned (for example, by *Hsu et al.* [2007]; *Savage* [2010]; *Helmstetter and Shaw* [2009]). In the rate-and-state formulation, a power-law decay arises from the nucleation time of a population of velocity weakening patches: the finite nucleation time introduces a delay following an instantaneous stress step, so that time-dependent stresses are no longer required to explain a delayed temporal evolution of seismicity.

4.1.2 Secondary Triggering

Another source of postseismic stresses are the aftershocks themselves. The seismic moment released by aftershocks is typically a small fraction of the coseismic moment (e.g. *Zakharova et al.* [2013]), and of the afterslip moment [*Perfettini and Avouac*, 2004]; for this reason, only the largest or the few largest events are normally considered in Coulomb studies. On the other hand, *Meier et al.* [2014] showed that about a third of the

aftershocks following the Landers mainshock experienced larger stress changes from aftershocks than from the mainshock. This finding is in agreement with *Marsan* [2005], who showed that given a fractal distribution of hypocentre locations and a Gutenberg-Richter distribution of magnitudes, small events can be as effective as large ones at generating stress perturbations.

All these lines of evidence indicate that both afterslip and secondary triggering play an important role in triggering aftershocks. On the other hand, a gap exists between these observations and physics-based models of aftershocks sequences developed in an operational forecasting context: with few exceptions (e.g. *Strader and Jackson* [2014]), these models do not usually include information about postseismic stresses [*Hainzl et al.*, 2010b]. In this study, I use CRS to quantify the role of afterslip and secondary triggering in generating aftershocks. I focus on the two case presented in Chapter 2: the 2004 Parkfield (M_w6.0) and the 2011 Tohoku (M_w9.0) earthquakes. I use the information gain (Chapter 2, Eq. 2.8) to verify whether the inclusion of postseismic processes improves the spatio-temporal fit to the observed aftershocks.
In this chapter, I present a comparison of CRS models, and I assess the general effect of postseismic stresses. In section 4.4, I discuss several factors controlling model behaviour. In particular, I assess the importance of the location and the temporal evolution of afterslip in triggering aftershocks, and I discuss the implications of these results in a global perspective. My goal is two-fold: on one hand, I aim to gain physical insight into the relative role of coseismic and postseismic stresses in triggering aftershocks; on the other hand, I test whether the inclusion of afterslip and aftershocks has the potential to improve operational earthquake forecasts aimed at modelling seismicity in the few hundred days following a large event.

4.2 Methods

I implements Coulomb-rate-and-state models as described in Chapter 2. Based on the results presented in Chapter 3, I know that the most important sources of uncertainties in Coulomb stress calculations are the choice of input slip model and the unknown orientation of the receiver faults on which the stress tensor should be resolved. I include the aleatoric uncertainties due to the latter by performing Monte Carlo simulations on a set of possible fault orientations (from the catalogue of past focal planes), and adding up the seismicity rates from each fault to

give an average rate, as described in Chapter 3.
The model domain for Parkfield corresponds to the area show in Fig. 2.3, and a depth range between [0.5, 11.5] km. For Tohoku, I considered the area shown in 2.4 and I create a non uniform grid such that grid points are not located too close to the edges of the slip models: I find this grid reduces the number of points for which ΔCFS exceeds the cut-off value described in Chapter 2.

4.2.1 Calculating time dependent stresses and rates

I consider static stresses generated by coseismic slip, afterslip, and aftershocks. All slip model based calculations are obtained from the analytical solutions for rectangular dislocations in an elastic half space [*Okada*, 1992].
A general, time dependent stressing history can be modeled by approximating it by a piece-wise linear function, and solving Eq. 2 and 3 for each time step using the analytical solution for linear stressing [*Dieterich*, 1994]. Since afterslip might be space and time dependent, each patch may experience a different temporal evolution. I developed a method based on spline interpolation, which allows to treat the general case of non-stationary afterslip, which is presented in Chapter 6. However, for the two test cases presented here, I find that the model behaviour is not changed significantly by approximating the afterslip as spatially stationary: for computational efficiency, I therefore assumed a spatially uniform temporal evolution $F(t)$. As shown by *Savage* [2010], the cumulative afterslip following Parkfield can be approximated by:

$$F(t) = A\log(1 + t/t_1) + B\log(1 + t/t_2) + C\log(1 + t/t_3) \tag{4.1}$$

with $A = 23.7$, $B = 9.02$, $C = 6.15$, $t_1 = 4.06$, $t_2 = 0.11$ and $t_3 = 10^{-4}$. For Tohoku, I found that the time series can be fit by a single logarithmic function: I obtained $A = 1; B = C = 0$ and $t_1 = 14.2$, in agreement with *Perfettini and Avouac* [2014].
To calculate the stresses imposed by an aftershock, I created a square synthetic slip model based on the focal mechanism solution and the empirical relations of *Wells and Coppermith* [1994]. For most aftershocks focal mechanisms are not available: in these cases, I followed the approach of *Chen et al.* [2013] and approximated the stress field by:

$$\Delta CFS = \frac{M_0}{6\pi r^3} \tag{4.2}$$

where M_0 is the seismic moment and r the distance to the earthquake hypocenter. I considered stress changes from all aftershocks above the magnitude of target events (described in Chapter 2) from $t = 0$.
Eq. 4.2 describes the decay of stress in the far field, but it gives unphysical values as $r \to 0$. In this study, the singularity is prevented by the use of a cut-off value for ΔCFS, described in Chapter 2.

4.3 Results

To verify whether modelling postseismic stresses has the potential to improve aftershock forecasts, I compare a starting model with only coseismic stresses (Model 0) with three models accounting additionally for postseismic effects: one including time-dependent stresses from afterslip (Model 1), one including secondary triggering by aftershocks (Model 2), and one including both processes (Model 3). Rate-and-state parameters $A\sigma$ and t_a are inverted independently for each model.

4.3.1 Model Performance

The performance of a model is again quantified by the Information Gain (Eq. 2.8) and by the log-likelihood change of individual events (Eq. 2.9). As shown in Table 4.1, secondary triggering by aftershocks causes in both cases the most significant changes in log-likelihood, with a probability gain of $I = 0.25$ for Parkfield and $I = 0.72$ for Tohoku; on the other hand, the inclusion of afterslip has an opposite effect on model performance for Parkfield and for Tohoku ($I = 0.10$ and $I = -0.41$ respectively). In the next section, I estimate the significance of these values by comparing them with the internal variability of each forecast due to the Monte Carlo sampling of receiver fault orientations. Information gain differences are significant for all models in the case of Tohoku; for Parkfield, I find that the improvement in performance due to afterslip is small between models 0 and 1, and not significant between models 2 and 3. The slip model of *Perfettini and Avouac* [2014] presents a similar coseismic slip distribution as other published slip models, but a different afterslip distribution: the authors find large shallow afterslip, overlapping with the area of coseismic slip. On the other hand, the patch of deep afterslip identified in previous models is still present. When using this slip models, the ranking of the models is unchanged; however, I find variations in the optimal values of RS parameters, as well as the information gain and the total number of forecasted events. I notice that the change in performance due to the choice of the coseismic slip

(a) Parkfield

Model	Afterslip	Secondary Triggering	$A\sigma$ (kPa)	t_a (days)	N_{events} ($N_{obs} = 644$)	I
0	no	no	4.0	8000	447	0
1	yes	no	8.0	5000	515	0.10
2	no	yes	3.5	7000	619	0.25
3	yes	yes	5.5	5000	853	0.22

(b) Tohoku (slip model from *Wang et al.* [2013])

Model	Afterslip	Secondary Triggering	$A\sigma$ (kPa)	t_a (days)	N_{events} ($N_{obs} = 1740$)	I
0	no	no	15.0	700 0	1139	0.0
1	yes	no	19.0	8000	1651	−0.41
2	no	yes	15.0	7000	1445	0.72
3	yes	yes	19.0	8000	1923	0.54

(c) Tohoku (slip model from *Perfettini and Avouac* [2014])

Model	Afterslip	Secondary Triggering	$A\sigma$ (kPa)	t_a (days)	N_{events} ($N_{obs} = 1740$)	I
0	no	no	40.0	16000	2179	0.0 (0.28∗)
1	yes	no	32.0	4000	2319	−0.08
2	no	yes	40.0	8000	2122	0.79
3	yes	yes	35.0	4000	2527	0.70

Table 4.1: *Rate and state parameters and model performance for Parkfield and Tohoku.* I *is the information gain, i.e. the difference in log-likelihood between each model and model 0 divided by the total number of aftershocks. Difference in RS parameters from Table 3.2 are due to slight differences in the calculation grids, described in the main text.*
∗Information gain between model 0 using the model from Perfettini and Avouac [2014] and model 0 using the model from Wang et al. [2013].

model ($I = 0.28$) is of the same order of the change due to the inclusion of afterslip, but smaller than the improvement achieved by modelling of secondary triggering.

4.3.2 Statistical significance of the information gains

Aleatoric uncertainties in the Coulomb stress field are included in the forecast by using a Monte Carlo method (Chapter 3): 100 iterations are performed to produce a set of forecasts $\{\lambda_1, \lambda_2, ..., \lambda_{100}\}$, and the final forecast $\overline{\lambda}$ is calculated from their average. I use a bootstrapping technique to estimate variations in the information gain of $\overline{\lambda}$ due to the randomness of this approach: by resampling the individual forecasts $\{\lambda_1, \lambda_2, ..., \lambda_{100}\}$ I obtain a set of alternative ensemble forecasts $\{\overline{\lambda}_1, \overline{\lambda}_2, ...\}$. This distribution can be interpreted as a sample of the possible forecasts due to variations in the spatial heterogeneity of the stress field.
Fig. 4.1 shows the distributions of information gains given in Table 1. For both earthquakes I see that improvement in information gain due to the inclusion of secondary triggering is significant compared to the effect of stress heterogeneity. The effect of afterslip is less important, especially for the Parkfield event (panels (a) and (b)); in particular, models 2 and 3 have virtually identical information gains. The decrease in information gain when including afterslip for Tohoku appears to be significant, and consistent across different slip models (panels (c) and (d)). The value or probability gain between model 0 and model 1 varies between panels (c) and (d), due to the fact that the two afterslip models present very different slip distributions.

4.3.3 Spatial distribution

For Parkfield I find that, by redistributing slip along the mainshock fault plane, afterslip modifies the location of the positive and negative lobes of the forecast, particularly to the south-west of the rupture plane (Fig. 4.2a-d). Secondary triggering, on the other hand, has almost no effect on the large scale spatial distribution of seismicity. The model based on coseismic stresses (Fig. 4.2e) predicts high seismicity in the surrounding of the rupture area, where stresses are highest; and low rates close to the area of maximum coseismic slip. The model which includes afterslip forecasts higher seismicity rates everywhere along the faults. The inclusion of aftershocks also leads to higher on-fault seismicity rates (also due to the lower value of $A\sigma$ for Model 2 than for Model 0), but does not change the spatial distribution significantly.
The first order features of the forecast map for the Tohoku sequence

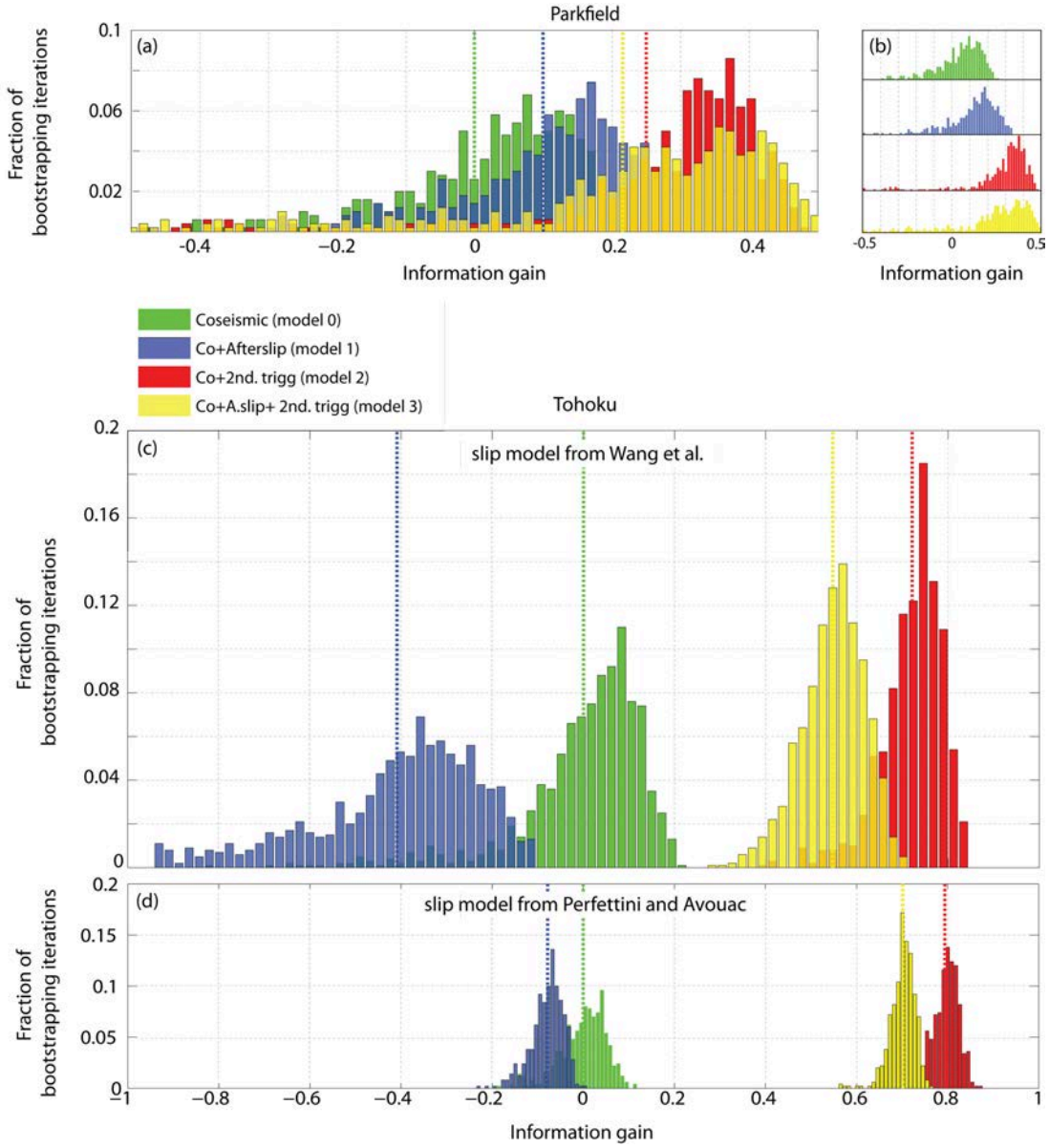

Figure 4.1: *Estimation of uncertainties in the information gains reported in Table 1. Each distribution is obtained from 500 bootstrap iterations. (a) Distribution of information gains for the Parkfield models; (b) same distributions as in (a), shown separately for clarity; the left tail of the distribution is not shown. (c) and (d) Information gains for Tohoku models, based on the slip models from Wang et al. [2013] and Perfettini and Avouac [2014] respectively.*

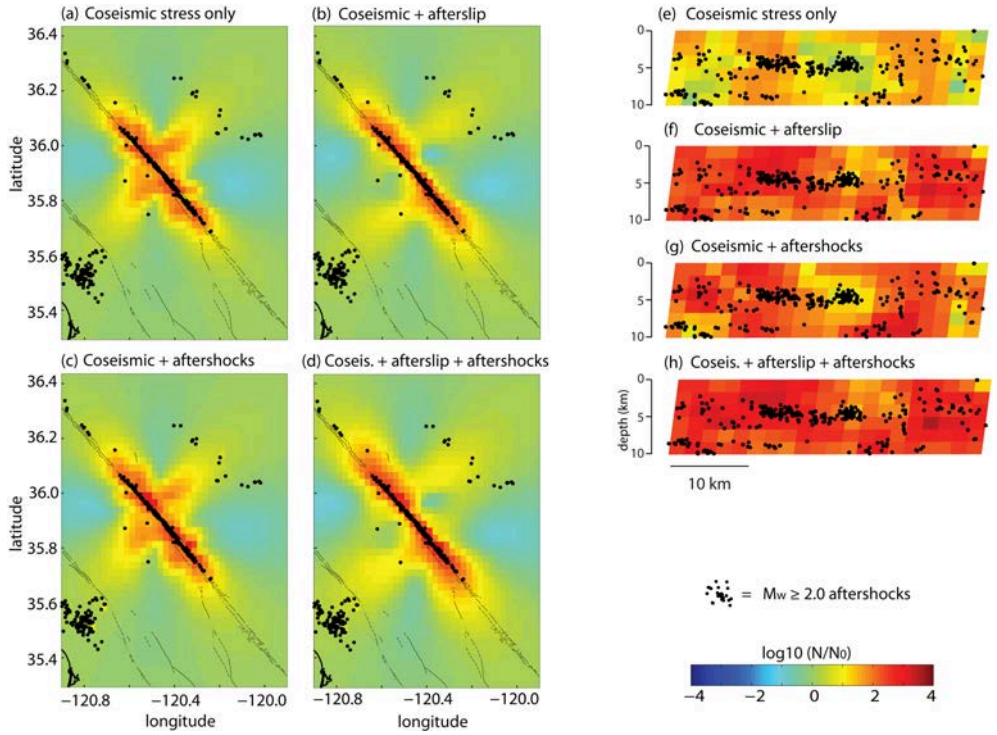

Figure 4.2: *Left: Maps of forecasted seismicity in 250 days following Parkfield, summed over all depth layers. Right: Forecasted seismicity on the mainshock rupture plane. The colour indicates the number of forecasted events, divided by the background number (N_0), on a logarithmic scale. Black dots are the observed events; in panels (e-h), only events within 5 km from the fault plane are shown. (a,e) model with coseismic stresses only; (b,f) model with coseismic stresses and afterslip; (c,g) model with coseismic stresses and secondary triggering; (d,h) model with coseismic stresses, afterslip and secondary triggering. RS parameters have been optimized for each case separately and they differ between models (see Table 4.1).*

agree with observed aftershocks (Fig. 4.3a-d); however, all models overestimate seismicity above the downdip edge of the fault plane and further inland. This is probably caused by the use of an homogeneous background rate, since positive ΔCFS can generate large seismicity in areas which are aseismic, where the background rate is in reality close to zero. This behaviour is accentuated by the inclusion of afterslip, which is concentrated at the downdip end of the fault plane. Models with afterslip also exhibit high seismicity rates at the downdip edge of the fault: this is an artefact due to the geometry of the slip model, which is composed of three sub-faults and presents a sharp change in dip at this depth. By calculating the log-likelihood excluding the bottom 3 km, I verified that this feature does not affect the ranking

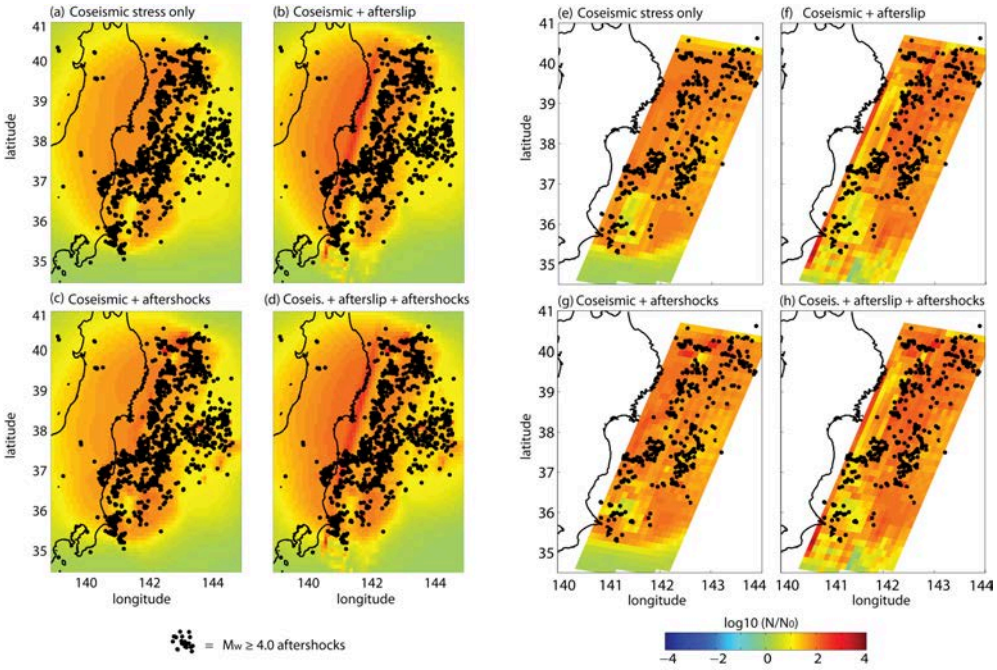

Figure 4.3: *Maps of forecasted seismicity between* 5 *and* 250 *days following Tohoku, with RS parameters optimized separately for each model (see Table 4.1). Coors and figure labels are the same as in Fig. 4.2.*

of the models. Fig. 4.3e-h shows the modeled and observed seismicity within 5 km of the slab. A qualitative inspection of Fig. 4.3f suggests that aftershocks are located at the edges of the afterslip patch, and not in the centre: this is in agreement with the lower seismicity rates predicted in the afterslip area, and consistent with triggering from the stress concentration at the edges of the area of afterslip. On the other hand, more careful observation indicates that some of the events occur within the area of predicted low seismicity; I return to the effect of afterslip on individual events in section 4.3.5, and discuss the uncertainties affecting the modelling of on-fault seismicity in section 4.4.

4.3.4 Temporal distribution

To first degree, all models provide a good fit to the observed seismicity (Fig. 4.4), but some discrepancies are present. The N-test [*Zechar et al.*, 2010] can be used to assess whether models underestimated or overestimated seismicity rates. I performed this tests on individual 24 h forecasts: Table 4.2 summarizes the results. We find that daily forecasts pass the N-tests on $92-97\%$ of days for Parkfield, and between $76-87\%$ for Tohoku; all models tend to underestimate seismicity more often than

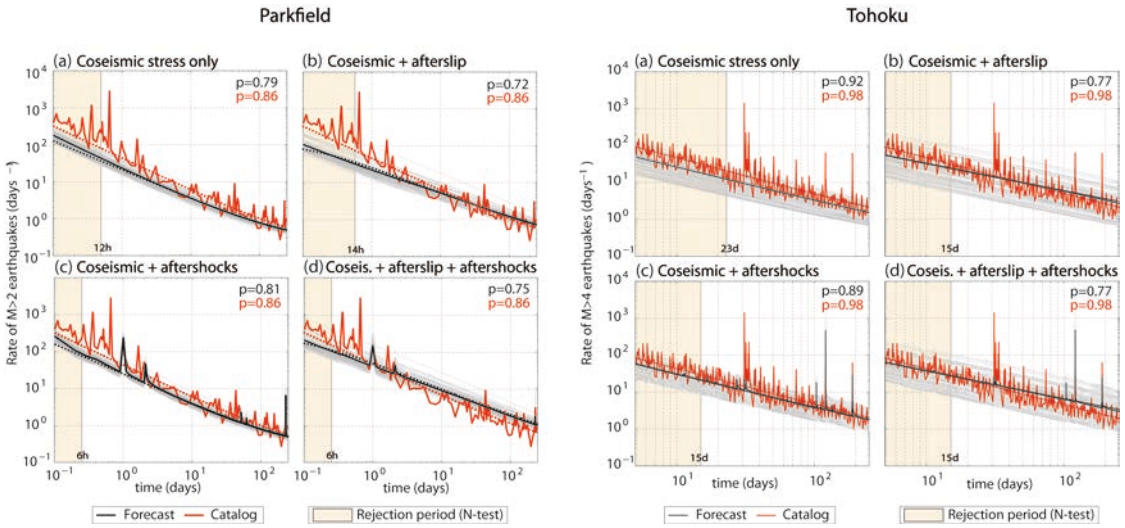

Figure 4.4: *Temporal evolution of seismicity following Parkfield (left) and Tohoku (right). Black lines: forecasted seismicity rates; Red lines: observed rates. Each grey line represents seismicity resolved on a different receiver fault from the catalogue of past focal planes, and the forecast is given by their average (details on the choice of receiver planes can be found in Cattania et al. [2014]). Dotted lines indicate the Omori fit obtained using log-likelihood maximization (for the catalogue), or a least square fit (for the model forecasts), and the corresponding Omori p-values are given. The shaded areas indicate time periods during which the forecasts are rejected based on a hourly N-test (quantile score δ_1 at a 0.1 significance level).*

they overestimate it, with the exception of model 3 for Parkfield. In both cases, model 0 is rejected most often, indicating that modeling of postseismic processes makes the models more successful. All models underestimate seismicity and fail the N-test at the start: for Tohoku, model 0 is rejected in the first 23 days, and models 1-3 in the first 15 days. All models are rejected in the first day for Parkfield: an hourly N-test performed on the first day of seismicity for Parkfield indicates that models 2 and 3 are rejected in the first 6 h, while models 0 and 1 are rejected in the first 12 and 14 h respectively.

Afterslip leads to higher seismicity rates at later times, and hence lower Omori p-values: while the total number of events is better estimated (Table 4.1), the fit to the temporal decay worsens, as indicated by the Omori p-values reported in Fig. 4.4. I will return to a discussion of the misfit between the observed and modeled Omori decay in section 4.4.6.

(a) Parkfield

Model	No. of days with $\delta_1 < 0.05$	No. of days with $\delta_2 < 0.05$	Percentage of days passing the N-test
0	18	0	93%
1	7	0	97%
2	13	1	94%
3	2	9	96%

(b) Tohoku

Model	No. of days with $\delta_1 < 0.05$	No. of days with $\delta_2 < 0.05$	Percentage of days passing the N-test
0	59	0	76%
1	29	8	85%
2	44	1	82%
3	22	13	86%

Table 4.2: *N-test results obtained with a sliding window of 24 h. The second and third columns indicate the number of days rejected by the N-test at a significance level of 0.1, respectively due to underestimation and overestimation of the number of events; a daily forecast passes the N-test if $\delta_1 \geqslant 0.05$ and $\delta_2 \geqslant 0.05$.*

4.3.5 Effect of postseismic stresses on individual events

In order to study the impact of postseismic stresses without the bias introduced by different constitutive parameters, I compare models with fixed rate-and-state parameters (for Tohoku, $A\sigma = 19$ kPa, $t_a = 8000$ days; for Parkfield, $A\sigma = 4$ kPa, $t_a = 8000$ days). To focus on the role of postseismic stresses on individual aftershocks, I compare the information gain of single events (Eq. 2.9).

When considering afterslip after Parkfield, I find the largest positive information gains for a band of events at ~ 5 km depth, and for a cluster of deeper events (~ 10 km), respectively updip and at the North-West edge of the afterslip area (Fig. 4.5a). Negative I_{ev} are instead found for deeper earthquakes, within the afterslip patch. The values of I_{ev} do not appear to be time-dependent (Fig. 4.5c).

Also for Tohoku, most of the negative information gains come from events at the downdip end of the fault, in the vicinity of the maxi-

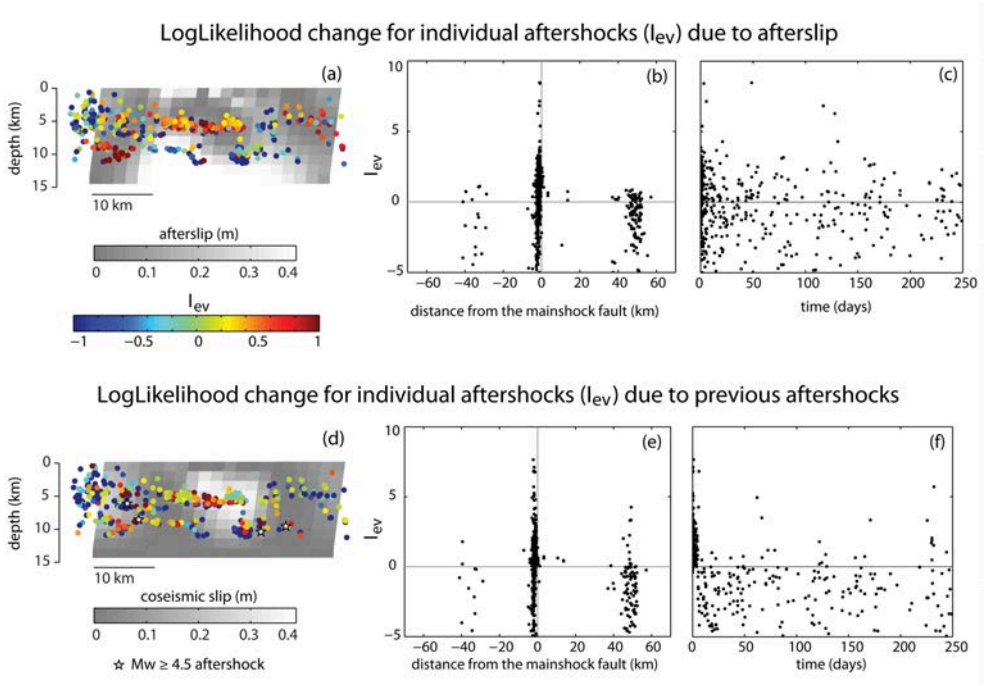

Figure 4.5: *Change in log-likelihood (I_{ev}) for individual events between model o and models including postseismic stresses, with fixed RS parameters, for the Parkfield sequence. (a-c): Comparison to models including afterslip. (a) Map view, with aftershocks colour coded by I_{ev}; (b) I_{ev} vs. distance from the mainshock fault plane; (c) I_{ev} vs. time. (d-f) Comparison to models including secondary triggering.*

mum afterslip (Fig. 4.6a); while an increase in probability is observed for events further south-west, on the side of a high afterslip region. The I_{ev} values in Fig. 4.6b suggest that on-fault aftershocks are not, on average, encouraged by afterslip; a clear temporal trend is not visible in Fig. 4.6c.

The overall information gain is dominated by on-fault events, not only because they are more numerous, but also because they experience the most dramatic changes, being closer to the slip. However, off-fault seismicity is important to understand from the hazard point of view; and since stress calculations are more reliable in the far field, several Coulomb-based seismicity studies exclude the near-fault region [*King et al.*, 1994; *Toda et al.*, 2012]. A cluster of events at $\sim 35-50$ km above the fault exhibits positive information gains ($I_{ev} > 0$ for 81% of the events; red points in Fig. 4.6b), and an average probability gain of 1.17. These 187 events are mostly shallow ($4-12$ km), normal faulting earthquakes occurring in the vicinity of Fukushima (lat. $\sim 37°$N, lon. $\sim 140.5-141°$E), documented by *Imanishi et al.* [2012] and *Kato et al.* [2011]. They start 30

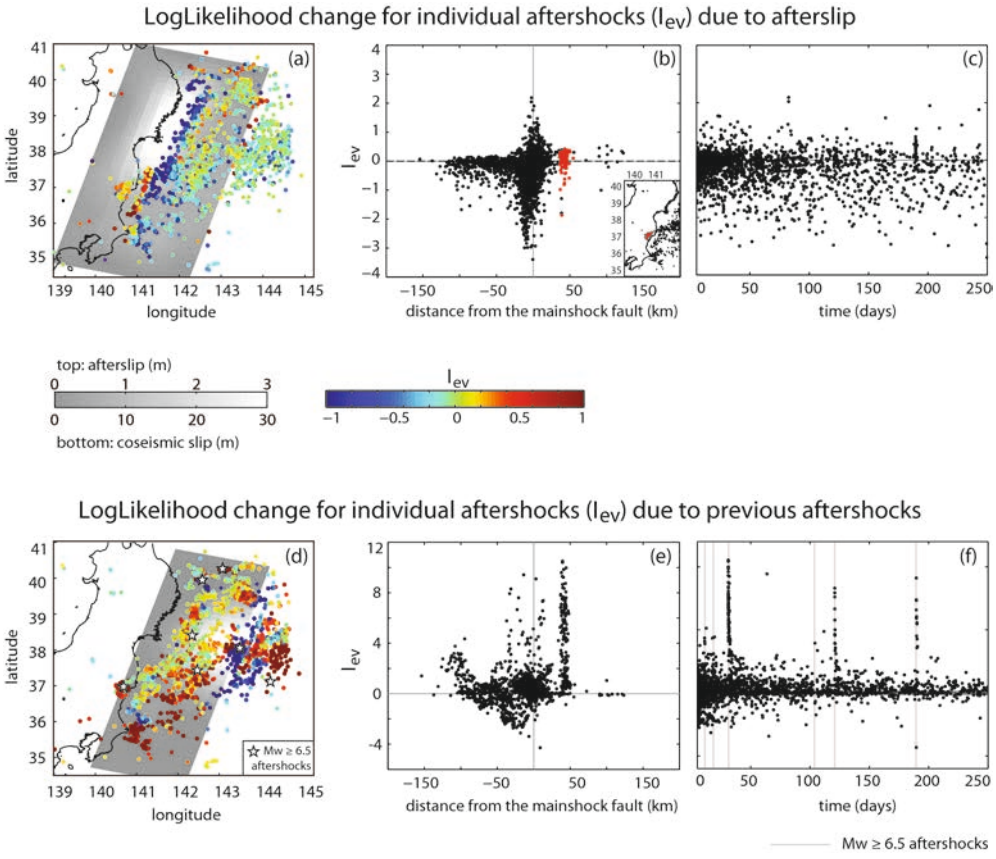

Figure 4.6: *Effect of afterslip and secondary triggering on individual events for Tohoku. Subfigures correspond to those in Fig. 4.5. Events in the vicinity of Fukushima (described in the main text) are highlighted in red, and they have an average probability gain* $G = 1.17$.

days after the mainshock and include one of the strongest aftershocks, the M_w7.1 Fukushima earthquake on April 11^{th}; when the contribution from afterslip is accounted for, the seismicity rate at the location and time of the this aftershock increases by 37%.

Fig. 4.5d-f, 4.6d-f indicate that secondary triggering leads to both positive and negative I_{ev}. Negative probability gains can be explained by two factors: firstly, aftershocks for which a synthetic slip model is used may produce stress shadows; secondly, models with secondary triggering forecast a larger number of events, so that the integral term in Eq. 2.9 gives a negative contribution. For Parkfield most of the positive probability gains are found at early times and close distances to the fault (Fig. 4.5e,f): since most of the aftershocks are aligned along a plane, they are likely to be triggered by previous events which generate $\Delta CFS > 0$ around their rupture area. For Tohoku, $I_{ev} > 0$ are found both in the near and in the far field (in the overriding plate and in the outer rise;

Fig. 4.6e).

4.4 Discussion and further analysis

In both case studies, I find an improvement in model performance when considering secondary triggering. The effect of afterslip is more subtle, and different between Parkfield and Tohoku: I will now discuss the limitations of the models, as well as testing the robustness of the result and their validity in a more general context.

4.4.1 Secondary Triggering

Modelling stresses from aftershocks is particularly challenging, since slip distributions or even focal planes are not always known. In fact, *Meier et al.* [2014] found that including ΔCFS from aftershocks decreases the predictive power of the Coulomb hypothesis; and *Segou and Parsons* [2014] found a negligible improvement in predictability. The difference between these results and the improvement in performance in my models may be due to the fact that, for most of the events, I assumed an isotropic stress field instead of the full stress field from the focal mechanism. The full stress field is highly sensitive to uncertainties due to the assumption of a uniform slip model and nodal planes uncertainties. Indeed I find, in agreement with *Meier et al.* [2014], that negative I_{ev} are in some cases associated with aftershocks with known focal mechanisms, for which I calculated a full anisotropic stress field. Due to the uncertainties involved in stress calculations, the use of an isotropic stress field seems preferable from the a forecasting perspective; and while not realistic from a physical point of view, this approach is in some way similar to methods used by statistical models such as the Epidemic Type Aftershock Sequences (ETAS) or smoothed seismicity models [*Ogata*, 1998; *Helmstetter et al.*, 2007]. Another aspect to keep in mind for secondary triggering is the model resolution: for computational reasons, the grid size was in both cases significantly larger than the rupture length of the smallest aftershocks, and the results may be sensitive to position of a source within a grid cell. Thanks to improvements in code performance implemented in the meanwhile (Chapter 6), it may be possible in the future to use a finer resolution across the entire domain and extend the model to even smaller magnitude; however, a strategy based on adaptive mesh refinement would be more appropriate.

4.4.2 Triggering of on fault aftershocks by coseismic stresses vs. afterslip

The inclusion of afterslip has a positive effect in model performance for Parkfield; in particular, reloading by afterslip improves the fit for events occurring within the rupture area, which experience negative coseismic stress. The overlap between aftershocks and the area of maximum coseismic slip, as well as the complementarity between coseismic and postseismic slip, are also observed with other published models [*Johnson et al.*, 2006; *Peng and Zhao*, 2009; *Langbein et al.*, 2006; *Barbot et al.*, 2009]. This is in contrast with the observation that generally only few aftershocks occur in regions of high coseismic slip [*Das and Henry*, 2003]; the different behaviour may be due to the fact that Parkfield was followed by an unusually large shallow afterslip, and reloading of the coseismic rupture area may have been more effective in this case than for the events analysed by *Das and Henry* [2003].

Based on stress transfer, the areas of the fault which experience the largest stresses from coseismic and postseismic slip are those located close to the edge of the slip area; on contrary, negative stresses are expected where the largest slip occurs. In order to model the stress generated by afterslip on neighbouring aftershocks, the spatial error from the afterslip model and earthquake location should be small enough to clearly establish their relative position. However, modelling choices such as fault geometry and smoothing may give rise to large differences between published slip models, as discussed in the next section.

Even if a slip model was a perfect description of the slip distribution at long wavelengths, uncertainties would still exist on small scales because slip inversions have smoothness constraints due to limited information: therefore inverted slip distributions are likely smoother than real ones. Various studies [*Mai and Beroza*, 2000] indicate that slip is fractal, and *Marsan* [2005] showed that the stress heterogeneity caused by fractal slip accounts for the observed seismicity in the vicinity of the fault; *Lengliné and Marsan* [2009] propose that small repeating earthquakes on or near the Parkfield rupture area are caused by a highly heterogeneous stress field.

Similar considerations also apply to the stress generated by afterslip. While afterslip is thought to have a smoother distribution than coseismic slip, a popular model of the subduction interface invokes heterogeneities in frictional properties [*Lay and Kanamori*, 1981]: isolated patches with velocity weakening friction (asperities) embedded in velocity strengthening material. In regions with a low density of asperities, earthquakes are decoupled and driven by the surrounding creep: the timing of repeating events lends support to this hypothesis [*Schaff et al.*, 1998]. This mechanism can not be captured by the model, since the seismic

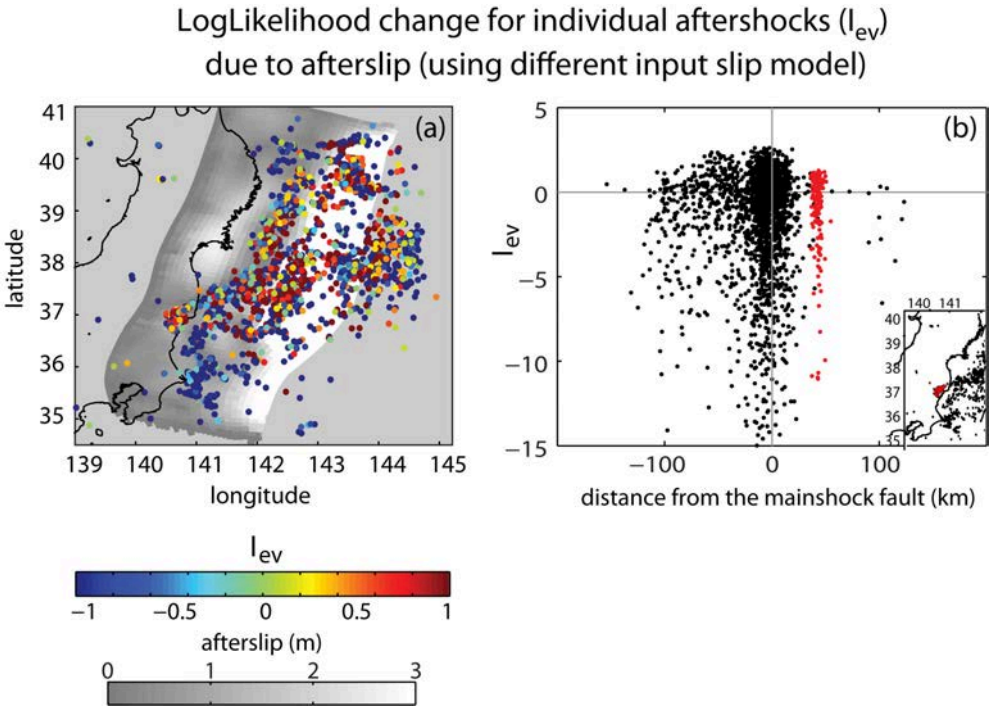

Figure 4.7: *Effect of afterslip on individual events using the coseismic and afterslip model of Perfettini and Avouac [2014]. (a) Map view; (b)* I_{ev} *vs. distance from the mainshock fault plane. To allow direct comparison with Fig. 4.6, distances from the fault are calculated with respect to the slip model of Wang et al. [2013].*

patches embedded in the afterslip regions are not resolved. This may account for the negative I_{ev} in Fig. 4.5a and 4.6a.

4.4.3 Sensitivity to the choice of slip model

Comparison of published afterslip models for the same mainshock indicates that the details of the slip distribution are not well defined, and the exact location of the afterslip following Tohoku varies between models [*Ozawa et al.*, 2011, 2012; *Perfettini and Avouac*, 2014]. As shown by *Rietbrock et al.* [2012] for the Maule earthquake, the discrepancies between slip models may be too large to draw clear conclusions about the relationship between slip and near field aftershocks.
To address this issue, I calculate I_{ev} from afterslip for the slip model of *Perfettini and Avouac* [2014],with fixed RS parameters ($A\sigma$ = 19 kPa, t_a = 8000 days). A comparison of Fig. 4.7 with Fig. 4.6 reveals that for events within 20 km from the fault interface, the effect of afterslip is very

Event name (year)	M_{post}/M_{co}	source
Sumatra-Nias (2005)	0.1	*Hsu et al.* [2006][a]
Tohoku (2011)	0.2 (0.07)	*Wang et al.* [2013]; *Ozawa et al.* [2012][b]
Maule (2010)	0.25	*Lin et al.* [2013][c]
Sumatra-Andaman (2004)	0.5	*Pritchard and Simons* [2006][d]
Chile (1960)	0.52	*Barrientos and Ward* [1990][e]

[a] The value given by the authors is mostly due to afterslip updip of the coseismic rupture; we estimated this value from the afterslip downdip of the coseismic rupture.

[b] Other authors report a higher value (0.4 in *Perfettini and Avouac* [2014], dominated by shallowed afterslip). The value in bracket refers to 30 days.

[c] In agreement with slip model from *Bedford et al.* [2013].

[d] A smaller value (0.3) is given by *Chlieh et al.* [2007], for a period of 40 days; however, the value of 0.5 better reflects the ratio between co/post-seismic slip in the vicinity of the Nicobar island, where several crustal aftershocks were observed [*Gomberg and Sherrod*, 2014]).

[e] Value obtained from the ratio of slip between patches which the authors interpreted as co/post-seismic.

Table 4.3: *Sources for the seismic moment ratios used in Fig. 4.8.*

sensitive to the choice of slip model. In the *Wang et al.* [2013] model, most events updip of the afterslip area do not experience significant information gains. On the other hand, the model of *Perfettini and Avouac* [2014], in which most of the afterslip is shallow and partially overlaps with the coseismic slip, exhibits more dramatic information gains. The large variability of I_{ev} seen in Fig. 4.7a can be attributed to the exact location of the events with respect to the megathrust, and to their timing within the sequence (early events are less affected by afterslip and have I_{ev} close to 0; see section 4.4.5). The cluster of shallow seismicity in the vicinity of Fukushima, however, presents more a consistent picture, since in both cases the probability of the events increases when considering afterslip. In spite of the negative I_{ev} seen in Fig. 4.7b, the average probability gain of the cluster is 1.31; the seismicity rate at the time and location of the Fukushima event increases by 306%. While this value is larger than the one obtained from the slip models of *Wang et al.* [2013], in both cases I see a significant increase in probability, indicating that the contribution of afterslip to the triggering of this aftershock is not negligible.

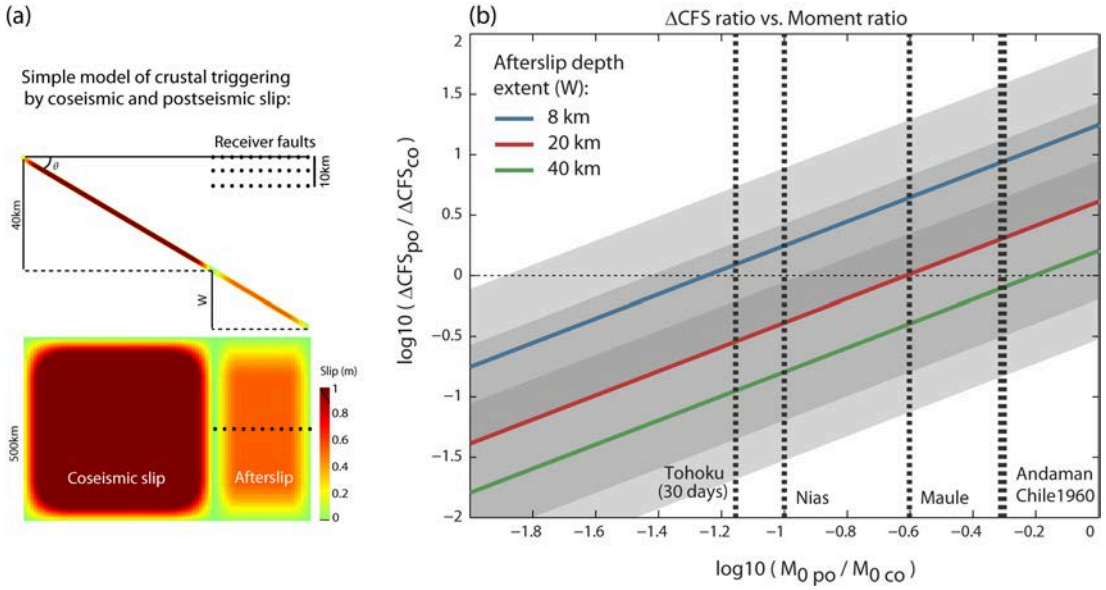

Figure 4.8: *(a) Simplified model of crustal triggering on the hanging wall by coseismic slip and afterslip, for faults located above patches of high afterslip. Coulomb stresses are calculated on receiver faults at the locations indicated by the dots; at each location, a set of receiver faults are used, with strike close to trench parallel (strike=*$0° \pm 10°$*,* $180° \pm 10°$*) and dip between* $60°$ *and* $90°$*. The dip of the slab is varied between* $10°$ *and* $20°$*; coseismic and postseismic slip are assumed to be uniform but tapered at the edges; a purely thrust mechanisms is assumed, and the slip is varied to produce moment magnitudes between* $M_w 8.0$ *and* 9.0 *(mainshock) and* $M_w 6.5$ *and* 9.0 *(afterslip).*

(b) Ratio between postseismic and coseismic stresses, as a function of seismic moment ratio. Each line corresponds to a different vertical extent of afterslip, corresponding to $20 - 100\%$ *of the coseismic rupture area. The grey area represents one standard deviation of the distributions obtained by varying the parameters described above. Vertical lines are the values of coseismic/postseismic moment ratio obtained from the literature (see Table 4.3).*

4.4.4 Triggering of shallow crustal events by deep afterslip in subduction zones

My models indicate that afterslip plays an important role in triggering a cluster of shallow, normal fault aftershocks in the Fukushima region; and this result is robust with respect to input coseismic and postseismic slip models. This observation is particularly relevant from a hazard point of view, since these are intra-plate events in the vicinity of urban centres, and they can be very destructive. The triggering of moderate size aftershocks in the hanging wall is a consistent feature of megathrust earthquakes: *Gomberg and Sherrod* [2014] showed that all $M_w \geqslant 8.6$ subduction mainshocks since 1960 triggered crustal events of $M_w \geqslant 5.5$, usually at a distance of few fault lengths. Afterslip is also frequently observed following megathrust events [*Pritchard and Simons*, 2006]. In particular, afterslip downdip of the mainshock rupture area is expected based on along-dip variations of the frictional properties of the fault: below the seismogenic depth, the fault is velocity strengthening and it responds to the coseismic stress changes by creep [*Hyndman et al.*, 1997; *Marone et al.*, 1991].

These considerations suggest that the enhancement of crustal seismicity by afterslip may be a common behaviour following megathrust earthquakes. While an exhaustive study of several cases is beyond the scope of this work, I tested the effect of afterslip for the M_w8.8 2010 Maule (Chile) earthquake on 27/02/2010, which was followed by intense crustal seismicity in particular in the vicinity of Pichilemu, including a M_w7.0 and a M_w6.8 aftershocks on March 11^{th} [*Ryder et al.*, 2012]. For this analysis, I used the slip models from *Bedford et al.* [2013] and events with $M_w \geqslant 2.0$ from the IPOC catalogue [*Lange et al.*, 2012], starting on March 15^{th}. Similarly to what observed for Tohoku, I find that the average probability gain of events within 5 km of the Pichilemu events is 1.76. Positive I_{ev} are also found for earthquakes further inland, at distances of more than 35 km above the fault (average probability gain = 1.52). The spread of I_{ev} for near fault events is also similar to what was observed for Tohoku. It should be noted that, unlike for Tohoku, for Maule the coseismic slip extends close to the crustal aftershocks near Pichilemu; in fact, *Ryder et al.* [2012] found that these events are consistent with static stress triggering from the mainshock. My results suggest that afterslip further enhances seismicity rates in an area which was already loaded by the coseismic stresses.

These findings may be surprising, since afterslip has a significantly lower amplitude than coseismic slip. A geometrical reason can be invoked to explain the results: for a shallow-dipping fault, deep slip may

be located directly underneath the continent, closer to crustal normal faults than near-trench slip. To explore this geometrical effect, and to generalize my results to other subduction settings, I perform a Coulomb stress analysis for a simplified model of subduction, depicted in Fig. 4.8a. Based on the analysis of *Ruff and Tichelaar* [1996], I assume coseismic slip extending down to a depth of 40 km, and afterslip on the same fault, directly downdip of the coseismic rupture; I vary the dip of the slab and the location and orientation of the receiver faults, located above the afterslip patch. For each of these different geometries, I calculate the ratio between postseismic and coseismic stresses as a function of the ratio of co/post-seismic moment (Fig. 4.8b). Variations in the geometry of the receiver faults and slab dip introduce large variations in the stress ratio ($\Delta CFS_{po}/\Delta CFS_{co}$), but on average, postseismic stress changes exceed coseismic ones as long as the moment ratio is above ~ 0.6. These values can directly be compared with seismic moment ratio of past great subduction earthquakes (given in Table 4.3). Based on the results from *Gomberg and Sherrod* [2014], I consider events larger than $M_w \geqslant 8.6$; for each of these events, visual comparison between the location of crustal aftershocks [*Gomberg and Sherrod*, 2014] and published afterslip models indicate that aftershocks have occurred close to the afterslip area, in agreement with the simple geometry in 4.8a; the only exception is the 1964 Alaska earthquake (according to the slip model of [*Suito and Freymueller*, 2009]). Fig. 4.8b indicates that, following these megathrust earthquakes, afterslip induced stresses on crustal faults were likely to be comparable to coseismic stresses, and may therefore have played an important role in triggering crustal aftershocks.

4.4.5 **Effect of stress evolution**

In addition to the location of afterslip, the large information gain obtained for off-fault events may be enhanced by the time dependence introduced by the rate-and-state seismicity response. In order to isolate this aspect, I calculated the seismicity rate for a single stress step followed by afterslip with the same time dependence as for the Tohoku model (section 4.2.1), and rate-and-state parameters as for Model 1 (Table 4.1 b); the amplitude of the postseismic stress is varied so that at $t = 30$ days the postseismic stress is between $1 - 50\%$ of the coseismic stress. Fig. 4.9 shows that, during the study period, the fractional change in seismicity rate introduced by afterslip exceeds the ratio between post and co-seismic stresses by a factor of $8 - 10$. For the Fukushima event, I find that this effect is more important than the geometrical aspect

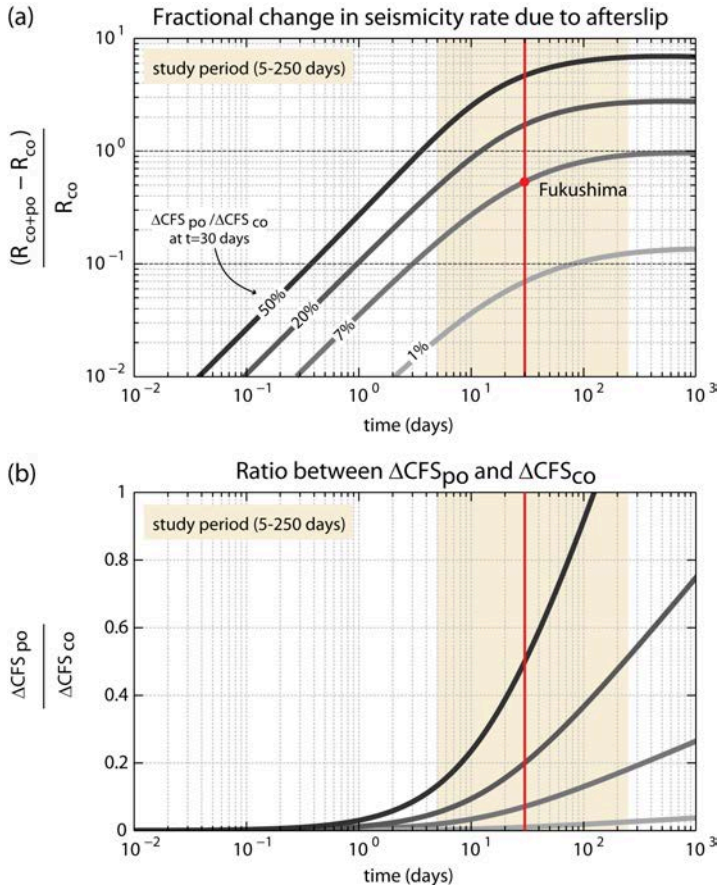

Figure 4.9: *Effect of time dependent stress changes on the seismicity rate, for a coseismic stress step of* $0.32\mathrm{MPa}$ *(the value calculated on the Fukushima fault);* $A\sigma = 19\mathrm{kPa}$, $t_a = 18000\mathrm{d}$. *The postseismic stress is given by* $\Delta CFS_{po}(t) = \alpha \log(t/14.2 + 1)$, *with* α *such that* $\Delta CFS_{po}(30\mathrm{d})$ *is between* $1-50\%$ *of the coseismic stress. (a) Fractional change in seismicity rate due to the effect of afterslip. (b) Temporal evolution of* ΔCFS_{po} *normalized by coseismic stress, for the same curves as in (a). The red line indicates the time of the Fukushima aftershock.*

described above: the postseismic stress calculated directly on the focal plane of this aftershock is ~ 7% of the coseismic stress; however, the enhancement in seismicity is 53%. It has been suggested that, despite generating small stresses compared to coseismic slip, afterslip drives aftershock sequences [*Perfettini and Avouac*, 2004]. While my models also include coseismic stresses, these results confirm that the time dependence of afterslip makes it a particularly effective triggering mechanism, and that studies of earthquake triggering based purely on Coulomb stress analysis may severely underestimate the importance of afterslip at a given point in time.

4.4.6 **Omori decay**

All the tested models exhibit a slower time decay than the catalogue (Fig. 4.4): the underestimation of the Omori p-value can be due to several factors. In rate-and-state based seismicity models, the time dependence of seismicity depends on the interplay between a variable stressing rate, and the nucleation time scale imposed by the rate-and-state parameters. I tested a wide range of $A\sigma$, t_a to verify if a different choice of parameters would produce the observed temporal decay for Tohoku for a model with coseismic stresses and afterslip (Model 1): as shown in Fig. 4.10, I found similar p-values (close to 0.75) for all the parameter tested.

A second candidate are errors in the time dependent input data, in particular for the models which include aftershocks as stress sources: the incompleteness of the catalogue at early times will inevitably lead to underestimating early stresses over late ones, which may contribute to a slow decay in the modeled seismicity rate. I tested this possibility by creating a synthetic complete catalogue, from which I then removed early events using the detection rate function of *Ogata and Katsura* [2006]; I found that, in spite of the large difference in the total number of events used as sources (4885 and 3916), the difference in the time curves is negligible (less than 1%).

A third explanation for the p-value is the heterogeneity of the stress field. It has been shown [*Helmstetter and Shaw*, 2006] that stress heterogeneity leads to p-values smaller than 1, and decreasing with increasing width of the stress distribution. In the model, stress heterogeneity comes from two aspects: the used of multiple receiver fault orientations, and the spatial variability. The use of receiver fault orientations does not seem to be the most important aspect: the lines in Fig. 4.4, representing individual receiver faults, are almost parallel to the average, indicating the p-value

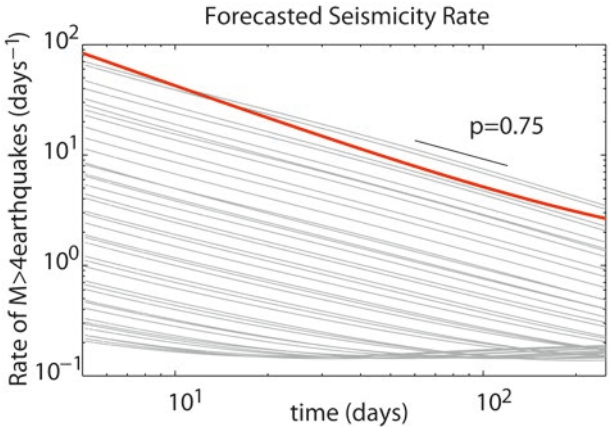

Figure 4.10: *Temporal decay following Tohoku, from Model 1 (with coseismic stresses and afterslip), and different values of* $A\sigma$ *and* t_a *(grey lines).* $A\sigma$ *was varied linearly between* 15 *and* 30 *MPa; to allow for a wider range of values,* t_a *was varied logarithmically between* 10 *and* 10000 *days. The red curve is the Omori fit to the observed seismicity (with* $p = 1.0$*).*

.

would not change significantly if stresses were resolved on a single receiver fault. The spatial heterogeneity of stresses may not have been overestimated in itself; however, by using a uniform background rate, I may have overestimated the importance of low stress areas, since the majority of the off-fault area is aseismic and would not contribute to the seismicity if a non-uniform background was used. I tested this aspect by running Model 0 for Tohoku with a non-uniform background rate, obtained from declustered, smoothed seismicity from 01/01/2010 until the mainshock, as using the methods described in Chapter 2. Fig. 4.11 indicates that using a non-uniform background leads to better temporal fit: the p-value increases from $p = 0.92$ to $p = 0.97$, very close to the observed value of 0.98.

Finally, I point out that in a space-time dependent model, the effect of afterslip in the temporal evolution of seismicity does not only depend on the slip rate, but also on the spatial distribution of the afterslip: in particular, since areas with positive coseismic ΔCFS dominate early seismicity, the sign of the afterslip-induced ΔCFS in these regions may determine whether the net effect of afterslip is to accelerate or slow down seismicity. To test how these uncertainties in the spatial distribution of ΔCFS may affect the temporal evolution of seismicity, I use a simple model comprised of two regions, experiencing coseismic stresses of ± 0.1 MPa. Postseismic stresses with a logarithmic time dependence ($\tau \propto \log(1 + t/t^*)$, $t^* = 14$ days) are superimposed to each region, reaching a value of ± 0.05 MPa in 250 days. I computed seismicity evolution us-

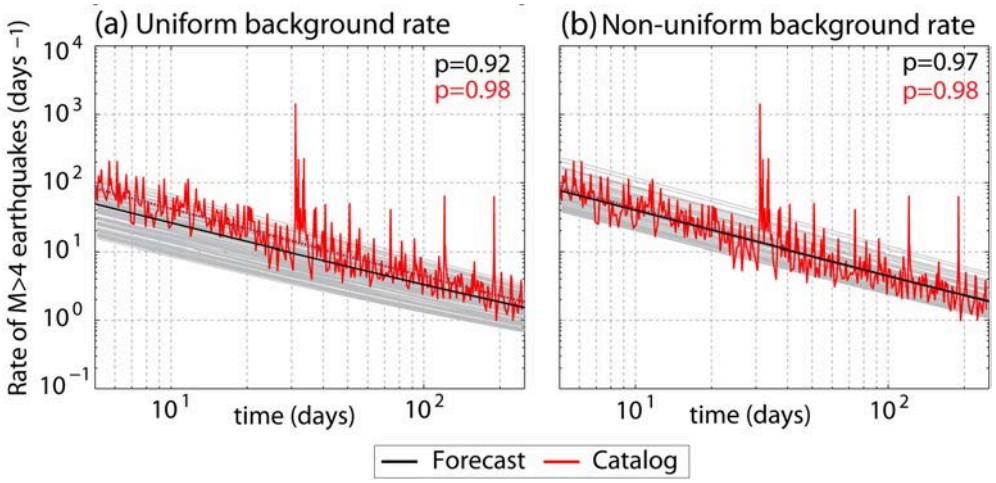

Figure 4.11: *Comparison between seismicity decay obtained by assuming uniform (a) or non-uniform (b) background seismicity, for the Tohoku sequence. The non-uniform background seismicity model was calculated for the period between 01/01/2010 and the mainshock, using the nearest neighbour algorithm [Helmstetter et al., 2007], after declustering the catalogue with the window method introduced by [Gardner and Knopoff, 1974]. I find that the increase in the Omori p-value is a robust observation with respect to variations of the minimum smoothing distance, the cut-off magnitude and the length of time window of the catalogue.*

.

ing equation B21 from *Dieterich* [1994], and compared a case in which the sign of co/post-seismic stresses is the same in each region, and a case in which they are instead anti-correlated. Fig. 4.12 shows that the two cases result in very different Omori p-values (1.65 and 0.85 respectively), indicating that the spatial distribution of slip may have a profound role in determining the temporal evolution predicted by CRS models.
By using a space-independent CRS formulation, *Savage* [2010] obtained a good fit for the decay of aftershocks following Parkfield. While Fig. 4.4 seem to contradict these results, I conclude that the sensitivity of a space dependent model to the background seismicity and to the relative location of co/post-seismic stress changes make it challenging to obtain reliable results on the time decay of seismicity.

4.4.7 Modelling assumptions

In addition to the uncertainties related to the input data, several simplifications are made in the models. I focus on two sources of time depen-

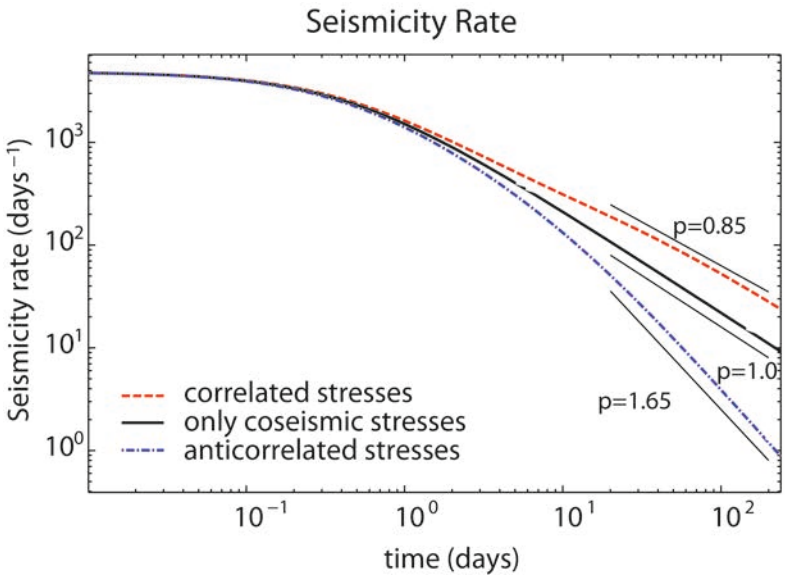

Figure 4.12: *Temporal evolution of seismicity for the simple model described in the text. The black, red, and blue line corresponds to models without afterslip; with afterslip correlated to coseismic slip; with afterslip anti-correlated with coseismic slip. The total coseismic and postseismic stresses are the same in all cases.*

dent stresses, and neglected the impact of viscoelastic relaxation and poroelastic effects. Viscoelastic relaxation typically acts on a longer time scale than afterslip, and its contribution may be negligible in the time frame I consider [*Diao et al.*, 2014]. On contrast, poroelastic effects as expected on the same time scale as afterslip, but modelling them would require detailed assumptions on the poorly constrained value of the hydraulic diffusivity in the seismogenic volume.

The consideration of stress heterogeneities has a profound impact on CRS models. I take into account one source of stress variability, namely the existence of multiple receiver fault orientations, by sampling from the catalogue of previous focal planes: as described in Chapter 3, I considered to some extent the spatial variations in the distribution of focal planes. However, a more detailed consideration of spatial variability may be implemented, in particular by including information of the existing fault systems. Finally, the assumption of uniform background seismicity is an oversimplification, and as shown in section 4.4.6 it can significantly affect model behaviour: stable estimations of the background rate are therefore an important challenge for the future.

4.4.8 Relevance for operational earthquake forecasting

In the case studies considered here, model performance improves significantly when secondary triggering is taken into account: this result may explain, to some extent, the poor performance of CRS models compared to statistical models which explicitly or implicitly include the effect of previous aftershocks, such as the ETAS models or smoothed seismicity models [*Woessner et al.*, 2011]. I point out, however, that this study represents a best case scenario, since I used earthquake catalogues released months after the mainshock, with a lower completeness magnitude and smaller errors than real time data. Further testing, especially in a prospective setting, should be carried out to verify the generality of these findings and the potential gains for earthquake forecasting. A step in this direction is the submission of CRS models to CSEP testing centre for retrospective performance evaluation, an example of which will be presented in Chapter 5.
My approach to the inclusion of afterslip data is also not applicable to an operational forecasting setting, since afterslip models are currently not available in real time; moreover, including afterslip may not be beneficial in terms of model performance, as measured by log-likelihood. On the other hand, the observation of crustal seismicity being favoured by afterslip seems a robust feature of the model for the Tohoku sequence, and it may be a common feature following megathrust earthquakes. While detailed modelling of afterslip may not be feasible in real time, monitoring of crustal deformation may be used to directly estimate the stress increases, and hence the triggering potential, in these areas.

4.5 Conclusions concerning the effect of postseismic stress changes

I performed a study on the role of postseismic stresses in triggering aftershocks, based on Coulomb stress transfer and the rate-and-state constitutive law of earthquake nucleation.
In terms of model performance, I find that stress redistribution by aftershocks plays a first order role, in spite of the fact that aftershocks account for a small fraction of seismic moment compared to the mainshock and afterslip. This result may explain, to some extent, the poor performance of physics-based seismicity models compared to statistical models which take into account secondary triggering [*Woessner et al.*, 2011].

The effect of afterslip on model performance is more difficult to assess. In the vicinity of the rupture plane, where slip model uncertainties are large and the relative location of afterslip and aftershocks is not well determined, robust conclusions on the role of afterslip for triggering aftershocks are difficult to draw, especially for Tohoku. For Parkfield, reloading by afterslip may explain the occurrence of aftershocks on the coseismic rupture area, a feature common to several coseismic slip models; however, this observation can also be explained by unresolved small scale slip heterogeneity, and the relative role of the two factors remains an open question. At distances further than few tens of kilometres from the mainshock fault, I find that afterslip generally enhances seismicity; in particular, crustal inland aftershocks in the Fukushima region following the Tohoku earthquake are promoted by afterslip. The enhancement of shallow seismicity in the hanging wall by afterslip seems to be a common feature of large subduction earthquakes: a simple model of afterslip following great megathrusts indicates that, for typical seismic moment ratios, trench parallel crustal fault systems experience higher stresses from afterslip than would be expected based on its seismic moment. Given the hazard posed by onshore aftershocks, the topic deserves further study: in particular, I suggests that a more detailed description of the fault orientation in these areas, as well as consideration of viscoelastic and poroelastic response, could give more insight on the seismic activation of these regions. Finally, I show that afterslip time dependence is an important aspect to consider: in the study period, the effect of postseismic stresses on seismicity rate is amplified by the rate-and-state response of the model, and the triggering potential of afterslip at later times would be severely underestimated by a time-independent Coulomb stress analysis.

5

RETROSPECTIVE EVALUATION DURING THE CANTERBURY SEQUENCE

The results presented in the previous chapters indicate that CRS models can be improved by including stress uncertainties and postseismic stresses. However, rigorous testing is necessary to assess the potential benefits of these methods for operational forecasting. To this end, I have submitted the models for retrospective evaluation of the 2010-2011 Canterbury (New Zealand) sequence. This experiment is initiated by the EU-project REAKT and carried out by the Collaboratory for the Study of Earthquake Predictability (CSEP). It consists of a comparison between fifteen forecasting models, including statistical and physical ones. In this chapter I will describe the CRS models I submitted to this experiment, and outline some preliminary results released by CSEP. These indicate that CRS models including stress uncertainties outperform statistical models, in stark contrast to previous studies [Woessner et al., 2011]. These results are in agreement with the case studies presented in the previous chapters, and encouraging for the future of CRS models in operational earthquake forecasting.

About 60% of the material presented in this chapter has been published in the following conference contribution:

- Werner, M. J., W. Marzocchi, M. Taroni, J.D. Zechar, M. Gerstenberger, M. Liukis, D. A. Rhoades, **C. Cattania**, A. Christophersen, S. Hainzl, A. Helmstetter, A. Jimenez, S. Steacy, T. H. Jordan, Retrospective Evaluation of Earthquake Forecasts during the 2010-12 Canterbury, New Zealand, Earthquake Sequence, *presented at 2014 Fall Meeting, AGU, San Francisco, Califor., 15-19 Dec.*, pp. S23A–4481, 2014.

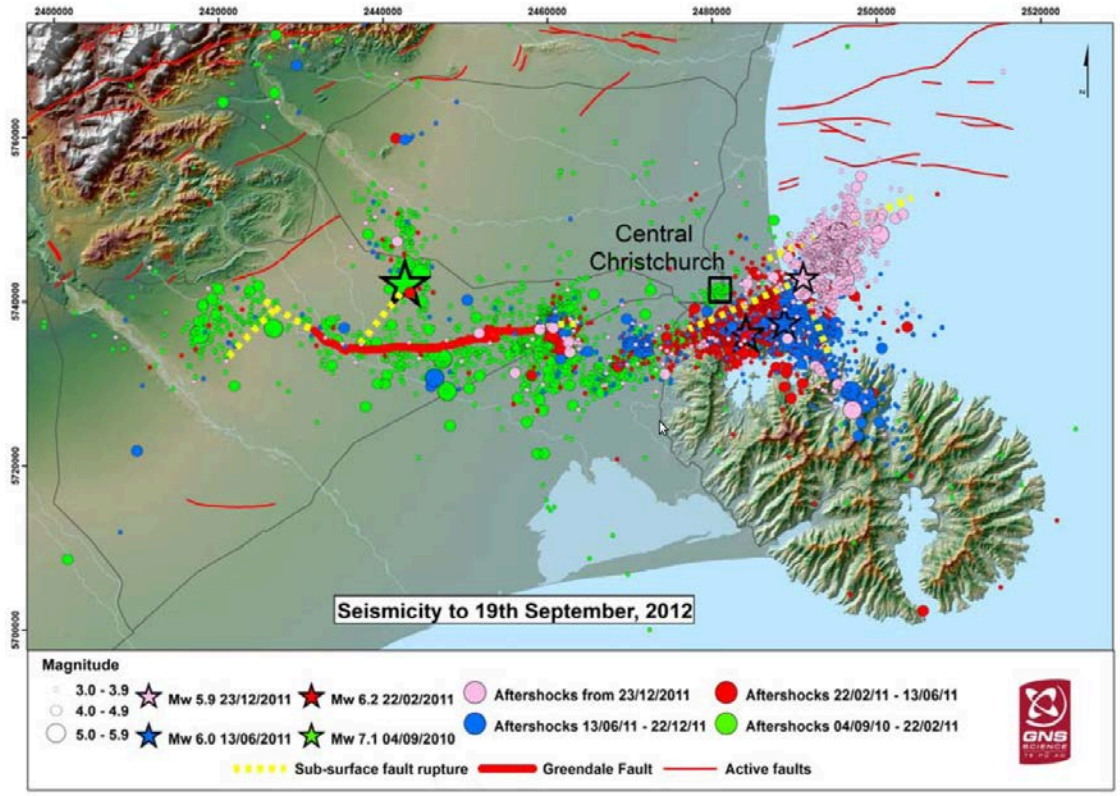

Figure 5.1: *Map of the aftershock sequence following the 2010 Darfield earthquake, showing the eastwards migration of seismicity. Figure prepared by Rob Langridge and reproduced from Christophersen et al. [2013].*

5.1 Introduction

The M_w7.1 Darfield earthquake on 04/09/2010 was followed by a vigorous aftershock sequence: more than 500 $M_w \geqslant 3.95$ events were recorded in 2 years in the study area (Fig. 5.1), three of which exceeded M_w6.0. These larger aftershocks occurred at a distance of 42-47 km east of Darfield epicentre, and they presented particular hazard due to their proximity to the city of Christchurch: the M_w6.3 earthquake on 22/02/2011 was particularly damaging, with casualties and damage vastly exceeding those of the Darfield earthquake itself.

Given the efforts under way to implement operational earthquake forecasting [*Jordan et al.*, 2011], rigorous and independent testing of candidate models is fundamental. The rich datasets collected during this sequence provide the possibility to test and compare the performance of medium-term forecasting models in a blind, pseudo-prospective setting.

5.2 Data

We used two types of datasets: the best available data, and near-real-time data. The best available data comprises the GeoNet catalogue earthquake catalogue available at the time of the experiment, with reviewed source parameters, and the slip model from *Beavan et al.* [2012], published in 2012. The near-real-time dataset consists of a preliminary GeoNet catalogue downloaded with a 30-day delay, and the preliminary slip model by *Holden et al.* [2011]. Additionally, CRS models used a focal mechanism catalogue also provided by GeoNet, which includes 848 events between 21/08/2003 and 03/09/2014, 728 of which occurred before the Darfield event. The target earthquakes against which model performance is tested are $M_w \geqslant 3.95$ from the reviewed GeoNet catalogue.

5.3 Testing setup and models submitted

Fifteen models (described in Table 5.1) have been submitted to the Collaboratory for the Study of Earthquake Predictability (CSEP); forecasts are generated and evaluated in a CSEP testing centre, and not by the modellers.

The output of each model is a gridded forecast of the number of events expected in a given forecast horizon. The grid provided by CSEP corresponds to the area between 170.5° and 174.0° lon, −44.5° and−42.4° lat, with 0.05° spacing, and a single depth layer between 0 and 40 km. Magnitude bins with 0.1 spacing, starting from M_w 3.95 are used, the last of which has no upper bound.

Forecasts are produced for successive time intervals. Three forecast horizons are tested: 1 day, 1 months, and 1 year (Table 5.2). In some forecasts, the models are updated after each $M_w \geqslant 6.0$ earthquakes, as would be done in a real-time scenario. An important difference between this test and the applications presented in Chapter 3 and Chapter 4 is that the models are run in truly pseudo-prospective mode: the data used to produce each forecast only includes stress sources up to the start time of the forecast.
I submitted 5 CRS models, with the following features:

- **CRS**0: uses Coulomb stresses imparted by mainshocks (the four events with $M_w \geqslant 6.0$) resolved on planes on which the total stress field is maximum (Optimally Oriented Planes).

Type	Name	Description	Modellers (reference)
Physical	CRS0	no uncertainties no secondary triggering	Cattania [*Cattania et al.*, 2014]
	CRS1	uncertainties no secondary triggering	Cattania [*Cattania et al.*, 2014] (Chapter 3)
	CRS2	uncertainties sec. trigg. if focal mech. available	Cattania [*Cattania et al.*, 2015] (Chapter 4)
	CRS3	uncertainties sec. trigg. from all earthquakes	Cattania [*Cattania et al.*, 2015] (Chapter 4)
	CRS4	uncertainties; sec. trigg. from all earthquakes non-uniform background rate	Cattania (Chapter 2)
Statistical	ETAS0	ETAS; uses distance from epicentre	Hainzl [*Bach and Hainzl*, 2012]
	ETAS2	ETAS; uses distance from fault	Hainzl [*Bach and Hainzl*, 2012]
	K2	Space-time smoothing, with Gutenberg-Richter	Helmstetter, Werner [*Helmstetter and Werner*, 2014]
	K3	Space-time smoothing, non-parametric	Helmstetter, Werner [*Helmstetter and Werner*, 2014]
Hybrid	ETAS1	ETAS; uses ΔCFS in space	Hainzl [*Bach and Hainzl*, 2012]
	RETAS0	RETAS; uses ΔCFS for tot. no. of earthquakes	Hainzl [*Zakharova et al.*, 2013]
	RETAS1	RETAS: uses ΔCFS in space	Hainzl [*Zakharova et al.*, 2013]
	RETAS2	RETAS; uses distance from fault	Hainzl [*Zakharova et al.*, 2013]
	STEP-Coulomb	STEP; uses sign(ΔCFS) in space	Steacy [*Steacy et al.*, 2014]
Reference	SUP	Uniform Poisson	Rhoades

Table 5.1: *List of models submitted to CSEP for testing.*

Forecast length	Forecast periods
1 year	1 x 1 year, and 1x scaled 1-year period (to Feb 2012)
	4 x 1 year periods, updated immediately after large quakes
1 month	20 x 1 month periods, updated after large quakes
1 day	in progress

Table 5.2: *List of forecast periods.*

- **CRS**1: uses Coulomb stresses from mainshocks, and it includes uncertainties from receiver fault orientation, as described in Chapter 3.
- **CRS**2: uses Coulomb stresses from all events with a focal mechanism, by creating a synthetic slip model (as described in Chapter 4). Uncertainties are treated as in CRS1.
- **CRS**3: uses Coulomb stresses from all events, using an isotropic stress field for events with $M_w < 6.0$ (as described in Chapter 4). Uncertainties are treated as in CRS1.
- **CRS**4: like CRS3, but uses a non-uniform background rate calculated from background seismicity.

Since Coulomb stress calculations require a smaller grid than the one provided, all models perform the stress calculations on an internal grid with a finer resolution. This is achieved by subdividing each cell into smaller cells, until the required minimum resolution is obtained. I set minimum resolution of 4 km both horizontally and vertically; in practice, the final resolution is 2.02 x 2.78 x 4.0 km (along latitude, longitude, depth), with an increase in the number of cells of a factor of 400.
All models use the input earthquake catalogue to invert for rate-and-state parameters (see Chapter 3). The search ranges are set to $[0.01 - 0.1]$ MPa for $A\sigma$ and $[5000 - 10000]$ days for t_a; the background rate r_0 is also optimized, using the analytical solution which maximizes the log-likelihood. In models CRS4, the spatially variable background rate is calculated from the seismicity catalogue, as described in Chapter 2.
In order to calculate the number of earthquakes in each magnitude bin, the number of earthquakes predicted in each cell is distributed across magnitude bins according to the Gutenberg-Richter distribution: $N(m \geqslant M) \propto 10^{-bM}$, where N is the number of earthquakes with magnitude exceeding M. The b-value is estimated from the input catalogue using a maximum curvature method [*Zhuang et al.*, 2011].

5.4 Preliminary Results

5.4.1 Forecast maps

Fig. 5.2 shows the forecasted seismicity for selected models, with a forecast horizon of 1 month and 1 year. None of the CRS models presents clear stress shadows. For model CRS0, this is due to resolving stresses on Optimally Oriented Planes, which by definition tend to favour positive ΔCFS; for CRS2, the suppression of stress shadows can in part be explained by the use of Monte Carlo iterations for multiple receiver faults, as explained in Chapter 3. In both models, seismicity at each grid point is obtained by summing up the contribution from the cells in the refined calculation grid: this effect is analogous to the suppression of stress shadows observed in Chapter 3 (section 3.7.1).
Both CRS models produce a smoother forecast than the other tested models, i.e. they have low specificity [*Kagan*, 2014]. This is in part is a direct result of including uncertainties, and averaging over several receiver faults or sub-cells, and as such may be interpreted as a measure of the uncertainty in the forecast. Additionally, the smooth distribution is an artefact due to the use of a uniform background rate, since this assumption neglects the fact that earthquakes concentrate along fault structures, and do not occur homogeneously throughout the crust.

5.4.2 Performance

Models will be compared across a range of statistical tests [*Zechar et al.*, 2010]: the N-test, to assess the ability to estimate the total number of earthquakes; the S-test, to assess the accuracy in the spatial distribution; the M-test, which compares the forecasted and observed magnitude distributions; and the T-test, which compares the Information Gain between two models (see Chapter 2). At the moment, only results of the T-test are available (Fig. 5.3).

For forecasting horizons of 1 year and 1 month, physical and hybrid models perform better than purely statistical models. Fig. 5.3 indicates that CRS models perform generally well: when the best available data is used, CRS$2-3$ and STEP-Coulomb are the most successful models.
Comparison of the performance of CRS0 versus CRS$1-3$ indicates that the use of variable receiver fault orientations (implemented in CRS$1-3$ but not in CRS0) improved model performance. However, this difference is in some cases minor compared to the difference between CRS models and others. The inclusion of more earthquakes as stress sources

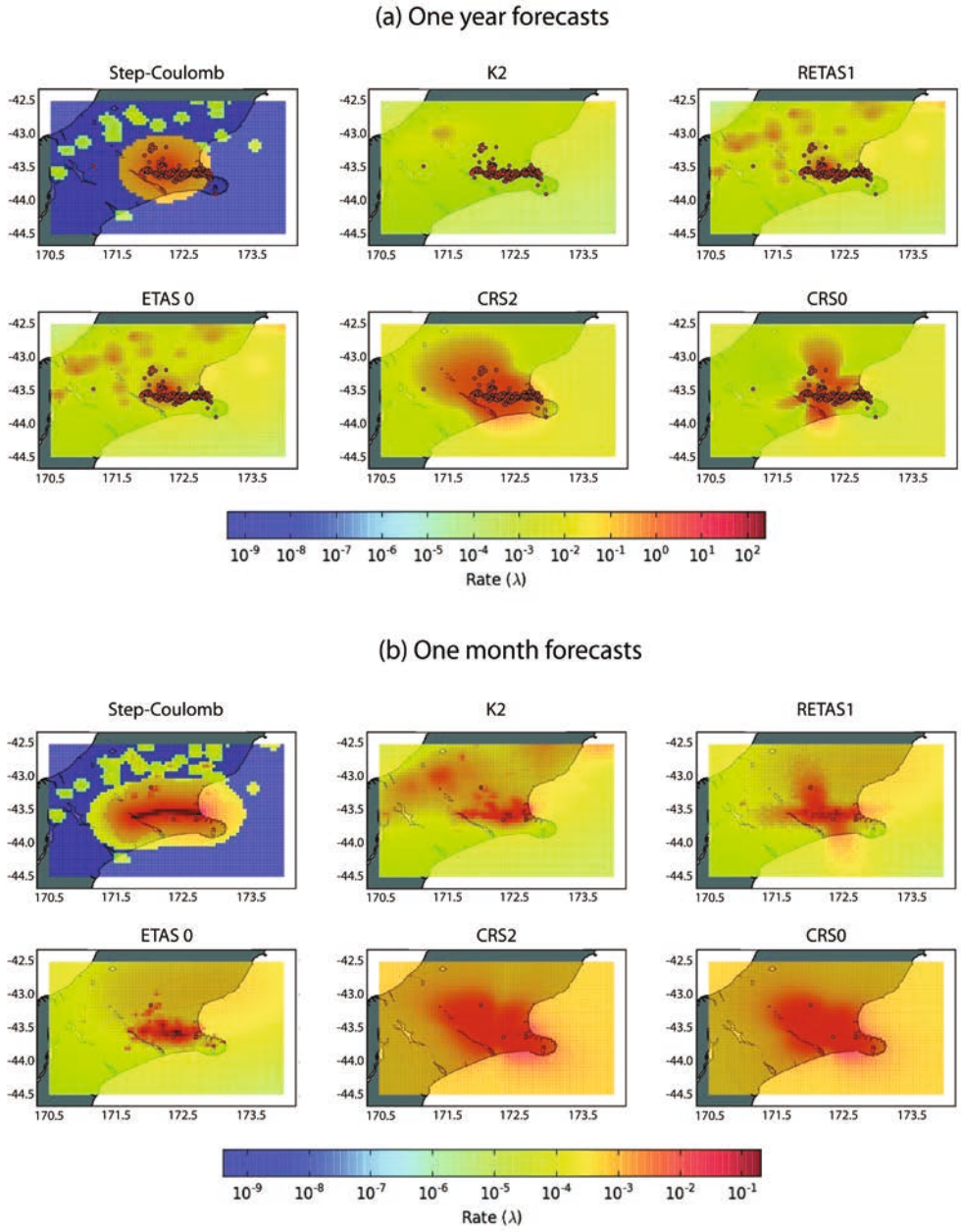

Figure 5.2: *Forecast produced by a representative sample of the models. Top:* 1 *year forecasts starting immediately after the Darfield earthquake. Bottom:* 1*-month forecasts leading up to and including the February 2011 Christchurch earthquake. Red circles denote observed earthquakes. .*

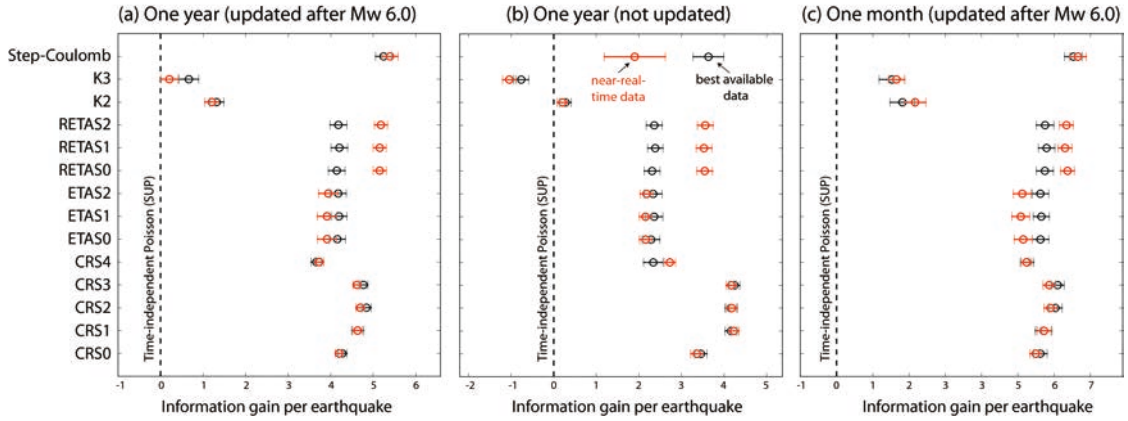

Figure 5.3: *T-test results. (a) Information gains of* 1*-year forecasts using best-available data (black) and near-real-time data (red) as model input, with forecasts updated immediately after large earthquakes. (b) Information gains of* 1*-year forecasts, not updated after large earthquakes. (c) Information gains of* 1*-month forecasts updated immediately after large earthquakes.*

(CRS2 – 3) leads to no change for the 1-year forecast starting at the time of Darfield: this is obvious, since aftershock data is not yet available. A slight improvement in performance can be seen for the yearly forecast updated at the time of $M_w \geqslant 6.0$ earthquakes, but this is not significant within error; a larger improvement can be seen for the 1 month horizon, since the models are updated more often. CRS2 and CRS3 differ in the number of aftershocks included and how stresses are calculated (see Table 5.1); however, they have almost identical performance. Finally, the model including non-uniform background rate (CRS4) performs worst within the CRS class.

Compared to all other models, and in particular the others physical or hybrid ones, CRS models are the least sensitive to the quality of the data: while they perform slightly better with the best available data, their probability gains do not change within errors.

5.5 Discussion and Conclusions concerning the Canterbury experiment

These preliminary results suggest that including Coulomb stress information increases the predictive power of forecasts models. A similar experiment conducted on the 1994 Landers aftershock sequence [*Woessner et al.*, 2011] yielded almost opposite results: statistical models were

found to be more effective that physical ones.
The study by *Woessner et al.* [2011] also included CRS models with a stochastic component, which assumed ΔCFS to be Gaussian distributed with a standard deviation proportional to its absolute value [*Hainzl et al.*, 2009]. These models were found to be more effective than standard CRS models, which performed very poorly compared to statistical ones. These results are in agreement with the better performance of models CRS$1-3$ compared to CRS0; however, I find in this case that even CRS0, which does not employ a stochastic treatment, has comparable or better performance than the statistical models. This is most likely due to the use of a refined calculation grid and in particular the consideration of several depth layers, which is necessary to describe the details of the stress field. The stability of the models with respect to input data (real time vs. best available datasets) may also be due to the use of a refined grid: since the output forecast is an average over several grid points, the model is less sensitive to small scale changes in the stress field. This behaviour is particularly desirable in an operational forecasting context, in which only preliminary data is available. Therefore, the increased computational cost seems justified, and for this case study it is not prohibitive in terms of computational resources (the number of grid points was of the order of 10^5). Some of the regions currently tested in CSEP testing centres, however, are too large to allow for the resolution employed here (for example, current CSEP testing regions include the entire Japan; New Zealand; Italy; Southern California). In order to model the seismicity following large earthquakes, it would be necessary to implement a dynamic mesh refinement for a limited area and time period.
The improvement in performance when secondary triggering is included confirms the results presented in Chapter 4. Since forecasts are not updated continuously, the effect of secondary triggering is more pronounced for shorter forecast horizons: comparison on the 1 day forecasts will presumably shed more light on the effect of secondary triggering, and possibly on the differences between different treatments (CRS$2-3$).
The decrease in information gain when including non-uniform background rate is probably due to the fact that background seismicity is dominated by the Alpine fault system in the North-West corner of the forecast region, and the background rate estimation for the Canterbury plain is not reliable if too few events are available.

6

COMPUTATIONAL ASPECTS

In order to guarantee reproducibility, and to facilitate future applications of the models developed during this work, I have made the code publicly available through the version control platform "github". In this chapter, I describe how the code has been designed, with a focus on implementation details that have not been previously addressed, in particular optimization and parallelization strategies.

The material in this chapter will be submitted as:

- **Cattania, C.**, and F. Khalid, A parallel code to calculate seismicity evolution induced by time dependent, heterogeneous Coulomb stress changes, *in preparation for submission to Computers and Geosciences*.

The final version of the code will be available in a repository connected to the article. The current version of the code can be found at: `https://github.com/fkhalid/CRS`.

6.1 Introduction

The main capabilities of CRS have been introduced in Chapter 2 and developed in Chapter 3 and 4, and they can be summarized as follows:

- **Calculation of stresses from multiple seismic sources.** Stresses can be calculated from user provided slip models, from synthetic slip models calculated at run time (see Chapter 4) or using a spherically symmetric approximation. Synthetic slip models are tapered to avoid unphysical slip gradients at the edges; the patch size used for tapering is defined by the user.
- **Calculation of time dependent aseismic stresses.** If afterslip has a stationary patter, it may be represented by a single slip model

and a logarithmic temporal function (Eq. 4.1). Alternatively, the user may provide any number of snapshots representing a non-stationary afterslip, which will be fit by using splines as described below. Finally, externally calculated time dependent loading may be provided by the user, in order to include aseismic processes other than afterslip.

- **Estimation of aleatoric and epistemic uncertainties.** As described in Chapter 3. A set of alternative slip models can be provided, and the rate-and-state parameters will be calculated independently for each model; the creation of an ensemble model is not part of the program.
- **Consideration of spatially variable background seismicity rate.** As described in Chapter 2, the user may choose to use a spatially uniform background rate, or a spatially variable background rate calculated from a seismicity catalogue at run time; alternatively, one may provide a pre-calculated background rate in a gridded format.
- **Choice of receiver faults.** The user may choose to resolve stresses on Optimally Oriented Planes, on a set of receiver faults from a focal mechanisms catalogue, or to provide a grid with a single fixed receiver fault at each grid point [*Segou et al.*, 2013; *Toda and Enescu*, 2011]. In this case receiver faults will not be considered as a source of uncertainty.

6.2 Program description

The work flow of the program and its main capabilities were introduced in Chapter 2. Here I outline two aspects of the model implementation which have not previously been discussed: the use of a non-stationary afterslip model, and the numerical implementation of rate-and-state equations.

6.2.1 Fitting a slip history to non-stationary slip models

When the user provides a set of afterslip snapshots, the afterslip pattern is assumed to be non-stationary: the slip history may have a different time dependence on each patch. While the user may supply snapshots corresponding to arbitrary points in time, a finer temporal discretization may be required to correctly calculate seismicity evolution (see section 6.2.3): afterslip at intermediate time steps is calculated using

spline interpolation.
I find that on some patches, a simple spline interpolation leads to unphysical oscillations (Fig. 6.1(b)). In order to minimize this effect, I use a Monte Carlo method which takes into account the uncertainty of slip. For each patch, I perform the following steps:

1. For each snapshot provided by the user, I draw a value of slip from a doubly truncated Gaussian distribution centred at the given value, with the constraints that absolute value of slip is monotonically increasing or decreasing (i.e. slip doesn't reverse direction). This constraint does not apply if the unperturbed curve is already not monotonic (as in Fig. 6.1(b));

2. A natural spline is fit between the first snapshot ($t = t_1$) and the last one;

3. The period between $t = 0$ and $t = t_1$ is not included because the large displacement in the first day (with a slope much steeper than subsequent steps) produces later oscillations. Instead, I fit a quadratic function for this time period, such that $s(t = 0) = 0$ and the first derivative is continuous at $t = t_1$;

4. I repeat steps 1 to 3 a large number of times (500) and calculate the average between the splines.

For well-behaved time sequences (such as a logarithmic increase with time) a simple spline interpolation would be sufficient; as shown in Fig. 6.1(a), the two methods are almost identical in this case. On the other hand, the blue line in Fig. 6.1(b) shows that for some patches fitting a spline without considering uncertainties produces an unphysical slip history with slip frequently reversing direction, while the method described above (red line) reduces oscillations. A snapshot close to the end time of the calculation period (approximately 70% between $t = 0$ and the end) should be provided by the user, since the value of the spline functions may grow rapidly in a region in which they are extrapolated.
While this procedure is more general and captures the full spatio-temporal evolution of stress, it is also computationally more expensive due to $S(t, x)$ being non-separable.

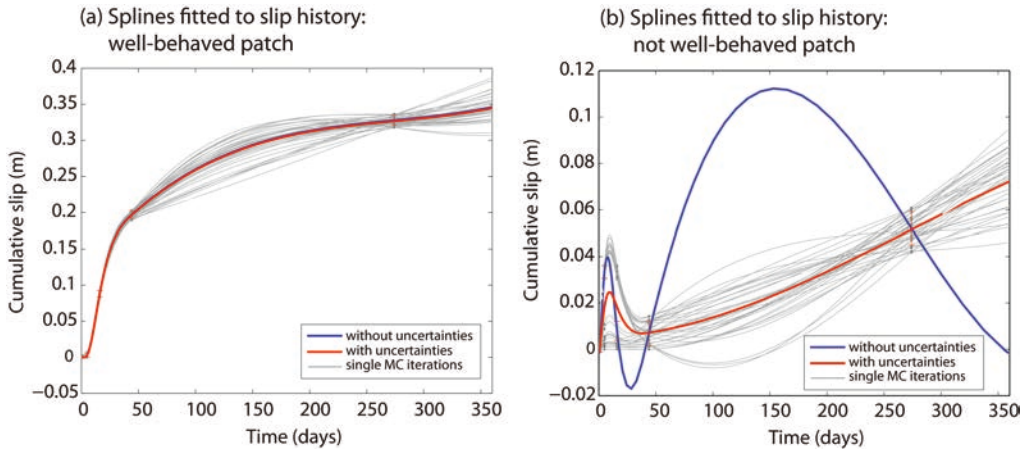

Figure 6.1: *Example of interpolation between afterslip snapshots at times* $t = [1, 5, 16, 44, 274]$ *days, on two patches. The slip models are for Parkfield, from Wang et al. [2012b]. Grey lines are a sample of the splines obtained from perturbing the value of slip; the red line is their average. The blue line is the spline obtained without considering uncertainties. (a) For a well-behaved slip history, the two methods give similar results; (b) in this case, an oscillatory slip history is obtained by fitting splines without considering uncertainties. Note the different y-axis: I find that patches with a larger total slip tend to be better behaved, since they have a monotonic slip history.*

6.2.2 Calculating seismicity evolution

Calculating seismicity evolution consists of solving the rate-and-state differential equation introduced in Chapter 2:

$$\begin{aligned} R(t,x) &= \frac{r_0(x)}{\gamma(t)\dot{\tau}_r} \\ d\gamma &= \frac{1}{A\sigma}\left[dt - \gamma dS\right] \end{aligned} \tag{6.1}$$

Seismic and aseismic stress changes are characterized by different forms of $S(t)$: while a stress step is a better approximation for static coseismic stress changes, aseismic processes are better described by continuous functions. Therefore, I proceed as follow:

1. At the time t of an earthquake, $\gamma_{(t_+)} = \gamma_{(t_-)} e^{\Delta S/A\sigma}$
2. Between earthquakes, the evolution of γ due to continuous stress changes is calculated as explained below.

Analytical solutions to equations 2.4 and 2.5 are known for few functional forms of $S(t)$, including a stress step followed by constant

stress and constant stressing rate. In order to model arbitrary stressing histories, the function $S(t)$ is discretized so that an analytical solution can be used within each time step: for example, by assuming step changes in the centre of each bin [*Dieterich et al.*, 2000; *Hainzl et al.*, 2010c]. In this work, I represent the function as a piecewise linear function, which I find to be a better approximation. Using the solution of Eq. 2.5 for linear constant $\dot{S}$ (Eq. 17 in *Dieterich* [1994]), the evolution of γ between time t and $t + \Delta t$ with a constant stressing rate $\dot{S} = \Delta S/\Delta t$ is found:

$$\gamma_{(t+\Delta t)} = \left(\gamma_{(t)} - \frac{\Delta t}{\Delta S}\right) e^{-\Delta S/A\sigma} + \frac{\Delta t}{\Delta S} \tag{6.2}$$

Similarly, the total number of events in between t and $t + \Delta t$ can be obtained by integrating Eq. 2.4:

$$N(t + \Delta t) = N(t) + \frac{r_0 \dot{S}}{\dot{S}_0} \left\{\Delta t + t_a \left[\log\left(\alpha e^{-\Delta t/t_a} + 1\right) - \log(\alpha + 1)\right]\right\} \tag{6.3}$$

where $\dot{S}$ is the stressing rate between t and $t + \Delta t$, $\dot{S}_0$ is the stressing rate in the previous time step and $\alpha = \dot{S}\gamma_{(t)} - 1$.

6.2.3 Time step size

The time evolution of afterslip is close to a power law decay, or a logarithmic function: in either case, the slope of $S(t)$ decreases with time. In order to capture the initial rapid evolution of stresses, and at the same time save computational resources, I choose to discretize the function using non-uniform time steps of the form:

$$t_i = t_{i-1} + K(t_{i-1} - t_{eq} + c)^p \tag{6.4}$$

which yields stress changes of equal size for afterslip following an Omori decay with parameters p and c, which are fixed to the values of p=0.6, c=0.001 days; t_{eq} is the time of the most recent mainshock followed by afterslip. It should be noted that the temporal evolution of afterslip is not constrained to be of this form: the equation simply refers to the separation of consecutive "snapshots", between which a linear evolution is assumed as described in section 6.2.2. Fig. 6.2a shows an example of the discretization of afterslip, the convergence to the analytical solution as $K \to 0$, and the increase in number of steps: the value of K is selected to achieve an accurate result while keeping the number of time steps, and hence the computational requirements, low.

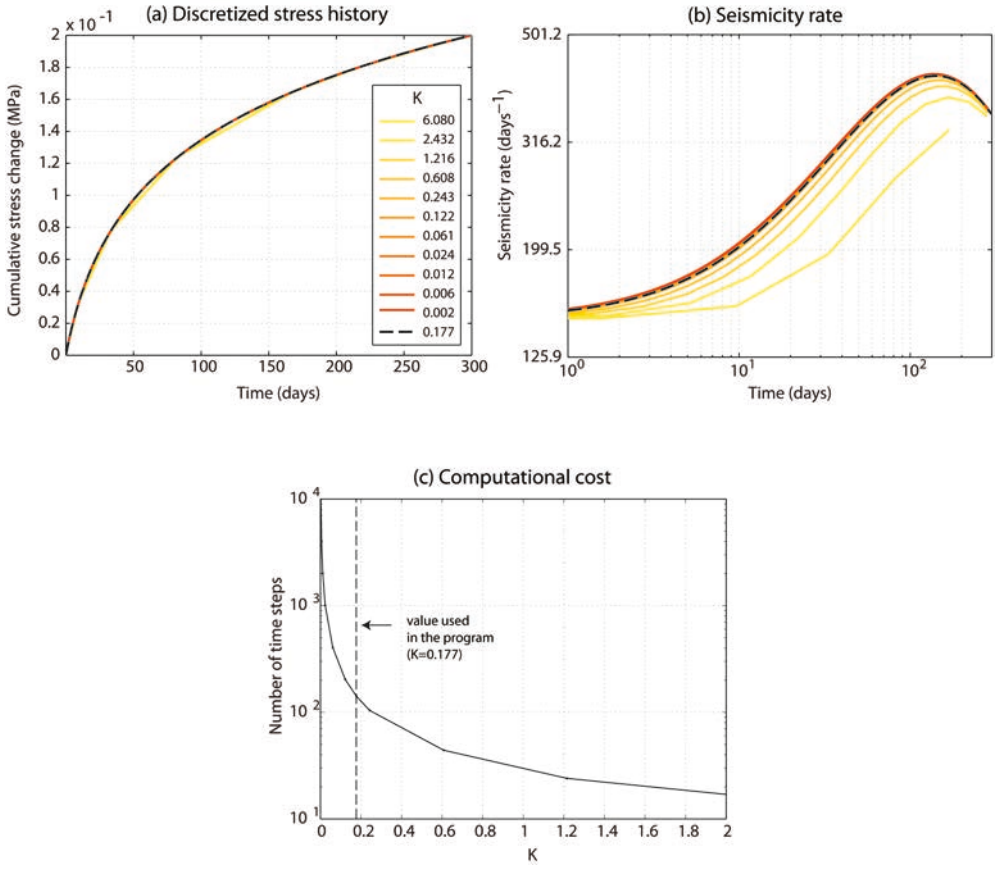

Figure 6.2: *(a): Discretization of the afterslip time function, according to Eq. 6.4. (b) Solution for seismicity rate calculated from Eq. 6.2, and various values of* K *in Eq. 6.4. (c) Tradeoff between K and the total number of steps. In (a) and (b), a coseismic stress step of* 0.5 *MPa is followed by logarithmic afterslip reaching* 0.2 *MPa at* $t = 300$ *days;* $A\sigma = 0.1$ *MPa,* $t_a = 100000$ *days, and the calculation period is* 300 *days. Black dashed lines refer to the value of* K *used in the code (*0.177*).*

6.3 Performance and Parallelization strategies

The current model implementation is significantly more complex than standard CRS models [*Hainzl et al.*, 2010c], implying a growth of computational costs. These aspects in particular lead to an increase in memory and CPU requirements:

- **Monte Carlo method.** The number of CPU operations scales approximately as $\mathcal{O}(n)$ with the number of iterations, which can be of the order of 100-1000 to obtain a reliable sample of the receiver faults provided in a catalogue for a given region;
- **Model discretization.** As explained in Chapter 4, the inclusion

of aftershocks as stress sources may require the choice of a finer grid to include smaller events. Moreover, the results of the CSEP experiment presented in Chapter 5 highlight the benefits of using an internally refined grid, despite the increase in the number of computations of the order of $10^2 - 10^3$;

- **Slip model resolution.** For stress calculations, the number of operations grows linearly with the number of patches in a slip model. While current published slip models usually do not exceed few thousand patches, this aspect may become a limitation when including slip at smaller scales (as done for example in Chapter 4);
- **Inclusion of more stress sources.** This aspect increases the time spent to calculate stresses and to evolve seismicity (Eq. 2.4, 2.5 in Chapter 2). However, I find that the computation time increases less significantly compared to the previous aspects (less than a factor of 2).

In what follows, I first describe how stresses from slip models are calculated in an efficient way; secondly, I describe two levels of parallelization: the lower level, consisting of parallelization for shared memory systems, implemented in OpenMP; and the second layer, which distributes the load across nodes of a distributed memory system, and is implemented in MPI. The calculations presented in the previous chapters have been carried out on a 6-cores Desktop PC with 12 GB of RAM, making use of the OpenMP parallelization. Currently, the code can be used on more powerful machines, allowing for a higher resolution, longer forecast periods and a larger number of iterations: the second layer of parallelization is aimed at this case.

6.3.1 Calculation of stresses from slip models

Since the Okada solutions in an elastic medium are linear with respect to source displacement, the total stress change at a single grid point induced by a set of rectangular sources with displacements $\mathbf{s}_k = (ss_k, sd_k)$ is a rank 2 tensor given by:

$$S_{ij} = A_{ij,k} ss_k + B_{ij,k} sd_k \tag{6.5}$$

with $i, j = 1, 2, 3$, and using the summation convention. $A_{ij,k}$, $B_{ij,k}$ are the Okada coefficients for slip on patch k, and ss_k and sd_k indicate the slip along strike and along dip. Since $S_{ij} = S_{ji}$, a more

compact representation of S_{ij} consists of a 6×1 vector, with the Okada coefficients forming a matrix of size $2N \times 6$, where N is the number of patches:

$$\begin{pmatrix} S_{xx} \\ S_{yy} \\ S_{xx} \\ S_{xy} \\ S_{xz} \\ S_{yz} \end{pmatrix} = \begin{pmatrix} A_{xx,1} & A_{xx,2} & \cdots & A_{xx,N} & B_{xx,1} & B_{xx,2} & \cdots & B_{xx,N} \\ A_{yy,1} & A_{yy,2} & \cdots & A_{yy,N} & B_{yy,1} & B_{yy,2} & \cdots & B_{yy,N} \\ \vdots & \vdots & \ddots & \vdots & \vdots & \vdots & \ddots & \vdots \\ A_{yz,1} & A_{yz,2} & \cdots & A_{yz,N} & B_{yz,1} & B_{yz,2} & \cdots & B_{yz,N} \end{pmatrix} \cdot \begin{pmatrix} ss_1 \\ \vdots \\ ss_N \\ sd_1 \\ \vdots \\ sd_N \end{pmatrix} \tag{6.6}$$

or using more compact notation $\mathbf{S} = \mathbf{G} \cdot \mathbf{s}$. The stress tensor $\mathbf{S}$ is then resolved on the receiver fault plane to calculate τ and σ.
The calculation of the Okada solutions grows fast with problem size: the number of calculations scales linearly with the number of slip model patches (which can be of the order of 10^3) and grid points (in the case studies of Chapter 3 and Chapter 4, up to $10^4 - 10^5$). A naive implementation in which the entire calculation is repeated at each Monte Carlo iteration would be prohibitive. Therefore I divide it into the following steps:

1. Calculation of the $\mathbf{G}$ for a given slip model geometry (functions `okadaCoeff.c`, `okadaCoeff_mpi.c`);
2. Calculation of the stress tensor $\mathbf{S}$ for a given slip model $\mathbf{s}$ (function `okadaCoeff2DCFS.c`);
3. Calculation of σ, τ for a given receiver plane, and calculation of ΔCFS (function `resolve_DCFS.c`);
4. Perturbation of ΔCFS to estimate uncertainties to finite grid size (function `smoothen_DCFS.c`).

Steps 1 and 2 are performed before the Monte Carlo iterations; step 3 is performed at each iteration if multiple receiver faults are used, or before the Monte Carlo iterations otherwise; step 4 is performed at each iteration if uncertainties from the finite grid size are considered.
The advantage of storing the matrix $\mathbf{G}$ in memory is that it can be reused for all slip models which share the same geometry. This is the case for afterslip, which is defined on the same fault plane as coseismic slip and may be represented by a large number of snapshots. As explained in

Benchmark name	OMP	MPI 1	MPI 2
Monte Carlo iterations	100	5000	50
Calculation grid points	52338	112728	52338
Slip model patches	1696	1657	496
Seismic stress sources	3	18	3
Events for LL calculation	4037	329	4037
Grid Search: time period	10 d	10 d	10 d
Grid Search: no. of $A\sigma$, t_a values	9	9	25
Forecast: time period	1 yr	0.5 yr	1 yr
Inclusion of afterslip	no	yes	no

Table 6.1: *Summary of the input parameters used in the performance benchmarks.*

section 3.2, the user may also supply a set of alternative coseismic slip models: if these have the same geometry, the matrix **G** will not be re-calculated. This method allows, for example, to include a large set of models obtained from Bayesian inversion on a fixed geometry, which give a measure of the uncertainties in the slip distribution (as in Chapter 3).

6.3.2 Empirical analysis of parallel performance

We[1] designed three different benchmarks in order to evaluate different performance aspects and/or simulation scenarios. The datasets used are from the 2011 M_w9.0 Tohoku earthquake, which due to its magnitude can be considered as an upper limit of the domain size and hence computational requirements. We present specification of the test bed, describe benchmarks and present results.

Cluster Specifications

Performance benchmarking was carried out at the Future of Service Oriented Computing (FutureSOC) Lab at the Hasso Plattner Institute in Potsdam. The cluster at the FutureSOC Lab consists of 25 nodes, each equipped with 4 Intel Xeon E7-4870 processors. Each processor can run up to 20 threads/ranks in parallel, making it 80 across each node, and a maximum of 2000 across the entire cluster. Each node is also equipped

1 I use the plural form for the aspects of the work to which my co-author (Fahad Khalid) contributed significantly.

with 1 TB of RAM, and 4 solid state hard disks with a capacity of 450 GB each. There are two 10 Gigabit Network Interface Cards (NICs) per node; one dedicated for communication with the network storage system, and the other dedicated for inter-node communication, such as message passing. The code was compiled with GCC 4.7.3 and OpenMPI 1.7.4. The operating system running on the cluster was SUSE Linux Enterprise Server 11.

6.3.3 Parallelization in OpenMP

OpenMP concepts

OpenMP allows parallel execution of threads on shared memory systems, such as single machines with multiple processors or cores. It implements multithreading, which consists of creating several threads to be executed by different processors; threads are forked and joined at run time, and they may only exist for a fraction of the program execution. Since all threads share the same memory, there is no significant increase in memory usage when running the code in parallel.

OpenMP implementation in CRS

I implemented parallelization for shared memory systems in the following functions:

- **Functions for calculating stress fields from slip models**: these are the functions described in section 6.3.1. The parallelization is performed over the grid points.
- **Function `rate_state_evolution.c`**: this function is responsible for calculating the evolution of seismicity according to Eq. 2.4 and 2.5. Also in this case, the parallelization is over grid points.
- **File input**: when reading the earthquake catalogue, the location of each earthquake is smoothed across a subset of grid points to account for location uncertainty, as described in Chapter 2. This operation is also done in parallel, by processing multiple earthquakes simultaneously.

OMP Benchmark

In order to test how the code scales with number of OpenMP threads, we run a benchmark test with a domain size which is a modified version of the models presented in Chapter 3 and Chapter 4, for the Tohoku

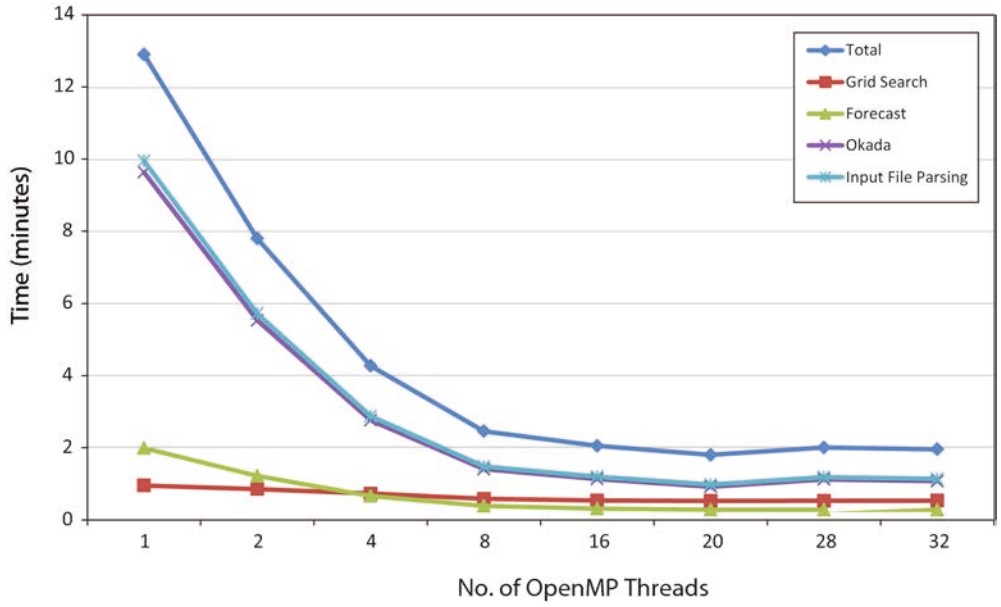

Figure 6.3: *Run times for the OMP benchmark (summarized in Table 6.1) vs. number of OpenMP threads.*

earthquake (OMP benchmark in Table 6.1). While the actual execution time may vary across different machines, the scaling with number of threads gives a measure of the benefit gained by running the program in parallel. Fig. 6.3 shows that an increase in speed up to a factor of $5-6$, when the number of threads is close to 10; there is no additional speedup when more threads are used, due to the parallelization overhead and to the contribution from non-parallel portions of the code. In this example, most of performance improvement comes from parallelizing the calculation of Okada coefficients and the smoothing of earthquakes over grid points. The calculation of perturbed stress fields and seismicity evolution (performed within "Grid Search" and "Forecast") takes overall a small fraction of time. This result should not be taken as general, since the time spent within each function varies largely depending on model settings: for example, using a slip model with fewer patches or larger number of Monte Carlo iterations will increase the relative weight of "Grid Search" and "Forecast". In terms of speedup, we find that in this case the execution time of "Forecast" decreases by a factor of 5 when using 8 threads, while the speedup for "Grid Search" is only 1.7. This may be due to using a short time period for the grid search (10 days), which causes a relatively larger parallelization overhead compared to "Forecast".

6.3.4 Parallelization in MPI

MPI Concepts

The Message Passing Interface (MPI) library is used for a distributed-memory parallel implementation, intended primarily for cluster systems. An MPI program executes as a combination of independent processes (ranks). Each rank has a private copy of all program data structures – scalars, vectors, matrices, tensors, etc., – and communicates with other ranks via message passing; one rank cannot directly access another rank's memory; this is because different MPI ranks generally run on different machines in a cluster. Therefore, the memory consumption of CRS-MPI increases with the addition of each MPI rank. Please note that it is possible to utilize more than one OpenMP threads within one MPI rank.

CRS MPI

We implement parallelization in MPI parallelization in the following parts of the simulation:

- **Reading input files**: Input file reading is implemented as a serial process, i.e., only one rank can read files. Therefore, root reads all input files, populates corresponding data structures, and broadcasts these data structure to all other ranks. Once all broadcast operations are complete, each rank has a copy of input data and can proceed with the simulation.

- **Okada Computation**: The calculation of Okada solutions comprises an algorithm with three levels of nesting: 1) Fault, 2) Patch 3) Grid points. The parallelization strategy employed in the MPI version for CRS decomposes the tensor by dividing the total number of patches among all available ranks. Each rank performs calculations for its share of patches. Once all ranks have finished computations for their respective share of patches, each rank shares its local results with all other ranks. The end result of this reduction operation is that each rank ends up with a tensor with all results.

- **Grid Search**: Grid search parallelization is accomplished by dividing the total number of Monte Carlo iterations among all available MPI ranks. Therefore, each rank only computes a small portion of iterations. Once all ranks are done, results are combined using a reduction operation similar to the one used for Okada computations.

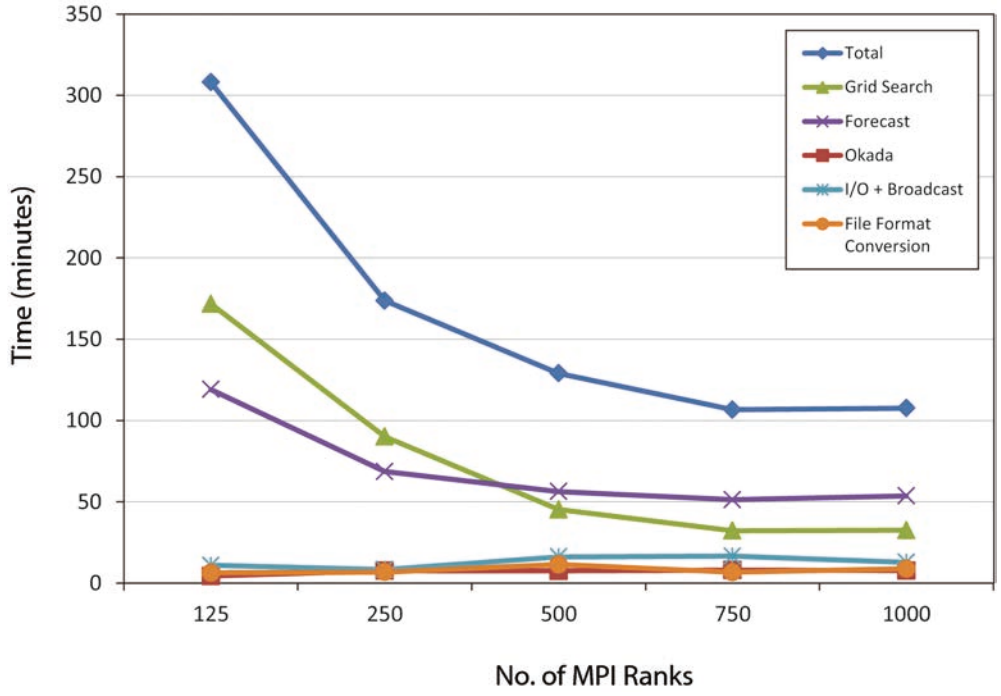

Figure 6.4: *Run times for MPI benchmark 1 (summarized in Table 6.1) vs. number of MPI ranks.*

- **Forecast**: Forecast computation utilizes the same parallelization strategy as grid search. The loop iterations are divided among MPI ranks, followed by a reduction operation that combines all local results.
- **File Format Conversion**: Within the forecast algorithm, all MPI ranks write output values to files. The file format used by the MPI parallel file I/O routines is binary. Since the binary format is not human readable, the program converts all binary output files to ASCII at the end of the simulation.

MPI Benchmark 1

We designed a benchmark to evaluate overall simulation performance with MPI parallelization (presented in Table 6.1). Fig. 6.4 shows benchmark results with 125, 250, 500, 750, and 1000 ranks. Since each node in the cluster can execute up to 80 threads, we placed multiple MPI ranks per node. We observed that, in terms of the number of ranks, CRS-MPI scales well up to 750 ranks. For more than 750 ranks, the parallelization overhead, i.e., inter-rank communication during reduction operations, overshadows any performance gains. Grid search

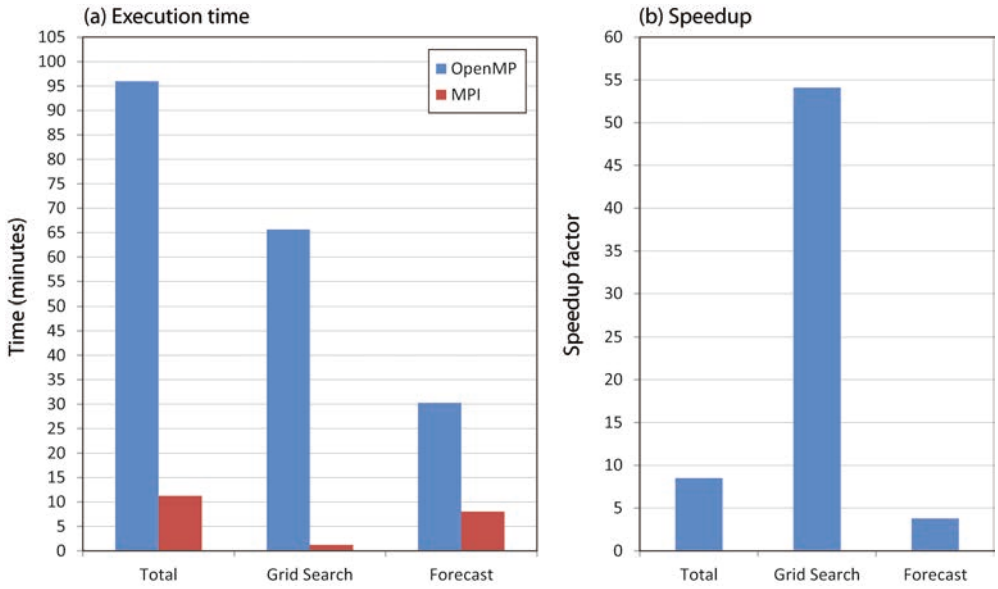

Figure 6.5: *Run times for MPI benchmark 2. The OpenMP version is executed with 20 threads; the MPI version uses 50 MPI ranks over 5 nodes. The speedup is the ratio between execution time in the MPI and the OpenMP versions.*

gains the most from this parallelization strategy. This is due to the fact that the grid search algorithm has a more suitable balance of computational intensity per iteration and computational intensity across all Monte Carlo iterations. Moreover, there are fewer grid search parameters used for reduction, and there are no parallel file I/O operations. Forecast on the other hand has a larger number of reduction parameters, and makes extensive use of MPI parallel file I/O routines. Also, the forecast algorithm favours parallelization within a single iteration. The contrast between grid search and forecast can be seen on the plot in Fig. 6.4.
We further observed that the performance impact of input-parameter broadcast and file format conversion is negligible, considering the total simulation time. Also, Okada computations do not contribute significantly to the overall computation time. This is due to the fact that this particular simulation utilizes a small number of patches.

MPI Benchmark 2

Not all users of CRS-MPI might have access to a cluster as powerful as the FutureSOC cluster. This benchmark was designed to evaluate simulation performance with a smaller number MPI ranks, distributed over a smaller number of nodes. Also, since the primary source of performance gain for CRS-MPI is parallelization of the Monte Carlo iterations,

this benchmark used a configuration that makes the Monte Carlo iterations the most compute intensive part of the simulation. Configuration parameters are presented in Table 6.1.
The benchmark was executed with 50 MPI ranks distributed across 5 nodes; 10 ranks per node. Fig. 6.5 compares simulation performance for this benchmark, with the same simulation configuration executed with the OpenMP-only version of CRS executed with 20 threads. It can be concluded that even with a small number of MPI ranks distributed over a small number of nodes, the performance gain is significant; a large number of iterations can be executed in a significantly shorter period of time.

6.4 Discussion and Conclusions concerning the computational aspects

The performance improvement gained by OpenMP parallelization scales well up to 8 threads, with an overall speedup of a factor of $5-6$. This behaviour makes it particularly suitable for execution on standard personal desktop and laptop computers with more than a single core. On such machines, memory may be the main restriction to the size of tractable problems: for example, I find that the OMP benchmark requires approximately 4.5 GB.
The results from the MPI Benchmark 2 indicate that, even with a relatively small number of Monte Carlo iterations (N), a speedup of $8-9$ can be achieved by the MPI parallelization when 50 ranks are used, as may be possible if a small-medium size cluster is available. Finally, the MPI benchmark 1 shows that the code scales well up to 750 MPI ranks. With a number of Monte Carlo iterations of the order of 10^4, we find a speedup of $25-65$ when the number of MPI ranks is of the order of hundreds. If such computational resources are available, it is therefore possible to run problems of a significantly larger size than those presented in Chapter 3 and Chapter 4.

6.4.1 Potential improvements

The current MPI based parallelization of Okada computation is not very effective, because it requires a large amount of memory to be allocated per rank. This limits the number of patches for which the parallelization can be used. However, since MPI parallelization is meant for large

problem sizes, we do not see any significant performance gain over the OMP version. We intend to fix this problem in a future release.

All benchmarks presented here utilize only 2 OMP threads per MPI rank. In principle, it is possible to utilize a larger number of OMP threads per MPI rank. It is likely that different configurations of OMP threads per MPI rank might favour performance improvements in different parts of the simulation. We intend to experiment with these configurations in the future.

In terms of domain size, the use of a uniform grid is not ideal, since different resolutions may be required in different regions. The current internal grid refinement algorithm could be improved by selecting different sub-grid cell size depending on the location of stress sources.

7

CONCLUSIONS AND FUTURE DIRECTIONS

In this thesis I have studied different aspects of physics-based aftershock models, in an attempt to implement a more realistic description of the physical processes involved in earthquake triggering.

Chapter 3 is a sensitivity study analysing various sources of uncertainties, in which I introduced methods to propagate uncertainties through the model. The main findings of this study are the following:

- The geometrical complexity of a fault system has a first-order impact on stress heterogeneity;
- Differences between published coseismic slip models also generate large stress uncertainties;
- The performance of the model improves dramatically when aleatoric uncertainties are included by averaging over Monte Carlo iterations;
- Ensemble models obtained from different input slip models are an effective way to include epistemic uncertainties, and they perform better.

I studied the role of stresses induced by afterslip and by previous aftershocks during a sequence in Chapter 4. The main conclusions of the study are the following:

- Modelling secondary triggering systematically improves the maximum log-likelihood fit;
- Afterslip plays a second order role, and it does not always improves model performance. In the near field, large slip model uncertainties make it challenging to draw definitive conclusions on the extent to which afterslip triggers aftershocks;

- Deep afterslip following large subduction earthquakes significantly contributes to triggering seismicity on shallow crustal faults, both due to its location and its temporal evolution.

Since the start of this work, Operational Earthquake Forecasting has been at the centre of important practical developments as well as a lively debate. In New Zealand, time-dependent seismicity models, including some of the aftershock clustering models listed in Chapter 5, have been used for planning recovery operations following the Darfield sequence [*Gerstenberger et al.*, 2014]; attention has been paid to the population response to the aftershock forecasts disseminated during the sequence, which was found to be overall positive [*Wein and Becker*, 2013]. The first version of an OEF system for Italy has been implemented [*Marzocchi et al.*, 2014], and it will soon be tested in selected areas.
At the same time, concerns on the usefulness of OEF have been raised [*Wang and Rogers*, 2014; *Kossobokov et al.*, 2015]. Among other criticisms, the authors mentioned the large uncertainties in the earth system generating earthquakes. Indeed, I believe that large differences in our knowledge of the underlying system exist between the fields of earthquake and weather forecasting (the context in which the term "Operational Forecasting" was first introduced). One outcome of this thesis is a deeper understanding of some of the sources of these uncertainty, and the development of methods to treat them within CRS models (Chapter 3). In terms of future developments, I have identified the following aspects as key for producing better physical models of seismic sequences:

- **Knowledge of the regional fault system.** A detailed description of the existing fault planes would allow a more reliable calculation of stress changes capable to trigger aftershocks; moreover, information on fault location may be included in the model to relax the assumption of a uniform background rate, by implementing spatially variable background seismicity models based on the fault network.

- **Reliable slip models.** Differences between slip models are a large source of epistemic uncertainty. Since the differences between forecasts are more pronounced in the near field, this issue may not be a priority in a OEF context, since aftershocks on the fault plane are expected and those in the far field are more important to forecast. On the other hand, better coseismic and postseismic slip models may allow to constrain the role of aseismic slip in earthquake triggering and establish whether more efforts to include this aspect in the models should be made. Given

the proposed intensified monitoring of the subduction interface, including the deployment of Ocean Bottom Seismometers and sea floor geodetic instruments [*Newman*, 2011], this issue may be worth further investigation in the future.

Other questions remain open in terms of the physical processes occurring during aftershock sequences, and in particular the relative role of small and large aftershocks in secondary triggering, and the contribution from other aseismic processes such poroelastic effects and dynamic triggering.

Based on the preliminary results presented in Chapter 5, the improvements to CRS models presented in this thesis make them competitive in comparison to statistical models, which are currently predominant in the OEF arena. In the future, further validation in CSEP testing centres should be carried out to assess their predictive power and their potential use in an operational context: by improving the efficiency of the software and making it open-source, as described in Chapter 6, I hope to facilitate efforts in this direction.

BIBLIOGRAPHY

Asano, Y., T. Saito, Y. Ito, K. Shiomi, and H. Hirose, Spatial distribution and focal mechanisms of aftershocks of the 2011 off the Pacific coast of Tohoku Earthquake, *Earth Plan. Space*, *63*, 669–673, doi: 10.5047/eps.2011.06.016, 2011.

Bach, C., and S. Hainzl, Improving empirical aftershock modeling based on additional source information, *J. Geophys Res.*, *117*, 1–12, doi: 10.1029/2011JB008901, 2012.

Barbot, S., Y. Fialko, and Y. Bock, Postseismic deformation due to the Mw 6.0 2004 Parkfield earthquake: Stress-driven creep on a fault with spatially variable rate-and-state friction parameters, *J. Geophys Res.*, *114*, 1–26, doi: 10.1029/2008JB005748, 2009.

Beavan, J., M. Motagh, E. J. Fielding, N. Donnelly, and D. Collett, Fault slip models of the 2010-2011 Canterbury, New Zealand, earthquakes from geodetic data and observations of postseismic ground deformation, *New Zealand J. of Geology and Geophysics*, *55*(3), 37–41, doi: 10.1080/00288306.2012.697472, 2012.

Bedford, J., et al., A high-resolution, time-variable afterslip model for the 2010 Maule Mw=8.8, Chile megathrust earthquake, *Earth and Plan. Sci. Lett.*, *383*, 26–36, doi: 10.1016/j.epsl.2013.09.020, 2013.

Belardinelli, M. E., Earthquake triggering by static and dynamic stress changes, *J. Geophys Res.*, *108*, 1–16, doi: 10.1029/2002JB001779, 2003.

Benioff, H., Earthquakes and rock creep, *Bull. Seism. Soc. Am.*, 1951.

Beresnev, I. A., Uncertainties in Finite-Fault Slip Inversions: To What Extent to Believe? (A Critical Review), *Bull. Seism. Soc. Am.*, *93*(6), 2445–2458, 2003.

Bhloscaidh, M. N., J. McCloskey, and C. J. Bean, Response of the San Jacinto Fault Zone to static stress changes from the 1992 Landers earthquake, *J. Geophys Res.*, *119*, 8914–8935, doi: 10.1002/2014JB011164, 2014.

Cattania, C., and F. Khalid, A parallel code to calculate seismicity evolution induced by time dependent, heterogeneous Coulomb stress changes, *in preparation for submission to Computers and Geosciences*.

Cattania, C., S. Hainzl, L. Wang, F. Roth, and B. Enescu, Propagation of Coulomb stress uncertainties in physics-based aftershock models, *J. Geophys Res.*, *119*, 7846–7864, doi: 10.1002/2014JB011183, 2014.

Cattania, C., S. Hainzl, L. Wang, B. Enescu, and F. Roth, Aftershock triggering by postseismic stresses: a study based on Coulomb-Rate-and-State models, *J. Geophys Res.*, *in press*, doi: 10.1002/2014JB011500, 2015.

Causse, M., F. Cotton, and P. M. Mai, Constraining the roughness degree of slip heterogeneity, *J. Geophys Res.*, *115*, 1–14, doi: 10.1029/2009JB006747, 2010.

Chen, K. H., R. Bürgmann, and R. M. M. Nadeau, Do earthquakes talk to each other? Triggering and interaction of repeating sequences at Parkfield, *J. Geophys Res.*, *118*, 1–18, doi: 10.1029/2012JB009486, 2013.

Christophersen, A., S. Hainzl, M. C. Gerstenberger, D. A. Rhoades, and E. G. C. Smith, The Canterbury sequence in the context of global earthquake statistics, *GNS Science Consultancy Report*, (196), 2013.

Cocco, M., and J. R. Rice, Pore pressure and poroelasticity effects in Coulomb stress analysis of earthquake interactions, *J. Geophys Res.*, *107*(0), doi: 10.1029/2000JB000138, 2002.

Cocco, M., S. Hainzl, F. Catalli, B. Enescu, A. M. Lombardi, and J. Woessner, Sensitivity study of forecasted aftershock seismicity based on Coulomb stress calculation and rate-and-state-dependent frictional response, *J. Geophys Res.*, *115*, 1–15, doi: 10.1029/2009JB006838, 2010.

Das, S., and C. Henry, Spatial relation between main earthquake slip and its aftershock distribution, *Rev. of Geophys.*, *41*(3), 1013–2003, doi: 10.1029/2002RG000119, 2003.

Das, S., and C. H. Scholz, Off-fault aftershock clusters caused by shear stress increase, *Bull. Seism. Soc. Am.1*, *71*(5), 1669–1675, 1981.

Diao, F., X. Xiong, R. Wang, Y. Zheng, T. R. Walter, H. Weng, and J. Li, Overlapping post-seismic deformation processes: afterslip and viscoelastic relaxation following the 2011 Mw 9.0 Tohoku (Japan) earthquake, *Geophys. J. Int.*, *196*(1), 218–229, doi: 10.1093/gji/ggt376, 2014.

Dieterich, J., A constitutive law for rate of earthquake its application to earthquake clustering, *J. Geophys Res.*, *99*, 2601–2618, 1994.

Dieterich, J., A. Cayol, and P. Okubo, The use of earthquake rate changes as a stress meter at Kilauea volcano, *Nature*, *408*, 457–460, 2000.

Dieterich, J. H., Modeling of Rock Friction Experimental Results and Constitutive Equations, *Journal Geophys. Res.*, *84*(9), 2161–2168, 1979.

Dieterich, J. H., Constitutive properties of faults with simulated gauge, in *Mechanical Behavior of Crystal Rocks*, edited by N. L. Carter, M. Friedman, J. M. Logan, and D. W. Stearns, pp. 103–120, Americal Geophysical Union, 1981.

Doser, D. I., and R. Robinson, Modeling Stress Changes Induced by Earthquakes in the Southern Marlborough Region, South Island, New Zealand, *Bull. Seism. Soc. Am.*, *92*(8), 3229–3238, 2002.

Enescu, B., S. Aoi, S. Toda, W. Suzuki, K. Obara, K. Shiomi, and T. Takeda, Stress perturbations and seismic response associated with the 2011 M9.0 Tohoku-oki earthquake in and around the Tokai seismic gap, central Japan, *Geophys. Res. Lett.*, *39*, 10–15, doi: 10.1029/2012GL051839, 2012.

Felzer, K. R., and E. E. Brodsky, Decay of aftershock density with distance indicates triggering by dynamic stress, *Nature*, *441*, 1–4, doi: 10.1038/nature04799, 2006.

Freed, A. M., Earthquake triggering by static, dynamic, and postseismic stress transfer, *Ann. Rev. Earth Planet. Sci.*, *33*, 335–367, doi: 10.1146/annurev.earth.33.092203.122505, 2005.

Freed, A. M., and J. Lin, Delayed triggering of the 1999 Hector Mine earthquake by viscoelastic stress transfer, *Nature*, *411*, 1999–2002, 2001.

Gardner, J. K., and L. Knopoff, Is the sequence of earthquakes in southern California, with aftershocks removed, Poissonian?, *Bull. Seism. Soc. Am.*, *64*(5), 1363–1367, 1974.

Gerstenberger, M., G. Mcverry, M.EERI, D. A. Rhoades, and M. Stirling, Seismic Hazard Modeling for the Recovery of Christchurch, *Earthquake Spectra*, *30*(1), 17–29, doi: 10.1193/021913EQS037M, 2014.

Gomberg, J., and B. Sherrod, Crustal earthquake triggering by modern great earthquakes on subduction zone thrusts, *J. Geophys Res.*, *119*, 1235–1250, doi: 10.1002/2012JB009826, 2014.

Gualandi, A., E. Serpelloni, and M. E. Belardinelli, Space-time evolution of crustal deformation related to the Mw 6.3, 2009 L'Aquila earthquake (central Italy) from principal component analysis inversion of GPS position time-series, *Geophys. J. Int.*, *197*(1), 174–191, doi: 10.1093/gji/ggt522, 2014.

Hainzl, S., B. Enescu, M. Cocco, J. Woessner, F. Catalli, R. Wang, and F. Roth, Aftershock modeling based on uncertain stress calculations, *J. Geophys Res.*, *114*, 1–12, doi: 10.1029/2008JB006011, 2009.

Hainzl, S., G. B. Brietzke, and G. Zöller, Quantitative earthquake forecasts resulting from static stress triggering, *J. Geophys Res.*, *115*, 1–9, doi: 10.1029/2010JB007473, 2010a.

Hainzl, S., S. Steacy, and D. Marsan, Seismicity Seismicity Models Based on Coulomb Stress Calculations, *Community Online Resource for Statistical Seismicity Analysis*, (Available at http://www.corssa.org), 1–25, doi: 10.5078/corssa-32035809, 2010b.

Hainzl, S., G. Zöller, and R. Wang, Impact of the receiver fault distribution on aftershock activity, *J. Geophys Res.*, *115*, 1–12, doi: 10.1029/2008JB006224, 2010c.

Hainzl, S., Y. Ben-Zion, **C. Cattania**, and J. Wassermann, Testing atmospheric and tidal earthquake triggering at Mt. Hochstaufen, Germany, *Journal Geophys. Res.*, *118*(\), 5442–5452, doi: 10.1002/jgrb.50387, 2013.

Hainzl, S., J. Moradpour, and J. Davidsen, Static stress triggering explains the empirical aftershock distance decay, *Geophys. Res. Lett.*, *41*, 8818–8824, doi: 10.1002/2014GL061975.1., 2014.

Hardebeck, J. L., Homogeneity of Small-Scale Earthquake Faulting, Stress, and Fault Strength, *Bull. Seism. Soc. Am.*, *96*(5), 1675–1688, doi: 10.1785/0120050257, 2006.

Hardebeck, J. L., J. J. Nazareth, and E. Hauksson, The static stress change triggering model: Constraints from two southern California aftershock sequences, *J. Geophys Res.*, *103*(B10), 24,427–24,437, 1998.

Hartzell, S., P. Liu, C. Mendoza, C. Ji, and K. M. Larson, Stability and Uncertainty of Finite-Fault Slip Inversions: Application to the 2004 Parkfield, California, Earthquake, *Bull. Seism. Soc. Am.*, *97*(6), 1911–1934, doi: 10.1785/0120070080, 2007.

Hasegawa, A., K. Yoshida, and T. Okada, Nearly complete stress drop in the 2011 Mw 9.0 off the Pacific coast of Tohoku Earthquake, *Earth, Plan. Space*, *63*, 703–707, doi: 10.5047/eps.2011.06.007, 2011.

Helmstetter, A., and B. E. Shaw, Relation between stress heterogeneity and aftershock rate in the rate-and-state model, *J. Geophys Res.*, *111*, 1–12, doi: 10.1029/2005JB004077, 2006.

Helmstetter, A., and B. E. Shaw, Afterslip and aftershocks in the rate-and-state friction law, *J. Geophys Res.*, *114*, doi: 10.1029/2007JB005077, 2009.

Helmstetter, A., and M. J. Werner, Adaptive Smoothing of Seismicity in Time, Space, and Magnitude for Time-Dependent Earthquake Forecasts for California, *Bull. Seism. Soc. Am.*, *104*(2), 809–822, doi: 10.1785/0120130105, 2014.

Helmstetter, A., Y. Y. Kagan, and D. D. Jackson, High-resolution Time-independent Grid-based Forecast for M$\geqslant$5 Earthquakes in California, *Seism. Res. Lett.*, *78*(1), 78–86, doi: 10.1785/gssrl.78.1.78, 2007.

Holden, C., J. Beavan, B. Fry, M. Reyners, J. Ristau, R. V. Dissen, P. Villamor, and M. Quigley, Preliminary source model of the M w 7.1 Darfield earthquake from geological, geodetic and seismic data, *Proceedings of the Ninth Pacific Conference on Earthquake Engineering Building an Earthquake-Resilient Society*, *164*, 1–7, 2011.

Hough, S. E., *Predicting the Unpredictable: The Tumultuous Science of Earthquake Prediction*, Princeton University Press, 2009.

Hsu, Y., P. Segall, S. Yu, L. Kuo, and C. A. Williams, Temporal and spatial variations of post-seismic deformation following the 1999 Chi-Chi, Taiwan earthquake, *Geophys. J. Int.*, *169*, 367–379, doi: 10.1111/j.1365-246X.2006.03310.x, 2007.

Hyndman, R. D., M. Yamano, and D. A. Oleskevich, The seismogenic zone of subduction thrust faults, *The Island Arc*, *6*, 244–260, 1997.

Imanishi, K., R. Ando, and Y. Kuwahara, Unusual shallow normal-faulting earthquake sequence in compressional northeast Japan activated after the 2011 off the Pacific coast of Tohoku earthquake, *Geophys. J. Int.*, *39*, doi: 10.1029/2012GL051491, 2012.

Johnson, K. M., R. Bu, and K. Larson, Frictional Properties on the San Andreas Fault near Parkfield, California, Inferred from Models of Afterslip following the 2004 Earthquake, *Bull. Seism. Soc. Am.*, *96*(4), 321–338, doi: 10.1785/0120050808, 2006.

Jordan, T. H., et al., Operational Earthquake Forecasting: State of Knowledge and Guidelines for Utilization, *Ann. of Geophys.*, *54*(4), 315–391, doi: 10.4401/ag-5350, 2011.

Kagan, Y. Y., Earthquakes: Models, Statistics, Testable Forecasts, in *Earthquakes: Models, Statistics, Testable Forecasts*, chap. 11, pp. 229–252, 2014.

Kato, A., S. Sakai, and K. Obara, A normal-faulting seismic sequence triggered by the 2011 off the Pacific coast of Tohoku Earthquake: Wholesale stress regime changes in the upper plate, *Earth, Plan. Space*, *63*, 745–748, doi: 10.5047/eps.2011.06.014, 2011.

Kato, A., K. Obara, T. Igarashi, H. Tsuruoka, S. Nakagawa, and N. Hirata, Propagation of Slow Slip Leading Up to the 2011 Mw9.0 Tohoku-Oki Earthquake, *Science*, *335*, 705–709, doi: 10.1126/science.1215141, 2012.

Kieling, K., R. Wang, and S. Hainzl, Broadband Ground-Motion Simulation Using Energy-Constrained Rise-Time Scaling, *Bull. Seism. Soc. Am.*, *104*(6), 2683–2697, doi: 10.1785/0120140063, 2014.

King, C. P., S. Stein, and J. Lin, Static Stress Changes and the Triggering of Earthquakes, *Bull. Seism. Soc. Am.*, *84*(3), 935–953, 1994.

Kossobokov, V. G., A. Peresan, and G. F. Panza, On Operational Earthquake Forecast and Prediction Problems, *Seism. Res. Lett.*, *86*(2), 287–290, doi: 10.1785/0220140202, 2015.

Langbein, J., J. R. Murray, and H. A. Snyder, Coseismic and Initial Postseismic Deformation from the 2004 Parkfield, California, Earthquake, Observed by Global Positioning System, Electronic Distance Meter, Creepmeters, and Borehole Strainmeters, *Bull. Seism. Soc. Am.*, *96*(4), 304–320, doi: 10.1785/0120050823, 2006.

Lange, D., et al., Aftershock seismicity of the 27 February 2010 Mw 8.8 Maule earthquake rupture zone, *Earth and Plan. Sci. Lett.*, *317-318*, 413–425, doi: 10.1016/j.epsl.2011.11.034, 2012.

Lay, T., and H. Kanamori, An asperity model of large earthquake sequences, *Earthquake Prediction: An International Review*, *4*, 1981.

Lengliné, O., and D. Marsan, Inferring the coseismic and postseismic stress changes caused by the 2004 Mw=6 Parkfield earthquake from variations of recurrence times of microearthquakes, *J. Geophys Res.*, *114*, B10,303, doi: 10.1029/2008JB006118, 2009.

Lin, J., and R. S. Stein, Stress triggering in thrust and subduction earthquakes and stress interaction between the southern San Andreas and nearby thrust and strike-slip faults, *J. Geophys Res.*, *109*, 1–19, doi: 10.1029/2003JB002607, 2004.

Linker, M. F., and J. H. Dieterich, Effects of variable normal stress on rock friction: Observations and constitutive equations, *J. Geophys Res.*, *97*(92), 4923–4940, 1992.

Mai, P. M., and G. C. Beroza, A spatial random field model to characterize complexity in earthquake slip, *J. Geophys Res.*, *107*, 2308, 2000.

Main, I., Is the reliable prediction of individual earthquakes a realistic scientific goal?, *Nature debates*, (http://www.nature.com/nature/debates/earthquake/equake_frameset.html), 1999.

Mallman, E. P., and T. Parsons, A global search for stress shadows, *J. Geophys Res.*, *113*, 1–16, doi: 10.1029/2007JB005336, 2008.

Marone, C., C. H. Scholz, and R. Bilham, On the Mechanics of Earthquake Afterslip, *J. Geophys Res.*, *96*(91), 8441–8452, 1991.

Marsan, D., Triggering of seismicity at short timescales following Californian earthquakes, *J. Geophys Res.*, *108*, 1–14, doi: 10.1029/2002JB001946, 2003.

Marsan, D., The role of small earthquakes in redistributing crustal elastic stress, *Geophys. J. Int.*, *163*, 141–151, doi: 10.1111/j.1365-246X.2005.02700.x, 2005.

Marsan, D., Can coseismic stress variability suppress seismicity shadows? Insights from a rate-and-state friction model, *J. Geophys Res.*, *111*, 1–11, doi: 10.1029/2005JB004060, 2006.

Marzocchi, W., J. D. Zechar, and T. H. Jordan, Bayesian Forecast Evaluation and Ensemble Earthquake Forecasting, *Bull. Seism. Soc. Am.*, *102*(6), 2574–2584, doi: 10.1785/0120110327, 2012.

Marzocchi, W., A. M. Lombardi, and E. Casarotti, The Establishment of an Operational Earthquake Forecasting System in Italy, *Seism. Res. Lett.*, *85*(5), 961–696, doi: 10.1785/0220130219, 2014.

Mccloskey, J., S. S. Nalbant, and S. Steacy, Earthquake risk from co-seismic stress, *Nature*, *434*, 291, doi: 10.1038/434291a, 2005.

McGuire, J. J., M. S. Boettcher, and T. H. Jordan, Foreshock sequences and short-term earthquake predictability on East Pacific Rise transform faults, *Nature*, *3*, 457–462, doi: 10.1038/nature03377, 2005.

Meier, M., M. J. Werner, J. Woessner, and S. Wiemer, A search for evidence of secondary static stress triggering during the 1992 Mw7.3 Landers, California,

earthquake sequence, *J. Geophys Res.*, pp. 3354–3370, doi: 10.1002/2013JB010385. Received, 2014.

Minson, S. E., M. Simons, and J. L. Beck, Bayesian inversion for finite fault earthquake source models I–theory and algorithm, *Geophys. J. Int.*, *194*(3), 1701–1726, doi: 10.1093/gji/ggt180, 2013.

Nalbant, S. S., J. Mccloskey, S. Steacy, and A. A. Barka, Stress accumulation and increased seismic risk in eastern Turkey, *Earth and Plan. Sci. Lett.*, *195*, 291–298, 2002.

Newman, A. V., Hidden depths, *Nature*, *474*, 441, 2011.

Nostro, C., L. Chiaraluce, M. Cocco, D. Baumont, and O. Scotti, Coulomb stress changes caused by repeated normal faulting earthquakes during the 1997 Umbria-Marche (central Italy) seismic sequence, *Journal Geophys. Res.*, *110*, 1–19, doi: 10.1029/2004JB003386, 2005.

Nur, A., and J. R. Booker, Aftershocks Caused by Pore Fluid Flow?, *Science*, *2*, 885–887, 1972.

Ogata, Y., Estimation of the parameters in the modified Omori formula for aftershock frequencies by the maximum likelihood procedure, *J. Phys. Earth*, *31*, 115–124, 1983.

Ogata, Y., Space-time point-process model for earthquake occurrences, *Ann. Inst. Stat. Math.*, *50*(2), 379–402, 1998.

Ogata, Y., and K. Katsura, Immediate and updated forecasting of aftershock hazard, *Geophys. Res. Lett.*, *33*(April), 10–13, doi: 10.1029/2006GL025888, 2006.

Okada, Y., Internal deformation due to shear and tensile faults in a half-space, *Bull. Seism. Soc. Am.*, *82*(2), 1018–1040, 1992.

Okada, Y., K. Kasahara, S. Hori, K. Obara, S. Sekiguchi, H. Fujiwara, and A. Yamamoto, Recent progress of seismic observation networks in Japan–Hi-net, F-net, K-NET and KiK-net–, *Earth, Plan. Space*, *56*, 15–28, doi: 10.1186/BF03353076, 2004.

Ozawa, S., T. Nishimura, H. Suito, T. Kobayashi, M. Tobita, and T. Imakiire, Coseismic and postseismic slip of the 2011 magnitude-9 Tohoku-Oki earthquake, *Nature*, *475*, 373–376, doi: 10.1038/nature10227, 2011.

Ozawa, S., T. Nishimura, H. Munekane, H. Suito, T. Kobayashi, M. Tobita, and T. Imakiire, Preceding, coseismic, and postseismic slips of the 2011 Tohoku earthquake, Japan, *J. Geophys Res.*, *117*, doi: 10.1029/2011JB009120, 2012.

Peng, Z., and P. Zhao, Migration of early aftershocks following the 2004 Parkfield earthquake, *Nature Geoscience*, *2*(12), 877–881, doi: 10.1038/ngeo697, 2009.

Perfettini, H., and J. Avouac, Postseismic relaxation driven by brittle creep: A possible mechanism to reconcile geodetic measurements and the decay rate of aftershocks, application to the Chi-Chi earthquake, Taiwan, *J. Geophys Res.*, *109*, 1–15, doi: 10.1029/2003JB002488, 2004.

Perfettini, H., and J. Avouac, Modeling afterslip and aftershocks following the 1992 Landers earthquake, *J. Geophys Res.*, *112*, 1–19, doi: 10.1029/2006JB004399, 2007.

Perfettini, H., and J. P. Avouac, The Seismic Cycle in the Area of the 2011 Mw9.0 Tohoku-Oki Earthquake, *J. Geophys Res.*, (119), 4469–4515, doi: 10.1002/2013JB010697, 2014.

Pollitz, F. F., R. Bürgmann, and P. Banerjee, Geodetic slip model of the 2011 M9.0 Tohoku earthquake, *Geophys. Res. Lett.*, *38*, 6–11, doi: 10.1029/2011GL048632, 2011.

Pritchard, M. E., and M. Simons, An aseismic slip pulse in northern Chile and along-strike variations in seismogenic behavior, *J. Geophys Res.*, *111*, 1–14, doi: 10.1029/2006JB004258, 2006.

Richards-Dinger, K., R. S. Stein, and S. Toda, Decay of aftershock density with distance does not indicate triggering by dynamic stress, *Nature*, *467*(7315), 583–586, doi: 10.1038/nature09402, 2010.

Rietbrock, A., I. Ryder, G. Hayes, C. Haberland, D. Comte, and S. Roecker, Aftershock seismicity of the 2010 Maule Mw=8.8, Chile, earthquake: Correlation between co-seismic slip models and aftershock distribution?, *Geophys. Res. Lett.*, *39*, 2–6, doi: 10.1029/2012GL051308, 2012.

Ruff, L. J., and B. W. Tichelaar, What controls the seismogenic plate interface in subduction zones?, *Geophys. J. Int.*, 1996.

Ruina, A., Slip Instability and State Variable Friction Laws, *J. Geophys Res.*, *88*, 359–370, 1983.

Ryder, I., A. Rietbrock, K. Kelson, R. Bürgmann, M. Floyd, A. Socquet, C. Vigny, and D. Carrizo, Large extensional aftershocks in the continental forearc triggered by the 2010 Maule earthquake, Chile, *Geophys. J. Int.*, *188*(3), 879–890, doi: 10.1111/j.1365-246X.2011.05321.x, 2012.

Savage, J. C., Calculation of aftershock accumulation from observed postseismic deformation: M6 2004 Parkfield, California, earthquake, *Geophys. Res. Lett.*, *37*(1), 1–4, doi: 10.1029/2010GL042872, 2010.

Savage, J. C., J. L. Svarc, and S.-b. Yu, Postseismic relaxation and aftershocks, *J. Geophys Res.*, *112*, 1–19, doi: 10.1029/2006JB004584, 2007.

Schaff, D. P., G. C. Beroza, and B. E. Shaw, Postseismic response of repeating aftershocks Time-Dependent Recurrence, *Geophys. Res. Lett.*, *25*(24), 4549–4552, 1998.

Segou, M., and T. Parsons, The stress shadow problem in physics-based aftershock forecasting: Does incorporation of secondary stress changes help?, *Geophys. J. Int.*, *41*(11), 3810–3817, doi: 10.1002/2013GL058744, 2014.

Segou, M., T. Parsons, and W. Ellsworth, Comparative evaluation of physics-based and statistical forecasts in Northern California, *J. Geophys Res.*, *118*, 6219–6240, doi: 10.1002/2013JB010313, 2013.

Steacy, S., S. Nalbant, J. Mccloskey, O. Scotti, and D. Baumont, Onto what planes should Coulomb stress perturbations be resolved?, *J. Geophys Res.*, *110*, 1–14, doi: 10.1029/2004JB003356, 2005.

Steacy, S., M. Gerstenberger, C. Williams, D. Rhoades, and A. Christophersen, A new hybrid Coulomb/statistical model for forecasting aftershock rates, *Geophys. J. Int.*, *196*, 918–923, doi: 10.1093/gji/ggt404, 2014.

Stein, R. S., G. C. P. King, and J. Lin, Change in failure stress on the southern San Andreas fault system caused by the 1992 Magnitude = 7.4 Landers earthquake, *Science*, *258*, 1328–1332, 1992.

Stein, R. S., A. A. Barka, and J. H. Dieterich, Progressive failure on the North Anatolian fault since 1939 by earthquake stress triggering, *Geophys. J. Int.*, *128*, 594–604, 1997.

Strader, A., and D. Jackson, Near-prospective test of Coulomb stress triggering, *J. Geophys Res.*, *119*, 3064–3075, doi: 10.1002/2013JB010780, 2014.

Sudhaus, H., and S. Jónsson, Improved source modelling through combined use of InSAR and GPS under consideration of correlated data errors: application to the June 2000 Kleifarvatn earthquake, Iceland, *Geophys. J. Int.*, *176*(2), 389–404, doi: 10.1111/j.1365-246X.2008.03989.x, 2009.

Suito, H., and J. T. Freymueller, A viscoelastic and afterslip postseismic deformation model for the 1964 Alaska earthquake, *J. Geophys Res.*, *114*(B11), doi: 10.1029/2008JB005954, 2009.

Toda, S., and B. Enescu, Rate/state Coulomb stress transfer model for the CSEP Japan seismicity forecast, *Earth, Plan. Space*, (2005), 171–185, doi: 10.5047/eps.2011.01.004, 2011.

Toda, S., and R. Stein, Toggling of seismicity by the 1997 Kagoshima earthquake couplet: A demonstration of time-dependent stress transfer, *J. Geophys Res.*, *108*, 1–12, doi: 10.1029/2003JB002527, 2003.

Toda, S., R. S. Stein, P. A. Reasenberg, J. H. Dieterich, and Y. Akio, Stress transferred by the 1995 Mw=6.9 Kobe, Japan, shock: Effect on aftershocks and future earthquake probabilities, *Journal Geophys. Res.*, *103*, 24,543–24,656, 1998.

Toda, S., J. Lin, and R. S. Stein, Using the 2011 Mw 9.0 off the Pacific coast of Tohoku Earthquake to test the Coulomb stress triggering hypothesis and to calculate faults brought closer to failure, *Earth, Plan. Space*, *63*(7), 725–730, doi: 10.5047/eps.2011.05.010, 2011.

Toda, S., R. S. Stein, G. C. Beroza, and D. Marsan, Aftershocks halted by static stress shadows, *Nature Geoscience*, *5*(6), 410–413, doi: 10.1038/ngeo1465, 2012.

Utsu, T., Aftershocks and earthquake statistics (III): Analyses of the distribution of earthquakes in magnitude, time, and space with special consideration to clustering characteristics of earthquake occurrence (1), *J. Faculty ICEF FINAL REPORT*, *3*, 379–441, 1971.

Utsu, T., and A. Seki, Relation between the area of af- tershock region and the energy of the mainshock, *Zisin (J. Seism. Soc. Japan)*, *2*(7), 233–240, 1955.

Utsu, T., Y. Ogata, and R. Matsu'ura, The Centenary of the Omori Formula for a Decay Law of Aftershock Activity, *J. Phys. Earth*, *43*, 1–33, 1995.

Wang, K., and G. Rogers, Earthquake Preparedness Should Not Fluctuate on a Daily or Weekly Basis, *Seism. Res. Lett.*, *85*(3), 569–571, doi: 10.1785/0220130195, 2014.

Wang, K., Y. Hu, and J. He, Deformation cycles of subduction earthquakes in a viscoelastic Earth, *Nature*, *484*, 327–332, doi: 10.1038/nature11032, 2012a.

Wang, L., S. Hainzl, G. Zöller, and M. Holschneider, Stress- and aftershock-constrained joint inversions for coseismic and postseismic slip applied to the 2004 M6.0 Parkfield earthquake, *J. Geophys Res.*, *117*(B7), 1–18, doi: 10.1029/2011JB009017, 2012b.

Wang, L., J. Liu, J. Zhao, and J. Zhao, Co- and Post- seismic modeling of the 2011 M9 Tohoku-Oki earthquake, and its impact on China mainland, *Earthquake (in Chinese)*, *33*(4), 238–246, 2013.

Wein, A., and J. Becker, Communicating aftershock risk: roles for reassuring the public, *Risk Frontiers*, *13*(3), 2013.

Wells, D. L., and K. J. Coppermith, New Empirical Relationships among Magnitude, Rupture Length, Rupture Width, Rupture Area, and Surface Displacement, *Bull. Seism. Soc. Am.*, *84*(4), 974–1002, 1994.

Werner, M. J., W. Marzocchi, M. Taroni, J.D. Zechar, M. Gerstenberger, M. Liukis, D. A. Rhoades, **C. Cattania**, A. Christophersen, S. Hainzl, A. Helmstetter, A. Jimenez, S. Steacy, T. H. Jordan, Retrospective Evaluation of Earthquake Forecasts during the 2010-12 Canterbury, New Zealand, Earthquake Sequence, *presented at 2014 Fall Meeting, AGU, San Francisco, Califor., 15-19 Dec.*, pp. S23A–4481, 2014.

Woessner, J., S. Jónsson, H. Sudhaus, and C. Baumann, Reliability of Coulomb stress changes inferred from correlated uncertainties of finite-fault source models, *J. Geophys Res.*, *117*, 1–14, doi: 10.1029/2011JB009121, 2012.

Woessner, J., et al., A retrospective comparative forecast test on the 1992 Landers sequence, *J. Geophys Res.*, *116*, 1–22, doi: 10.1029/2010JB007846, 2011.

Yagi, Y., and Y. Fukahata, Introduction of uncertainty of Green's function into waveform inversion for seismic source processes, *Geophys. J. Int.*, *186*, 711–720, doi: 10.1111/j.1365-246X.2011.05043.x, 2011.

Yamanaka, Y., Scaling Relationship between the Number of Aftershocks and the Size of the Main Shock, *J. Phys. Earth*, *38*, 305–324, 1990.

Yang, W., E. Hauksson, and P. M. Shearer, Computing a Large Refined Catalog of Focal Mechanisms for Southern California (1981 - 2010): Temporal Stability of the Style of Faulting, *Bull. Seism. Soc. Am.*, *102*(3), 1179–1194, doi: 10.1785/0120110311, 2012.

Zakharova, O., S. Hainzl, and C. Bach, Seismic moment ratio of aftershocks with respect to main shocks, *J. Geophys Res.*, *118*, 5856–5864, doi: 10.1002/2013JB010191, 2013.

Zechar, J. D., D. Schorlemmer, M. Liukis, J. Yu, F. Euchner, P. J. Maechling, and T. H. Jordan, The Collaboratory for the Study of Earthquake Predictability perspective on computational earthquake science, *Concurrency Computat.: Pract. Exper.*, *22*, 1836–1847, doi: 10.1002/cpe, 2010.

Zhuang, J., M. Werner, S. Hainzl, and D. S. Harte, Theme V - Basic Models/Techniques for Analyzing Seismicity Basic models of seismicity: Temporal models, *Community Online Resource for Statistical Seismicity Analysis*, (Available at http://www.corssa.org), 1–30, 2011.

ACKNOWLEDGEMENTS

This PhD was supported by the REAKT project (strategies and tools for Real-Time EArthquake RisK ReducTion) founded by the European Community via the Seventh Framework Program for Research (FP7), contract 282862. I received additional research training by the Helmholtz graduate research school GeoSim.

Thanks first of all to my supervisor, Sebastian Hainzl, whose positive attitude and support have been very important for me in these years: his office door was always open for discussing work and for advice about navigating the world of scientific research. I felt included and supported in Section 2.1; special thanks to Eleonora Rivalta for her advice and encouragement. I am grateful to Frank Roth for his feedback on several conference presentations and for his support with the computational infrastructure. Finally, thanks to Susanne for being so helpful and patient whenever I struggled with the intricacies of German bureaucracy.

During this PhD I also had the fortune to collaborate with people outside of GFZ. I would like to thank the participants in the CSEP experiment headed by Warner Marzocchi, and in particular Maria Liukis (Masha) for being very helpful during the installation of my models in CSEP. Thanks to Fahad Khalid for his hard work on the code, and for suggestions on how to improve.

I really had a great time in Helmholtzstrasse, and I feel lucky to have met such wonderful colleagues and friends. Thanks to my office mates Christoph and Katrin, who willingly took up the (nearly impossible) task of improving my German; and most of all Olya for being a friend, for our discussions about the most random topics, and for the many and loud laughs. Thanks to my fellow PhD students from section 2.1, and in particular to Michele, Elena and Mehdi; and to the italian crowd for the chats in the kitchen and for sharing times of crisis when the espresso machine was *defekt*. Thanks to Annamaria for our criptic emails ("kf @... ?"), and for sharing the short breaks and lunchtime runs which kept me sane on those long days of "bug-hunting" or the final rush before a conference.

Last but not least, a big thank you goes to my family for their support and their interest in my work, and most of all for helping me to put things in prospective during stressful times.

DECLARATION

I herewith declare that the work in this present thesis is my own work without any help from third parties and without the use of any aids beyond those given. The thesis consists no material previously published by another person.
This work has not been submitted in Germany or abroad to any other examination board in this or similar form.

Potsdam, March 2015

Camilla Cattania